Time Domain Modeling of Photoconductive Antennas

by

Andrea Degasperi

to obtain the degree of Master of Science
at the Delft University of Technology,
to be defended publicly on Wednesday August 28, 2019 at 1:30 PM.

Student number:	4744691	
Project duration:	November 5, 2018 – August 28, 2019	
Thesis committee:	Prof. dr. ir. A. Neto,	TU Delft, supervisor
	Prof. dr. ir. N. Llombart,	TU Delft
	Prof. dr. ir. O. Isabella,	TU Delft

Delft University Of Technology
Department Of Electrical Engineering

The undersigned hereby certify that they have read and recommended to the Faculty of Electrical Engineering, Mathematics and Computer Science for acceptance a thesis entitled "**Time Domain Modeling of Photoconductive Antennas**" by **Andrea Degasperi** in partial fulfillment of the requirements for the degree of **Master of Science**.

Dated: 28/08/2019

Chairman & Supervisor:

prof. dr. Andrea Neto

Committee Members:

prof. dr. Nuria Llombart

prof. dr. Olindo Isabella

Preface

Photoconductive antennas (PCAs) have been extensively utilized for the generation of broadband pulses over very large bandwidths. PCAs rely on a semiconductor (e.g. LT-GaAs) gap pumped by a laser and coupled to a passive structure biased at a certain voltage level. When the laser impinges on the semiconductor gap with an appropriate carrier frequency, enough energy is provided such that free electron-hole pairs are generated from the electrons that move from the valence band to the conduction band. As a result, the resistivity of the material decreases to a few ohms which in turns allows a time-varying current to flow across the gap. In recent year different hybrid equivalent circuits [1], [2], [3] have been developed in order to take into account all these complex phenomena although none of these models account for the frequency dependence of the impedance of the antenna, being formulated in the time domain. This approximation works for non-dispersive antennas such as the bow-tie, but fails in the characterization of more diverse and complex structures. The Norton equivalent circuit's aim proposed in [4] was to fill the aforementioned gap by introducing an analytical model completely in frequency domain, although the difficulty in the characterization of the generator impedance obstructed the way for a wide acceptance in the community. In this thesis a novel approach based on a commercially available electromagnetic simulator [5] to characterize the biasing of the passive structure, the optical laser excitation and the impulse response of the photoconductor is proposed. The accuracy of the model is verified by calculating the average power radiated by a bow-tie and the results are compared to the measurements in [6]. Moreover, a revised version of the Norton equivalent circuit [4] which describes more accurately the effective generator impedance is presented. While the computer-aided model offers great introspection in the characterization of voltages and currents and thus in the maximization of the power radiated, the revised Norton equivalent circuit offers an even better accuracy and reduces significantly the computational time.

This thesis is submitted in partial fulfillment of the requirements for the degree of Master of Science in Electrical Engineering at Delft University of Technology.

Andrea Degasperi
Delft, August 2019

Acknowledgments

This thesis has been carried out entirely at TU Delft in the THz Sensing group.

First of all I want to thank prof. Neto which supported me on a daily basis during this year. Furthermore, I also wanted to express my gratitude to all the people at the THz-Sensing group who during the year dropped instantly their work to help me and in particular: Ralph who helped me a lot with the transmission line model, Arturo who provided a much needed support during the development of the PCA model and prof. Cavallo and prof. Llombart for their invaluable suggestions. Last but not least, I want to dedicate this thesis to my parents who always supported me.

Contents

List of Figures

Chapter 1

Introduction

1.1 Background

Photoconductive antennas (PCAs) have attracted the interest of many researcher since the demonstration of the generation and detection of pulsed broadband THz signals in 1984 by the group lead by David Auston [7, 8]. A number of breakthroughs in photonics in the late 1990s and at the beginning of the 2000s [9, 10] led the way for the development of new applications such as spectroscopy and THz imaging. A complete PCA setup is shown as an example in Figure 1.1.

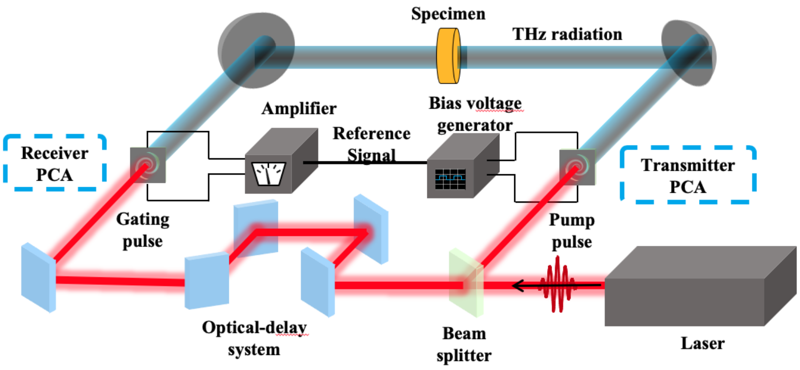

Figure 1.1: Complete PCA setup.

PCAs rely on a semiconductor (e.g. LT-GaAs) gap pumped by a laser and coupled to a passive structure biased at a certain voltage level. When the laser impinges on the semiconductor gap with an appropriate carrier frequency, enough energy is provided such that free electron-hole pairs are generated from the electrons that move from the valence band to the conduction band. As a result, the resistivity of the material decreases to a few ohms which in turns allows a time-varying current to flow across the gap.

In recent year different hybrid equivalent circuits [1, 2, 3] have been developed in order to take into account all these complex phenomena although none of these models account for the frequency dependence of the impedance of the antenna, being formulated in time domain. This approximation works for non-dispersive antennas such as the bow-tie antenna, but fails in the characterization of highly frequency-dependent structures. The Norton equivalent circuit's aim proposed in [4] was to fill the aforementioned gap by introducing an analytical model completely in frequency domain, although the difficulty in the characterization of the generator impedance obstructed the way for a wide acceptance in the community.

A connected array (see [11] and Figure 1.2) of pulsed photoconductive terahertz sources capable to radiate mW level average power has been presented in [6].

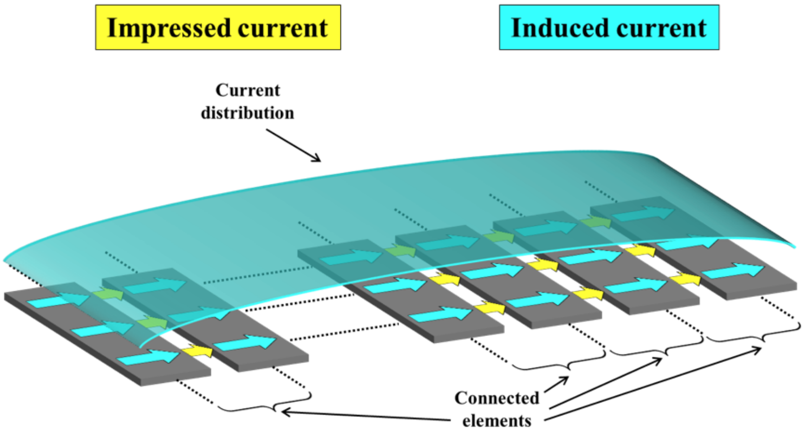

Figure 1.2: Current distribution on a connected array [6].

The measured values of a connected array of dipoles and slots, as shown in Figure 1.3, were compared with the ones predicted by the Norton Equivalent Circuit Model developed in [4].

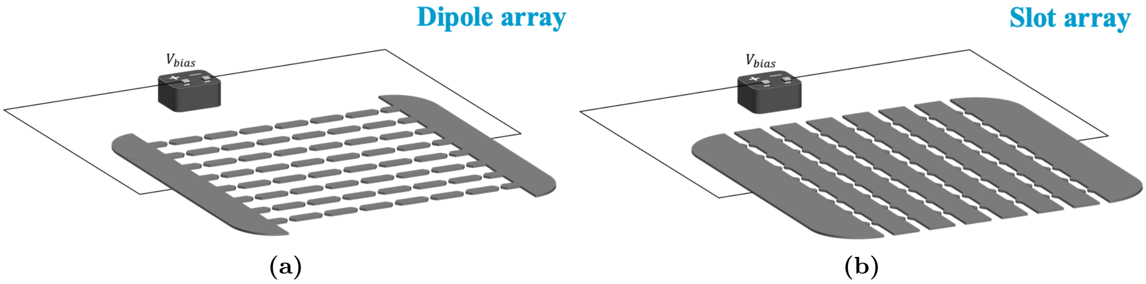

Figure 1.3: Connected array of dipoles and slots [6].

Although the purpose of the Norton Model was specifically to be able to characterize and predict the power radiated by these structures, it was also extensively utilized with single element antennas such as the bow-tie antenna, the H-dipole antenna and the logarithmic spiral antenna [12] (see Figure 1.4).

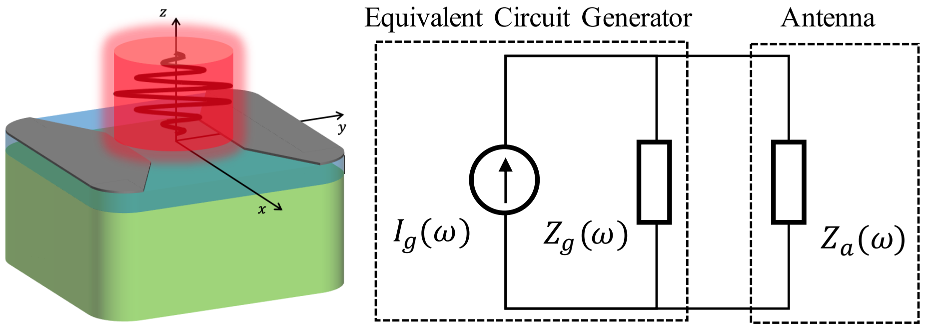

(a) **(b)**

Figure 1.4: Norton Equivalent Circuit Model of the laser excitation on a photoconductive gap with a biased bow-tie antenna [4].

Currently, the Norton Equivalent Circuit model describes well the average power radiated as function of the bias voltage, although presents a high degree of inaccuracy when the laser power is varied. Furthermore, the current unavailability of a single computer aided package that is able to characterize PCAs hinders the development of better designs and the optimization of current ones.

1.2 Solution proposed in this thesis

In this thesis a novel approach based on a commercially available electromagnetic simulator [5] to characterize PCAs which includes the biasing of the passive structure, the optical laser excitation and the impulse response of the photoconductor is proposed. The accuracy of the model is verified by calculating the average power radiated by a bow-tie antenna and the results are compared to the measurements in [6]. Moreover, a revised version of the Norton equivalent circuit [4] which describes more accurately the effective generator impedance is presented. While the computer-aided model offers great introspection in the characterization of voltages and currents and therefore in the transient fields, the revised Norton equivalent circuit offers an even better accuracy when compared with the available measurements of the bow-tie antenna and reduces significantly the computational time.

1.3 Outline of the thesis

This thesis is organized in 4 more chapters. Since this thesis serves as a preparatory work for designing a connected array in which the geometry and the periodicity of the structure account for the pulsed nature of the sources, in chapter 2 and chapter 3 analytical and numerical models are presented in order to describe the fields on various configurations of slots. In particular, in chapter 2 is proposed a transmission-line model of an infinite slot printed on an infinite ground plane between two homogeneous dielectric half-spaces. The model is used to derive the voltage along the slot assuming two active feeds are present. In chapter 3 three different configurations of slots printed on an infinite ground plane between two homogeneous half-spaces are analyzed. The slot has been chosen in this chapter because of the analyticity of the longitudinal Green's function which allows for generally compact notations and much faster computations.
In chapter 4 a novel procedure to analyze pulsed PCAs using an electromagnetic simulator

[5] is described. In particular, a new way to simulate the behavior of PCAs is proposed. Moreover, a revised version of the Norton equivalent circuit [4] which describes more accurately the effective generator impedance is presented.
In chapter 5 the conclusions are presented.

Chapter 2

Transmission-Line Equivalent Circuit of an Infinite Slot

In this section it is proposed the derivation for the voltage using a transmission-line model approach along an infinite slot printed on an infinite ground plane between two homogeneous dielectric half-spaces of permittivity $\varepsilon_{r,1}$ (half-space above) and $\varepsilon_{r,2}$ (half-space below), where it is assumed that $\varepsilon_{r,2} > \varepsilon_{r,1}$. The structure is fed by two electric dipoles at a certain distance $2d_x$ and has a width w which is small in terms of the wavelength. The current distribution is given by two magnetic current with equal amplitudes and opposite signs which are perfectly polarized along x.

2.1 Voltage Derivation

Referring to Figure 2.1, the voltage is derived by applying the superposition principle in three different regions

- Region 1: $d_x \leq d_{x1}$
- Region 2: $d_{x1} < x < d_{x2}$w
- Region 3: $x \geq d_{x2}$

Although the feeds are assumed to be identical, the steps are shown for both ports.

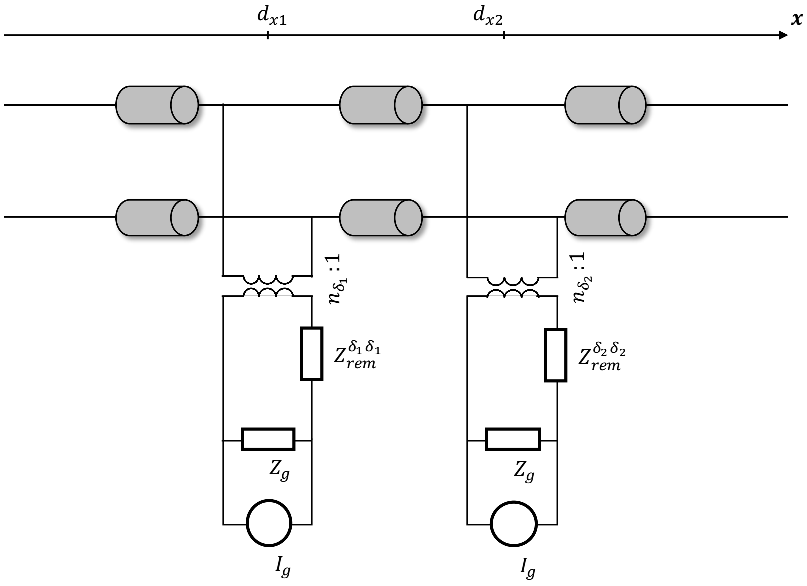

Figure 2.1: Transmission-line equivalent circuit of an infinite slot fed by two feeds positioned at d_{x1} and d_{x2} with a distance of $2d_x$.

2.1.1 Feed 1

Region 1 The general expression for the voltage of the transmission line can be written as

$$V_1(x) = V_1^+ e^{-jk_{xp}x} + V_1^- e^{jk_{xp}x} \tag{2.1}$$

where k_{xp} is the propagation constant associated with the leaky-wave pole. In this case we are considering an infinite line with a regressive voltage wave (i.e., traveling in the negative x direction), therefore the reflection coefficient $\Gamma = 0$ and (2.1) becomes

$$V_1(x) = V_1^- e^{jk_{xp}x} \tag{2.2}$$

where V_1^- is unknown and is derived in the next steps. Figure 2.2 shows the equivalent circuit on the feeding side of the transformer.

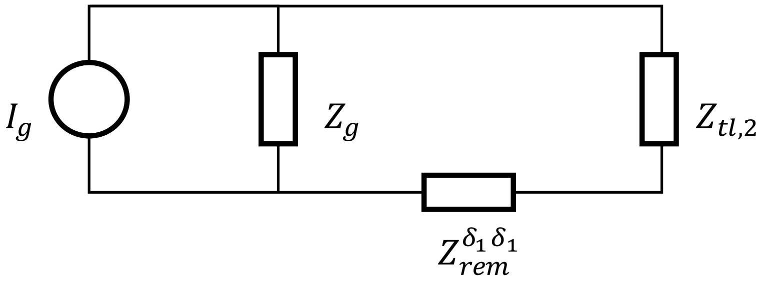

Figure 2.2: Final equivalent circuit showing both the remaining impedance $Z_{rem}^{\delta_1\delta_1}$ and the transmission line equivalent impedance $Z_{tl,2}$, and considering the excitation of feed 1 on the transformer side.

The Norton equivalent frequency-domain circuit, which comprises the current $I_g(\omega)$ and the impedance $Z_g(\omega)$, provides a way to decouple the source from the load, i.e., the antenna under analysis. Without loss of generality, we can therefore assume an arbitrary current $I_g(\omega)$ and an impedance $Z_g(\omega) = Z_{0,s}/2$, where $Z_{0,s}$ is the characteristic impedance of the transmission line computed as the ratio of voltage and current traveling along the slot (see [13] for the derivation)

$$Z_{0,s} = -\frac{2j}{D'(k_{xp})}$$

where $D'(k_{xp})$ is the derivative of the longitudinal Green's function $D(k_{xp})$ (see Appendix A). The *remaining* impedance, $Z_{rem}^{\delta_n\delta_n}$, has an imaginary part related to the reactance of the basis function and a real part related to the radiation of the feed, and can be computed as in [14]

$$Z_{rem}^{\delta_n\delta_n} = Z^{\delta_n\delta_n} - Z_{tl}^{\delta_n\delta_n}$$

where $Z_{tl}^{\delta_n\delta_n}$ is the impedance related to an infinite transmission line with characteristic impedance $Z_{0,s}$ and $Z^{\delta_n\delta_n}$ is the self-impedance of the δ_n feed:

$$Z^{\delta_n\delta_n} = \frac{1}{2\pi}\int_{-\infty}^{\infty} \frac{F_{\delta_n}(k_x)F_{\delta_n}(-k_x)}{D(k_x)}dk_x$$

where $F_{\delta_n}(k_x)$ is the spectral basis function representing the difference between the impressed tangent magnetic fields above and below the slot's ground plane the excites the feed

$$F_\delta(k_x) = \mathcal{F}\left[f_\delta(x)\right] = \operatorname{sinc}\left(\frac{k_x\Delta}{2}\right) \tag{2.3}$$

$$f_\delta(x) = \operatorname{rect}(x) \tag{2.4}$$

where $\mathcal{F}[\cdot]$ is the Fourier-transform (see Appendix B). The end-point impedance of feed 2 can be computed as

$$Z_{end} = \frac{\left[\left(Z_{rem}^{\delta_2\delta_2} + Z_g\right)/n_{\delta_2}^2\right] Z_{0,s}}{\left[\left(Z_{rem}^{\delta_2\delta_2} + Z_g\right)/n_{\delta_2}^2\right] + Z_{0,s}} \tag{2.5}$$

where $n_{\delta_2} = F_\delta(-k_{xp})$ is the transformer's turn ratio. The impedance seen from the first feed, Z_{in}, can be written as

$$Z_{in} = Z_{0,s}\frac{Z_{end} + jZ_{0,s}\tan\left(k_{xp}\left|d_{x1}\right|\right)}{Z_{0,s} + jZ_{end}\tan\left(k_{xp}\left|d_{x1}\right|\right)}$$

or, alternatively, as

$$Z_{in} = Z_{0,s}\frac{e^{-jk_{xp}d_{x1}} + \Gamma_0 e^{jk_{xp}d_{x1}}}{e^{-jk_{xp}d_{x1}} - \Gamma_0 e^{jk_{xp}d_{x1}}}$$

where

$$\Gamma_0 = \frac{Z_{end} - Z_{0,s}}{Z_{end} + Z_{0,s}}$$

The final load of Figure 2.3, Z_{fin}, can be computed as

$$Z_{fin} = Z_{rem}^{\delta_1\delta_1} + Z_{tl,2}$$

where

$$Z_{tl,2} = n_{\delta_1}\left(\frac{Z_{in}Z_{0,s}}{Z_{in} + Z_{0,s}}\right)$$

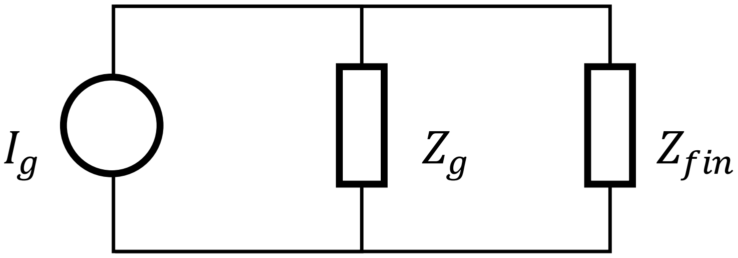

Figure 2.3: Final equivalent circuit showing the final equivalent impedance Z_{fin} and considering the excitation of feed 1 on the transformer side.

The current that enters the impedance Z_{fin} can be calculated as

$$I_{in} = \frac{Y_{fin}}{Y_g + Y_{fin}} I_g$$

And therefore the voltage drop V_{in} on the impedance Z_{fin} becomes

$$V_{in} = I_{in} Z_{tl,2}$$

The voltage on the other side of the transformer, $V(x = d_{x1})$, can be found by simply dividing V_{in} with the transformer turn ratio:

$$V(x = d_{x1}) = \frac{V_{in}}{n_{\delta_1}^2}$$

Therefore (2.2) becomes

$$\frac{V_{in}}{n_{\delta_1}^2} = V_1^- e^{jk_{xp}d_{x1}}$$

and V_1^- can be found as

$$V_1^- = \frac{V_{in}}{n_{\delta_1}^2} e^{-jk_{xp}d_{x1}} \tag{2.6}$$

Finally, the voltage in Region 1 can be written as

$$\begin{aligned} V(x \leq d_{x1}) &= V_1^- e^{jk_{xp}x} \\ &= \frac{V_{in}}{n_{\delta_1}^2} e^{-jk_{xp}d_{x1}} e^{jk_{xp}x} \end{aligned} \tag{2.7}$$

Region 2 The general expression for the voltage of the transmission line can be written as

$$V_2(x) = V_2^+ e^{-jk_{xp}x} + V_2^- e^{jk_{xp}x} \tag{2.8}$$

Imposing the continuity at the interface in $x = d_{x1}$ as

$$V_1(x = d_{x1}) = V_2(x = d_{x1}) \tag{2.9}$$

one obtains

$$V_1^- e^{jk_{xp}d_{x1}} = V_2^+ e^{-jk_{xp}d_{x1}} + V_2^- e^{jk_{xp}d_{x1}}$$

Therefore the forward voltage coefficient is obtained as

$$V_2^+ = \frac{V_1^- e^{jk_{xp}d_{x1}} - V_2^- e^{jk_{xp}d_{x1}}}{e^{-jk_{xp}d_{x1}}} \tag{2.10}$$

where V_1^- is known from (2.6). The impedance (2.5) can be also computed as the ratio of voltage and current in d_{x2}

$$\begin{aligned} Z_{end} &= \frac{V_2(x = d_{x2})}{I_2(x = d_{x2})} \\ &= \frac{V_2^+ e^{-jk_{xp}d_{x2}} + V_2^- e^{jk_{xp}d_{x2}}}{\frac{V_2^+}{Z_{0,s}} e^{-jk_{xp}d_{x2}} - \frac{V_2^-}{Z_{0,s}} e^{jk_{xp}d_{x2}}} \end{aligned}$$

By substituting V_2^+ from (2.10) it is possible to derive V_2^-, alternatively one can write the initial equation as

$$V_2(x) = V_2^+ \left(e^{-jk_{xp}x} + \Gamma_{d_{x2}} e^{jk_{xp}x} \right)$$

where

$$\begin{aligned} \Gamma_{d_{x2}} &= \Gamma_0 e^{-2jk_{xp}d_{x2}} \\ \Gamma_0 &= \frac{Z_{end} - Z_{0,s}}{Z_{end} + Z_{0,s}} \end{aligned}$$

and derive V_2^+ by imposing the boundary conditions at the interface in d_{x1} as in (2.9)

$$\begin{aligned} V_1^- e^{jk_{xp}d_{x1}} &= V_2^+ \left(e^{-jk_{xp}d_{x1}} + \Gamma_{d_{x2}} e^{jk_{xp}d_{x1}} \right) \\ V_2^+ &= \frac{V_1^- e^{jk_{xp}d_{x1}}}{\left(e^{-jk_{xp}d_{x1}} + \Gamma_{d_{x2}} e^{jk_{xp}d_{x1}} \right)} \\ &= \frac{V_{in}/n_{\delta_1}^2}{\left(e^{-jk_{xp}d_{x1}} + \Gamma_{d_{x2}} e^{jk_{xp}d_{x1}} \right)} \end{aligned}$$

Finally, the voltage in Region 2 can be written as

$$\begin{aligned} V_2(d_{x1} < x < d_{x2}) &= V_2^+ \left(e^{-jk_{xp}x} + \Gamma_{d_{x2}} e^{jk_{xp}x} \right) \\ &= \frac{V_{in}/n_{\delta_1}^2}{\left(e^{-jk_{xp}d_{x1}} + \Gamma_{d_{x2}} e^{jk_{xp}d_{x1}} \right)} \left(e^{-jk_{xp}x} + \Gamma_{d_{x2}} e^{jk_{xp}x} \right) \end{aligned} \tag{2.11}$$

Region 3 The general expression for the voltage of the transmission line can be written as

$$V_3(x) = V_3^+ e^{-jk_{xp}x} + V_3^- e^{jk_{xp}x} \tag{2.12}$$

Considering an infinite line with a progressive voltage wave (traveling in the positive x direction), the reflection coefficient is $\Gamma = 0$ and (2.12) becomes

$$V_3(x) = V_3^+ e^{-jk_{xp}x}$$

where V_3^+ is unknown and is derived in the following steps. By imposing the continuity at the interface in $x = d_{x2}$ one obtains

$$\begin{aligned} V_2(x = d_{x2}) &= V_3(x = d_{x2}) \\ V_2^+ \left(e^{-jk_{xp}d_{x2}} + \Gamma_{d_{x2}} e^{jk_{xp}d_{x2}} \right) &= V_3^+ e^{-jk_{xp}d_{x2}} \end{aligned}$$

And therefore V_3^+ is recovered as

$$\begin{aligned} V_3^+ &= \frac{V_2^+\left(e^{-jk_{xp}d_{x2}} + \Gamma_{d_{x2}} e^{jk_{xp}d_{x2}}\right)}{e^{-jk_{xp}d_{x2}}} \\ &= \frac{\frac{V_{in}/n_{\delta_1}^2}{\left(e^{-jk_{xp}d_{x1}} + \Gamma_{d_{x2}} e^{jk_{xp}d_{x1}}\right)}\left(e^{-jk_{xp}d_{x2}} + \Gamma_{d_{x2}} e^{jk_{xp}d_{x2}}\right)}{e^{-jk_{xp}d_{x2}}} \end{aligned}$$

Finally, the voltage in Region 3 can be written as

$$\begin{aligned} V(x \geq d_{x2}) &= V_3^+ e^{-jk_{xp}x} \\ &= \frac{\frac{V_{in}/n_{\delta_1}^2}{\left(e^{-jk_{xp}d_{x1}} + \Gamma_{d_{x2}} e^{jk_{xp}d_{x1}}\right)}\left(e^{-jk_{xp}d_{x2}} + \Gamma_{d_{x2}} e^{jk_{xp}d_{x2}}\right)}{e^{-jk_{xp}d_{x2}}} e^{-jk_{xp}x} \end{aligned} \tag{2.13}$$

2.1.2 Feed 2

Region 3 The general expression for the voltage of the transmission line can be written as

$$V_3(x) = V_3^+ e^{-jk_{xp}x} + V_3^- e^{jk_{xp}x} \tag{2.14}$$

Considering an infinite line with a progressive voltage wave (traveling in the positive x direction), the reflection coefficient is $\Gamma = 0$ and (2.14) becomes

$$V_3(x) = V_3^+ e^{-jk_{xp}x}$$

where V_3^+ is unknown and is derived in the following steps. Computing the voltage at $x = d_{x2}$ as done for Region 1 in subsection 2.1.1, one finds that

$$V(x = d_{x2}) = \frac{V_{in}}{n_{\delta_2}^2}$$

By imposing the continuity at the interface in $x = d_{x2}$ one obtains

$$\begin{aligned} V_3(x = d_{x2}) &= V_3^+ e^{-jk_{xp}d_{x2}} \\ \frac{V_{in}}{n_{\delta_2}^2} &= V_3^+ e^{-jk_{xp}d_{x2}} \end{aligned}$$

Therefore the forward voltage coefficient V_3^+ is obtained as

$$V_3^+ = \frac{V_{in}}{n_{\delta_2}^2} e^{jk_{xp}d_{x2}} \tag{2.15}$$

Finally, the voltage in Region 3 can be written as

$$\begin{aligned} V(x \geq d_{x2}) &= V_3^+ e^{-jk_{xp}x} \\ &= \frac{V_{in}}{n_{\delta_2}^2} e^{jk_{xp}d_{x2}} e^{-jk_{xp}x} \end{aligned} \tag{2.16}$$

Region 2 The general expression for the voltage of the transmission line can be written as

$$V_2(x) = V_2^+ e^{-jk_{xp}x} + V_2^- e^{jk_{xp}x} \tag{2.17}$$

The voltage expression in (2.17) can be written as

$$V_2(x) = V_2^+ \left(e^{-jk_{xp}x} + \Gamma_{d_{x1}} e^{jk_{xp}x} \right)$$

where the reflection coefficient at $x = d_{x1}$, $\Gamma_{d_{x1}}$, differs from the canonical representation since the opposite x direction in considered and therefore

$$\Gamma_{d_{x1}} = \frac{V_2^+}{V_2^-}$$

Imposing the continuity at the interface in $x = d_{x2}$, i.e., $V_3(x = d_{x2}) = V_2(x = d_{x2})$, one obtains

$$V_3^+ e^{-jk_{xp}d_{x2}} = V_2^- \left(e^{jk_{xp}d_{x2}} + \Gamma_{d_{x1}} e^{-jk_{xp}d_{x2}} \right)$$

Therefore V_2^- is obtained as

$$\begin{aligned} V_2^- &= \frac{V_3^+ e^{-jk_{xp}d_{x2}}}{e^{jk_{xp}d_{x2}} + \Gamma_{d_{x1}} e^{-jk_{xp}d_{x2}}} \\ &= \frac{V_{in}/n_{\delta_2}^2}{e^{jk_{xp}d_{x2}} + \Gamma_{d_{x1}} e^{-jk_{xp}d_{x2}}} \end{aligned}$$

where V_3^+ is known from (2.15) and the reflection coefficient at $x = d_{x1}$, $\Gamma_{d_{x1}}$, can be written as

$$\begin{aligned} \Gamma_{d_{x1}} &= \Gamma_0 e^{2jk_{xp}d_{x1}} \\ \Gamma_0 &= \frac{Z_{end} - Z_{0,s}}{Z_{end} + Z_{0,s}} \end{aligned}$$

Finally, the voltage in Region 2 can be written as

$$\begin{aligned} V_2(d_{x1} < x < d_{x2}) &= V_2^- \left(e^{jk_{xp}x} + \Gamma_{d_{x1}} e^{-jk_{xp}x} \right) \\ &= \frac{V_{in}/n_{\delta_2}^2}{e^{jk_{xp}d_{x2}} + \Gamma_{d_{x1}} e^{-jk_{xp}d_{x2}}} \left(e^{jk_{xp}x} + \Gamma_{d_{x1}} e^{-jk_{xp}x} \right) \end{aligned} \tag{2.18}$$

Region 1 The general expression for the voltage of the transmission line can be written as

$$V_1(x) = V_1^+ e^{-jk_{xp}x} + V_1^- e^{jk_{xp}x} \tag{2.19}$$

In this case we are considering an infinite line with a regressive voltage wave (traveling in the negative x direction) with a the reflection coefficient $\Gamma = 0$, therefore (2.19) becomes

$$V_1(x) = V_1^- e^{jk_{xp}x}$$

where V_1^- is unknown and is derived in the following steps. By imposing the continuity at the interface in $x = d_{x1}$ one obtains

$$\begin{aligned} V_2(x = d_{x1}) &= V_1(x = d_{x1}) \\ V_2^- \left(e^{jk_{xp}d_{x1}} + \Gamma_{d_{x1}} e^{-jk_{xp}d_{x1}} \right) &= V_1^- e^{jk_{xp}d_{x1}} \end{aligned}$$

Therefore V_1^- becomes

$$\begin{aligned} V_1^- &= \frac{V_2^-\left(e^{jk_{xp}d_{x1}} + \Gamma_{d_{x1}} e^{-jk_{xp}d_{x1}}\right)}{e^{jk_{xp}d_{x1}}} \\ &= \frac{\frac{V_{in}/n_{\delta_2}^2}{e^{jk_{xp}d_{x2}} + \Gamma_{d_{x1}} e^{-jk_{xp}d_{x2}}}\left(e^{jk_{xp}d_{x1}} + \Gamma_{d_{x1}} e^{-jk_{xp}d_{x1}}\right)}{e^{jk_{xp}d_{x1}}} \end{aligned}$$

Finally, the voltage in Region 1 can be written as

$$\begin{aligned} V(x \geq d_{x1}) &= V_1^- e^{jk_{xp}x} \\ &= \frac{\frac{V_{in}/n_{\delta_2}^2}{e^{jk_{xp}d_{x2}} + \Gamma_{d_{x1}} e^{-jk_{xp}d_{x2}}}\left(e^{jk_{xp}d_{x1}} + \Gamma_{d_{x1}} e^{-jk_{xp}d_{x1}}\right)}{e^{jk_{xp}d_{x1}}} e^{jk_{xp}x} \end{aligned} \tag{2.20}$$

2.2 Results

In order to verify the results obtained with the transmission-line model of the infinite slot between two infinite dielectrics, it is possible to solve a spectral integral for the voltage as

$$v(x,\omega) = \frac{1}{2\pi}\int_{-\infty}^{\infty} \frac{i_1 F_{\delta_1}(k_x) + i_2 F_{\delta_2}(k_x)}{D(k_x)} e^{-jk_x x} dk_x \tag{2.21}$$

where i_n is a unitary current amplitude and $F_{\delta_n}(k_x)$ is the spectral basis function defined in (2.3). The results of the voltage along the slot for the highest and lowest frequencies considered of the spectral integral (2.21) and the voltages obtained in section 2.1 are shown in Figure 2.4.

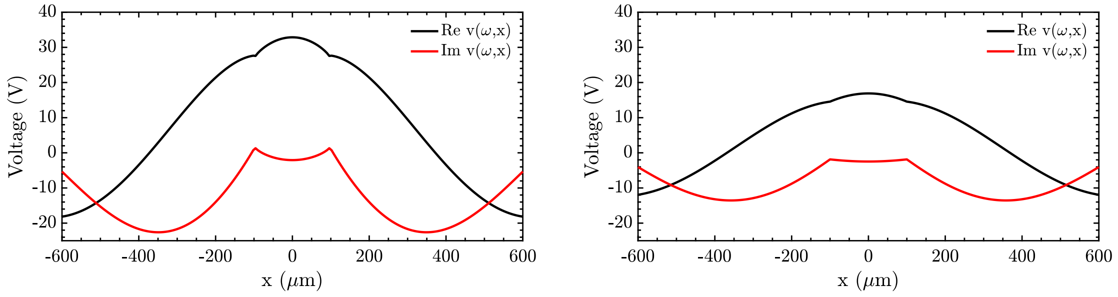

(a) Integral - 100 GHz

(b) Transmission-line - 100 GHz

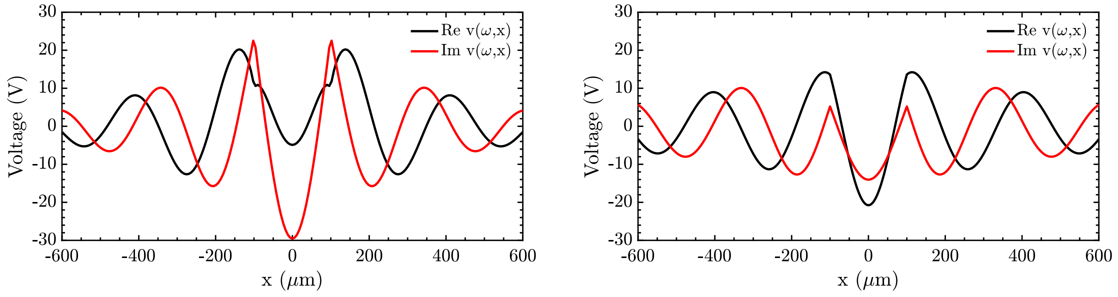

(c) Integral - 400 GHz

(d) Transmission-line - 400 GHz

Figure 2.4: Comparison of the voltage computed along the slot with a transmission-line approach and the full spectral integral. The slot considered has a width $w = 2$ μm and a delta gap $\Delta = 2$ μm and the frequency range is [0.1-0.4] THz. The two feeds considered are positioned in $d_{x1} = -100$ μm and $d_{x2} = 100$ μm.

Although the results are similar, one can notice a certain discrepancy in both the amplitude and the shape of the voltage. In order to explain this behavior Figure 2.5 shows the leaky-wave pole and the branch points of the structure as function of the frequency. The transmission line considers the leaky-wave pole as its propagation constant and therefore a certain (non-negligible) contribution of the space wave (spherical wave radiated from the origin of the structure from the branch points) is lost. Indeed, in different stratifications where the pole is positioned on the real axis (as for example the stratification proposed in [14]), the transmission-line approach yields an accurate result.

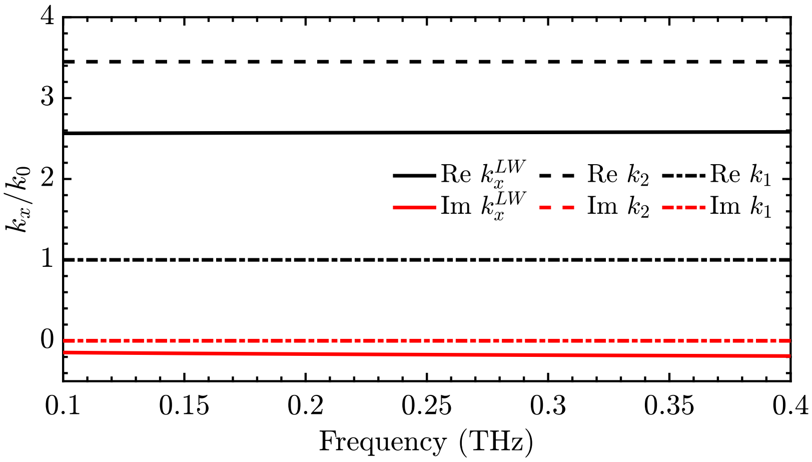

Figure 2.5: Leaky-wave pole k_x^{LW} and branch points k_1 and k_2 normalized to the free space wavenumber k_0.

Chapter 3

Electric field of Various Configurations of Slots

In this chapter three different configurations of slots printed on an infinite ground plane between two homogeneous half-spaces are analyzed. The slot has been chosen in this chapter because of the analyticity of the longitudinal Green's function which allows for generally compact notations and much faster computations. Since this thesis' goal is the introduction of a new computer aided model for Photoconductive Antennas (PCAs), in section 3.1 the time-varying electric field that propagates along an infinite slot and radiated by it is derived, using a simplified current derived in [4] and described in section 4.2. In section 3.2 an infinite array of slots is introduced and the asymptotic electric field is derived. Although this configuration has already been studied previously in [15], in this thesis it has been recognized that the choice of a dielectric with a high enough permittivity in conjunction with an infinite array of slots allows for a leaky-wave antenna with an angle of radiation much higher than it is possible to obtain with a single slot [16], without the need of introducing an air gap between the structure and the dielectric [17]. Finally, for completeness, in section 3.3 it is proposed the extension of section 3.2 for an infinite array of slots with N feeds.

3.1 Infinite Slot Singly Fed

Let us consider a slot printed on an infinite ground plane between two homogeneous half-spaces with permittivity $\varepsilon_{r2} = 11.9$ (silicon) and $\varepsilon_{r1} = 1$ (air), with cross section $w = 2$ μm and delta gap $\Delta = 2$ μm as shown in Figure 3.1.

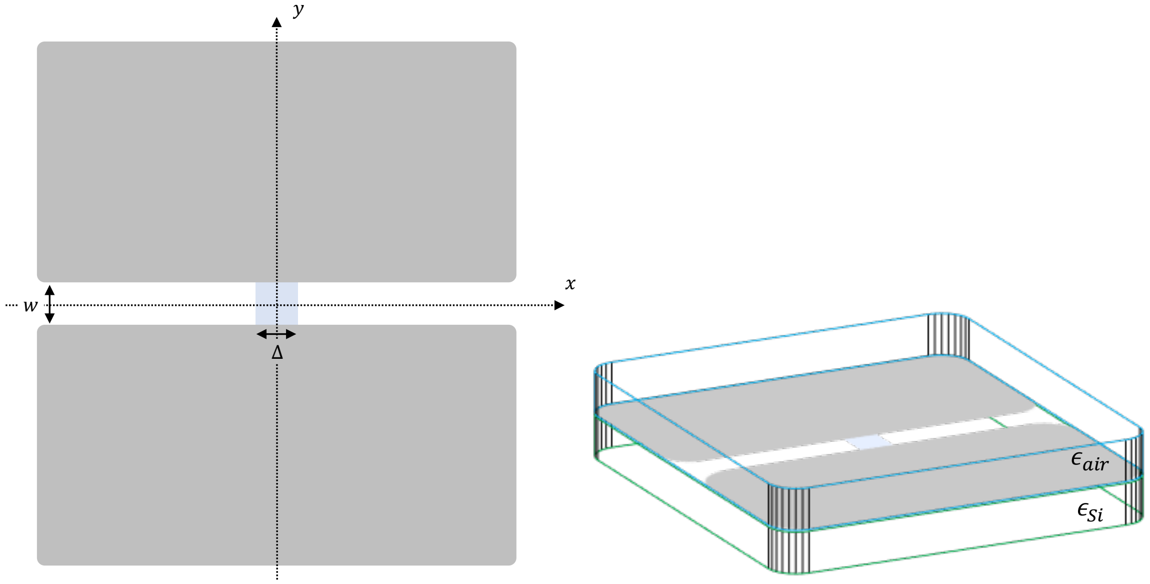

(a) (b)

Figure 3.1: Slot printed on an infinite ground plane between two homogeneous half-spaces with permittivities ε_{r2} and ε_{r1}, where $\varepsilon_{r2} > \varepsilon_{r1}$, with cross section w and delta gap Δ.

3.1.1 Electric field along the slot

The integral equation (as in [18]) which ensures the continuity of the magnetic field on the slot surface is

$$\iint_S g(x-x', -y'; t) m(x', y'; t) dx' dy' = i(t)\,\mathrm{rect}(x) \tag{3.1}$$

where $g(x-x', -y'; t)$ is the time-domain Green's function, $m(x', y'; t)$ is the magnetic current distribution, $i(t)$ is the current exciting the slot and $\mathrm{rect}(x)$ is the rectangular function defined as

$$\mathrm{rect}(x) = \begin{cases} 0, & |t| > 1/2 \\ 1, & |t| \leq 1/2 \end{cases}$$

The spatial distribution of the impulse which excites the feed is therefore a rectangle and the temporal distribution depends from a time-varying current as shown in [4]. The derivation is proposed again herein for completeness.

The examples proposed are pertinent to a photoconductor gap with an area of 2 μm × 2 μm and thickness of 2 μm, an absorption coefficient $\alpha = 10^6$ m^{-1}, a charge carrier lifetime $\tau_r = 0.3$ ps and a free carriers' transient mobility $\mu = 400$ cm^{2}V^{-1}s^{-1}. The laser beam with an average power $\overline{P}_{laser} = 10$ mW and a Gaussian profile with diameter at -3 dB of the gap surface impinges on it. The laser has an half-power pulse-width $\tau_p = 100$ fs, a carrier frequency $f_{\text{laser}} = 375$ THz (central wavelength $\lambda_{\text{laser}} = 800$ nm) and a period of repetition of $T_p = 12.5$ ns (pulse repetition rate $f_p = 80$ MHz).

The time-varying conductance shown as an example in Figure 3.2 can be written as

$$g(t) = \eta(W_x, W_y, W_z, A_{laser}) \frac{A_{laser}}{W_y^2} e\mu h(t) * s(t) \tag{3.2}$$

where $\eta(W_x, W_y, W_z, A_{laser})$ is the laser power absorption efficiency

$$\eta(W_x, W_y, W_z, A_{laser}) = (1-|\Gamma|^2)\frac{1-e^{-\alpha W_z}}{W_z}\frac{1}{A_{laser}}\int_{-W_x/2}^{W_x/2}\int_{-W_y/2}^{W_y/2}\int_{-W_z}^{0}|s(\boldsymbol{\rho}, z=0)|dxdydz \tag{3.3}$$

$h(t)$ is the impulse response of the material with respect to the laser excitation

$$h(t) = \mathcal{F}^{-1}[H(\omega)] = \mathcal{F}^{-1}\left[\frac{1}{hf_g}\frac{\tau_R}{1+j\tau_R\omega}\right] = \frac{1}{hf_g}e^{-\frac{t}{\tau_r}}u(t) \tag{3.4}$$

where $\mathcal{F}^{-1}[\cdot]$ is the anti Fourier-transform (see Appendix B), $u(t)$ is the Heaviside step function and $s(t)$ is the Gaussian modulating signal

$$s(t) = P_0 e^{-4\ln 2\frac{t^2}{\tau_p^2}} \tag{3.5}$$

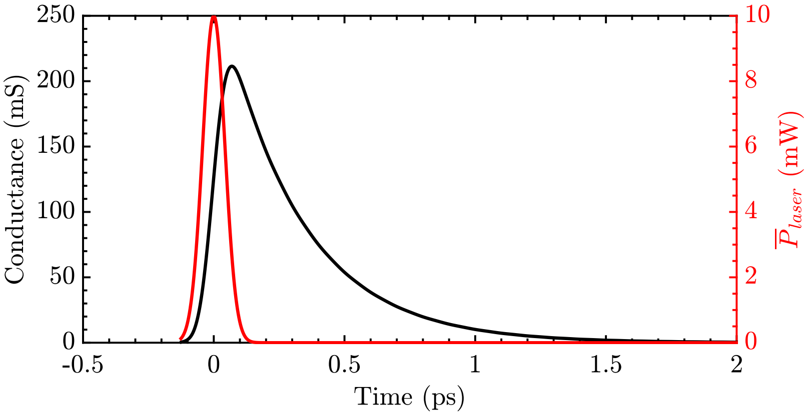

Figure 3.2: Conductance $g(t)$ and laser power envelope $s(t)$.

Through the conductance $g(t)$, one can derive the conductivity $\sigma(t)$ as

$$g(t) = \frac{1}{W_y^2}\int_{-W_x/2}^{W_x/2}\int_{-W_y/2}^{W_y/2}\int_{-W_z}^{0}\sigma(\boldsymbol{r};t)dxdydz \tag{3.6}$$

Thereby obtaining the conductivity as shown in Figure 3.3.

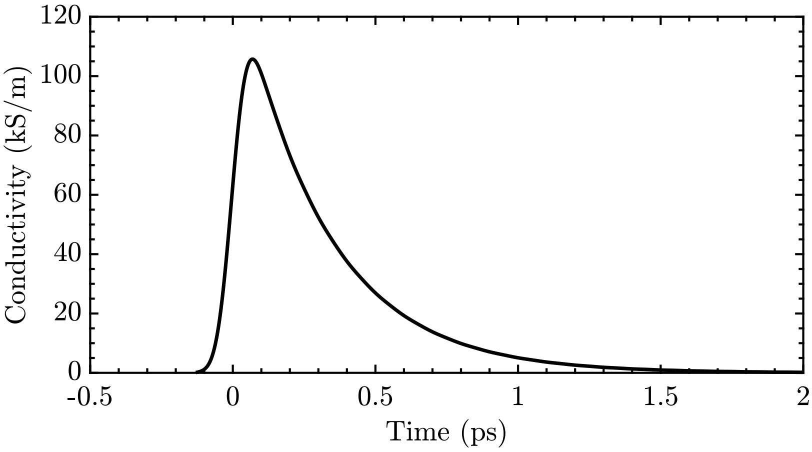

Figure 3.3: Electrical conductivity $\sigma(t)$ of the photoconductor gap.

By applying Ohm's law and assuming a constant electric field $e(\boldsymbol{r};t) = E_{bias}$, the current density $j(\boldsymbol{r};t)$ can be found as

$$j(\boldsymbol{r};t) = \sigma(\boldsymbol{r};t)E_{bias} \tag{3.7}$$

The resulting time-varying current generated on the gap and emitted is shown in Figure 3.4. It is obtained by integrating the current density $j(\boldsymbol{r};t)$ as

$$i(t) = \frac{1}{W_x}\int_{-W_x/2}^{W_x/2}\left(\int_{-W_y/2}^{W_y/2}\int_{-W_z}^{0} j(\boldsymbol{r};t)dydz\right)dx \tag{3.8}$$

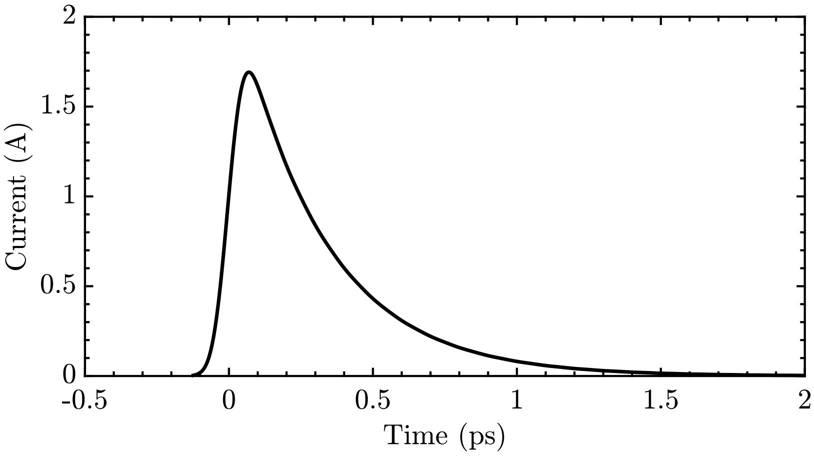

Figure 3.4: Time-varying current generated on the gap that propagates along the passive structure.

The expression for the current in Time Domain (TD) $i(t)$ is then Fourier-transformed in Frequency Domain (FD) as

$$I(\omega) = \int_{-\infty}^{+\infty} i(t)e^{-j\omega t}dt \tag{3.9}$$

The resulting FD current $I(\omega)$ is shown in Figure 3.5.

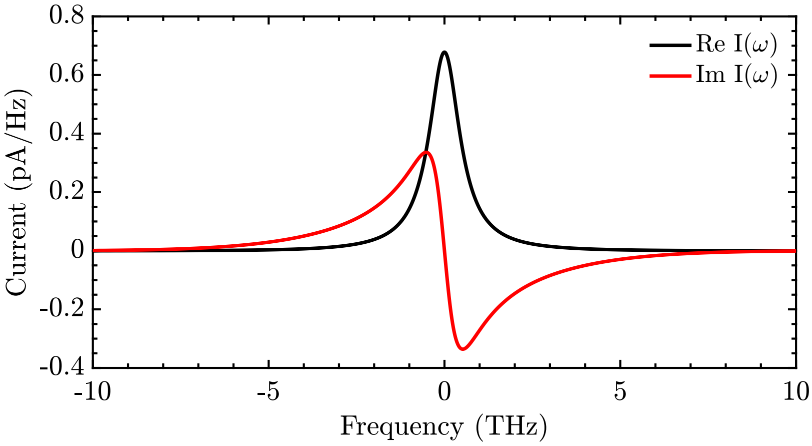

Figure 3.5: Fourier transform of the time-domain current in Figure 3.4.

The normalized magnetic current (i.e., the voltage) is found by spectral synthesis of the

2D-Green's function

$$v(\omega, x) = \frac{1}{2\pi}\int_{-\infty}^{+\infty} \frac{I(\omega)}{D(k_x)} \operatorname{sinc}\left(\frac{k_x \Delta}{2}\right) e^{-jk_x x} dk_x \tag{3.10}$$

where $D(k_x)$ is the longitudinal Green's function as defined in Appendix A. The electric field in FD is then found by dividing the voltage with the width w of the infinite slot and it is shown at the highest and lowest frequency in Figure 3.6.

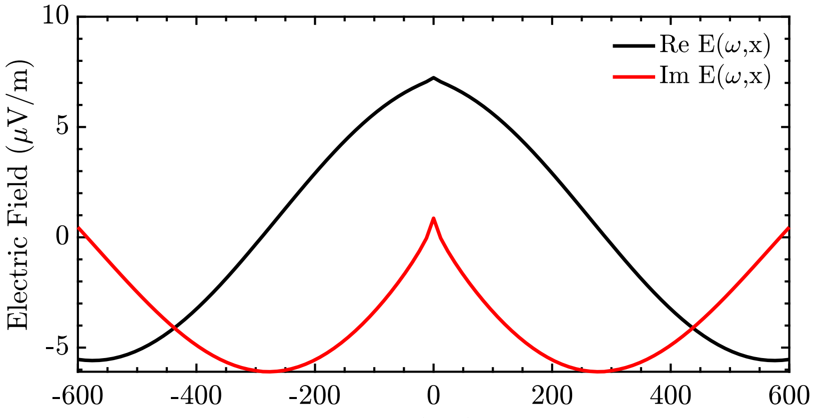

(a) 0.1 THz

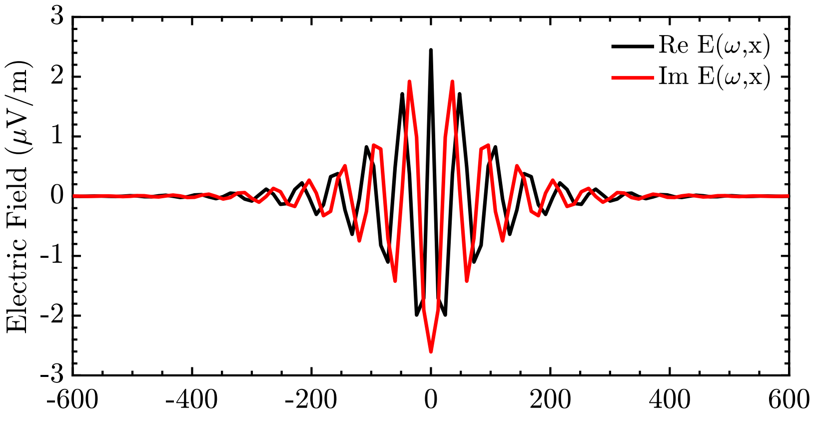

(b) 2 THz

Figure 3.6: Electric field in FD for the highest and lowest frequency considered.

In order to go to the TD from the FD it is possible to apply the canonical inverse-Fourier transform. However, as mentioned in [19], one has to pay attention to the passage from $\omega < 0$ to $\omega > 0$. The complex plane k_x for the spectrum $V(k_x) = 1/D(k_x)$ exhibits branch cuts for $k_z = \pm\sqrt{k_i^2 - k_x^2}$. Considering a time dependence $e^{j\omega t}$, in order to assure that the integrands remain bounded as the limit of $|k_z||z - z'| \to \infty$ it is necessary to impose restrictions on the imaginary part of k_z, therefore we deliberately assume that $\operatorname{Im}\sqrt{k_i^2 - k_x^2} < 0$. In other words, by imposing $\operatorname{Im}\sqrt{k_i^2 - k_x^2} < 0$ one makes sure that for $|k_x| > k$ the non-propagating modes are damped away from the source. One then has to select branch cuts in the complex k_x plane which allow passing from the Top Riemann Sheet (TRS) ($\operatorname{Im} k_z < 0$), to the Bottom Riemann Sheet (BRS) ($\operatorname{Im} k_z > 0$), in such a way that the sign of $\operatorname{Im} k_z$ remains constant. Thus, for a time dependence $e^{j\omega t}$, by choosing the branch cuts as in Figure 3.7, it is verified that $\operatorname{Im} k_z < 0$ on the entire TRS.

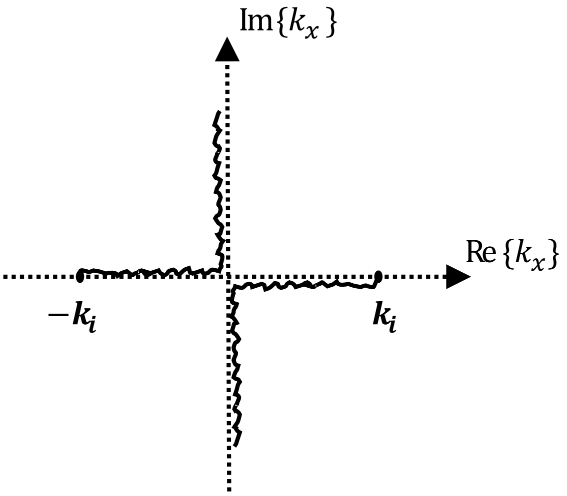

Figure 3.7: Sommerfeld type of branch cuts such that $\operatorname{Im}\sqrt{k_i^2 - k_x^2} < 0$ (i.e., $k_{zi} = -j|k_{zi}|$) on the entire TRS. $\operatorname{Re} k_z > 0$ in the first and third quadrants and $\operatorname{Re} k_z < 0$ in the second and fourth quadrants.

As a consequence, when integrating with positive frequencies the function remains analytic. However, if the sign of ω is changed to a negative one, the assumption regarding the sign of the square root does not hold anymore. It is as if we are assuming a time dependence $e^{-j\omega t}$ and therefore it is required that $\operatorname{Im} k_z > 0$. Therefore the branch cuts change and the integration should be involving unusual choices of the branch cuts with respect to established behaviors. In order to avoid unnecessary complications, it is possible to redefine the relations for a real space-time function $\check{X}(\boldsymbol{r}, t)$

$$X(\boldsymbol{r}, \omega) = \int_{-\infty}^{+\infty} \check{X}(\boldsymbol{r}, t) e^{-j\omega t} dt \tag{3.11}$$

$$\bar{\bar{X}}(\boldsymbol{r}, t) = \frac{1}{\pi} \int_{0}^{+\infty} X(\boldsymbol{r}, \omega) e^{j\omega t} d\omega \tag{3.12}$$

where the $^{=}$ symbol indicates the analytic continuation to complex time. The real field $\check{X}(\boldsymbol{r}, t)$ is obtained by taking

$$\check{X}(\boldsymbol{r}, t) = \operatorname{Re} \bar{\bar{X}}(\boldsymbol{r}, t) \tag{3.13}$$

The voltage in TD $v(t, x)$ can be therefore obtained by applying the upon mentioned properties of the inverse Fourier-transform, accordingly

$$v(t, x) = \operatorname{Re}\left[\frac{1}{\pi} \int_{0}^{+\infty} v(\omega, x) e^{j\omega t} d\omega\right] \tag{3.14}$$

The electric field is obtained by dividing the voltage with the width of the slot as $e(t, x) = v(t, x)/w$. An example of the propagation of the signal is shown in Figure 3.8.

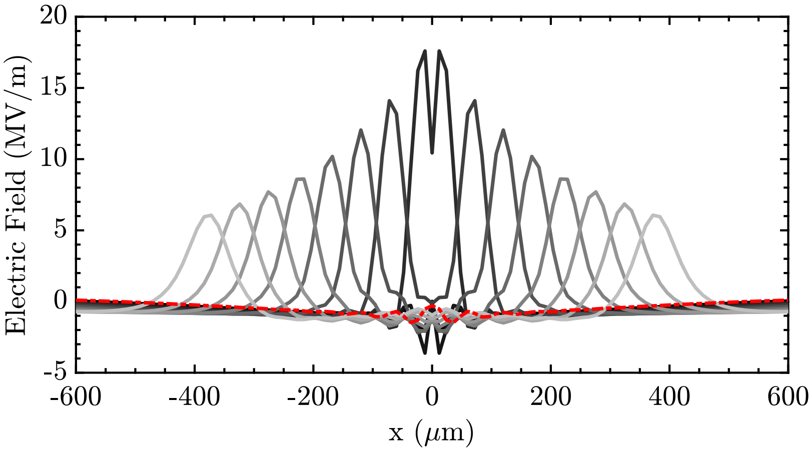

(a) Numerical

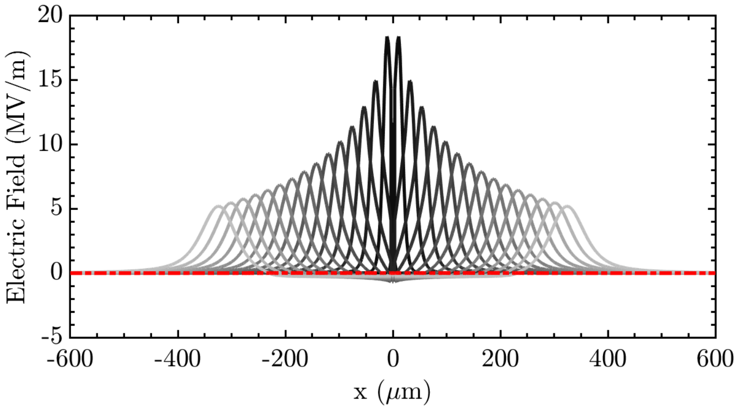

(b) CST

Figure 3.8: Propagation of the electric field in TD computed numerically (Fig. 3.8a) and verified with CST MWS (Fig. 3.8b). The signal at the initial time is represented with a dashed line. The signal propagates (symmetrically) with the speed of light in the denser dielectric (silicon) along the slot (x direction), the various curves represent linearly spaced successive time steps.

3.1.2 Electric field in Fraunhofer region

Considering the same slot that we investigated in subsection 3.1.1, we are now interested in the behavior of the electric field in Fraunhofer region (far field). The distribution along x of the potential is given by the direction of the current, indeed we know that

$$F = \frac{\varepsilon}{4\pi} \iiint\limits_V \mathbf{M} \frac{e^{-jkR}}{R} dv'$$

The electric potential can be written as in [16]

$$\mathbf{F}(\mathbf{r}) = -\frac{1}{4\pi} \int_{-\infty}^{+\infty} \frac{H_0^{(2)}\left(\sqrt{k_2^2 - k_x^2}\rho_t\right)}{jD(k_x)} \operatorname{sinc}\left(\frac{k_x \Delta}{2}\right) I(\omega) e^{-jk_x x} dk_x \hat{\mathbf{x}}$$

The electric field can be computed as

$$\mathbf{E}(\mathbf{r}) = -\frac{1}{\varepsilon} \nabla \times \mathbf{F}(\mathbf{r})$$

In order to avoid doing the curl in spatial domain, we can instead go to the spectral domain

$$\mathbf{E}(\mathbf{r}) = -\frac{1}{\varepsilon} j\mathbf{k} \times \mathbf{F}(\mathbf{r})\hat{\mathbf{x}} = j\frac{F(\mathbf{r})}{\varepsilon}\left(k_y\hat{\mathbf{z}} - k_z\hat{\mathbf{y}}\right)$$

The resulting electric field is

$$\mathbf{E}(\mathbf{r}) = \frac{j}{\varepsilon}\frac{1}{4\pi}\int_{-\infty}^{+\infty} \frac{H_0^{(2)}\left(\sqrt{k_2^2 - k_x^2}\rho_t\right)}{jD(k_x)} \operatorname{sinc}\left(\frac{k_x\Delta}{2}\right) I(\omega)\sqrt{k_2^2 - k_x^2} e^{-jk_x x} dk_x \hat{\mathbf{y}} \tag{3.15}$$

The electric field in TD is recovered via the anti Fourier-transform as explained in subsection 3.1.1:

$$e(t, \mathbf{r}) = \mathrm{Re}\left\{\left[\frac{1}{\pi}\int_0^{+\infty} E(\omega, \mathbf{r}) e^{j\omega t} d\omega\right]\right\}$$

An example of the resulting electric field in TD is shown in Figure 3.9.

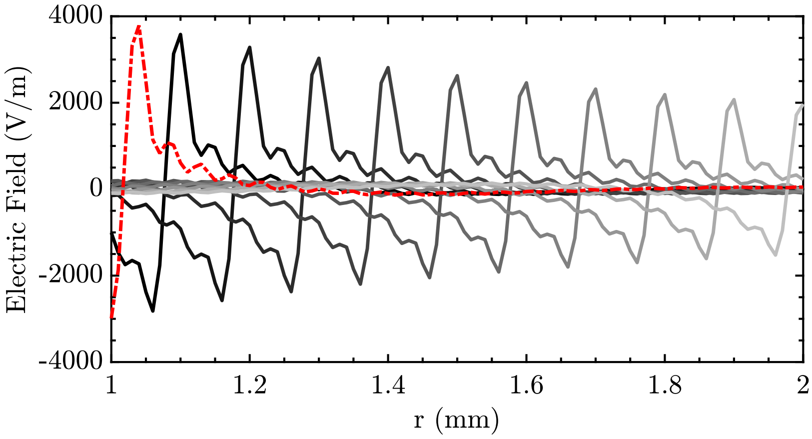

Figure 3.9: Radiation of the electric field in TD at a fixed angle $\theta = 48°$ (w.r.t. a spherical coordinates system where z is orthogonal to the slot plane) away from the slot (r direction). The signal at the initial time considered (≈ 11.5 ps) is represented with a dashed line. The signal propagates with the speed of light in the denser dielectric (silicon), the various curves represent linearly spaced successive time steps.

3.2 Infinite Array of Slots Singly Fed

Let us consider an infinite array of slots printed on an infinite ground plane between two homogeneous half-spaces with permittivity ε_{r2} and ε_{r1}, where $\varepsilon_{r2} > \varepsilon_{r1}$, with cross section w, delta gap Δ and periodicity d_y as shown in Figure 3.10. The slots are excited at their centers with constant amplitude and linear phase.

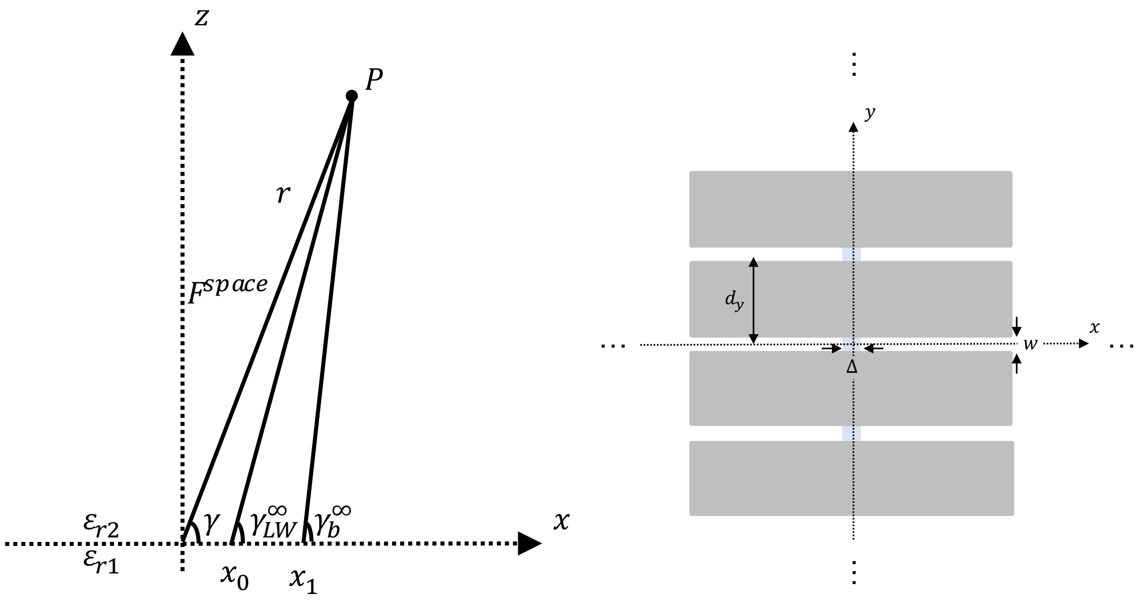

(a) **(b)**

Figure 3.10: Infinite array of slots printed on an infinite ground plane between two homogeneous half-spaces with permittivities ε_{r2} and ε_{r1}, where $\varepsilon_{r2} > \varepsilon_{r1}$, with cross section w, delta gap Δ and periodicity d_y.

3.2.1 Electric Field - Derivation of the Spectral Integral

The electric potential radiated by the central slot of an infinite array of slots can be written as

$$\mathbf{F}(\mathbf{r}) = -\frac{1}{4\pi}\int_{-\infty}^{\infty}\frac{H_0^{(2)}\left(\sqrt{k_2^2-k_x^2}\rho\right)}{jD_\infty(k_x)}\operatorname{sinc}\left(\frac{k_x\Delta}{2}\right)I_0e^{-jk_xx}dk_x\hat{\mathbf{x}}$$

where $\rho = \sqrt{y^2+z^2} = r_0\sin\gamma$, $D_\infty(k_x)$ is the infinite longitudinal Green's function that can be written as

$$D_\infty(k_x) = \frac{1}{d_y}\sum_{m_y=-\infty}^{\infty}\frac{J_0\left(\frac{wk_{ym}}{2}\right)}{k_0\zeta_0}\sum_{i=1}^{2}\frac{k_i^2-k_x^2}{\sqrt{k_i^2-k_x^2-k_{ym}^2}} \tag{3.16}$$

where k_{ym} are the Floquet wavenumbers $k_{ym} = k_{y0} - \frac{2\pi m}{d_y}$ and I_0 is the (assumed) unitary amplitude current exciting the feed. The field radiated by the nth slot can be expressed as

$$\mathbf{F}_{n_y}(\mathbf{r}) = -\frac{1}{4\pi}\int_{-\infty}^{\infty}\frac{H_0^{(2)}\left(\sqrt{k_2^2-k_x^2}\rho\right)}{jD_\infty(k_x)}\operatorname{sinc}\left(\frac{k_x\Delta}{2}\right)I_{n_y}e^{-jk_xx}dk_x\hat{\mathbf{x}}$$

where $\rho_{n_y} = \sqrt{(y-y_{n_y})^2+z^2}$. Here it is assumed that the array is excited by all elements in phase so that $I_{n_y} = I_{n_y=0} = I_0$. Accordingly, the field radiated by a infinite array of slots excited at their center can be expressed as

$$\mathbf{F}(\mathbf{r}) = \sum_{n_y=-N/2}^{N/2}\mathbf{F}_{n_y}(\mathbf{r}) = \sum_{n_y=-N/2}^{N/2}\left[-\frac{1}{4\pi}\int_{-\infty}^{\infty}\frac{H_0^{(2)}\left(\sqrt{k_2^2-k_x^2}\rho\right)}{jD_\infty(k_x)}\operatorname{sinc}\left(\frac{k_x\Delta}{2}\right)I_0e^{-jk_xx}dk_x\right]\hat{\mathbf{x}}$$

In general, the electric field can be computed as

$$\mathbf{E}(\mathbf{r}) = -\frac{1}{\varepsilon}\nabla' \times \mathbf{F}(\mathbf{r})$$

In order to avoid doing the curl in spatial domain, we can go to the spectral domain

$$\mathbf{E}(\mathbf{k}) = -\frac{1}{\varepsilon} j\mathbf{k} \times [F(\mathbf{k})\hat{\mathbf{x}}] \tag{3.17}$$

Recalling that

$$\mathbf{k} = k_x\hat{\mathbf{x}} + k_y\hat{\mathbf{y}} + k_z\hat{\mathbf{z}} \tag{3.18}$$

Substituting (3.18) in (3.17) one obtains

$$\mathbf{E}(\mathbf{k}) = \frac{1}{\varepsilon} jF\,[k_y\hat{\mathbf{z}} - k_z\hat{\mathbf{y}}] \tag{3.19}$$

The resulting electric field is

$$\mathbf{E}(\mathbf{r}) = \frac{j}{\varepsilon}\sum_{n_y=-N/2}^{N/2}\left[-\frac{1}{4\pi}\int_{-\infty}^{\infty}\frac{H_0^{(2)}\left(\sqrt{k_2^2-k_x^2}\rho_{n_y}\right)}{jD_\infty(k_x)}\operatorname{sinc}\left(\frac{k_x\Delta}{2}\right)(k_y\hat{\mathbf{z}} - k_z\hat{\mathbf{y}})\,I_0e^{-jk_xx}dk_x\right]$$

Considering $\phi = 0°$ and $k_y = 0$, the component of the electric field along $\hat{\mathbf{z}}$ is 0, therefore

$$\mathbf{E}(\mathbf{r}) = \frac{jI_0}{\varepsilon 4\pi}\sum_{n_y=-N/2}^{N/2}\left[\int_{-\infty}^{\infty}\frac{H_0^{(2)}\left(\sqrt{k_2^2-k_x^2}\rho_{n_y}\right)}{jD_\infty(k_x)}\operatorname{sinc}\left(\frac{k_x\Delta}{2}\right)\sqrt{k_2^2-k_x^2}e^{-jk_xx}dk_x\right]\hat{\mathbf{y}} \tag{3.20}$$

3.2.2 Electric Field - Asymptotic Ray Approximation

In this section an asymptotic approximation useful for the evaluation of the electric in far field is described. This section is based on [16] and [20].

In subsection 3.2.1 the electric field was derived from the potential in spectral domain. For the purpose of the asymptotic ray approximation, the electric vector potential in spatial form is used instead (in particular its approximation for w small with respect to the wavelength):

$$\mathbf{F}(\mathbf{r}) \approx -\int_{-\infty}^{\infty}\frac{e^{-jk_2R(x-x')}}{4\pi R(x-x')}2v(x')\operatorname{rect}(x')I(x')dx'\hat{\mathbf{x}} \tag{3.21}$$

where $R(x-x') = \sqrt{(x-x')^2+y^2+z^2} = \sqrt{(x-x')^2+\rho_t^2}$. Because the intent of this section is to derive the field in far field, only the space wave contribution is significant to the analysis. In particular, the space wave is a spherical wave with attenuation $(k_2r)^{-1}$, the leaky-wave ray attenuates as $(k_2r)^{-1/2}$ and the later-wave ray attenuates as $(k_1r)^{-2}(k_2r)^{-1/2}$. Hence, the latter has the higher asymptotic order of the three, the leaky-wave has a restricted domain of existence (shadow boundary cone) and the space wave contributes the most along $\gamma_{LW,\infty} = \cos^{-1}\left(\operatorname{Re}k_{x,\infty}^{LW}/k_2\right)$ (due to the phase matching of the space- and leaky-waves at that angle). The space wave is originated in the origin of the reference system (centered on the electric dipole feeding the slot) and is associated with the field radiated by the dipole source itself modulated by the boundary conditions imposed by the slot. Therefore, the integral in (3.21) becomes

$$\mathbf{F}^{\text{space}}(\mathbf{r}) \sim -\int\limits_{\text{Origin}} \frac{e^{-jk_2R(x-x')}}{4\pi R(x-x')} 2v(x')\,\text{rect}(x')I(x')dx'\hat{\mathbf{x}}$$

The phase around the origin (where the space wave is emanated) can be approximated as $k_2R(x-x') \approx k_2r(1-\cos\gamma)$ in order to recover the Fourier-transform of $v(x')$, thus obtaining (note that $k_2\cos\gamma$ is the saddle point in the k_x plane):

$$\mathbf{F}^{\text{space}}(\mathbf{r}) \sim -\frac{2e^{-jk_2r}}{4\pi r}\int\limits_{\text{Origin}} e^{jk_2\cos\gamma x'}v(x')\,\text{rect}(x')I(x')dx'\hat{\mathbf{x}}$$

And finally the potential becomes

$$\mathbf{F}^{\text{space}}(\mathbf{r}) \sim -\frac{1}{D_\infty(k_2\cos\gamma)}\,\text{sinc}\left(\frac{k_2\cos\gamma\Delta}{2}\right) I\left(k_2\cos\gamma\right)\frac{e^{-jk_2r}}{2\pi r}\hat{\mathbf{x}} \tag{3.22}$$

where $D_\infty(k_x)$ is the infinite longitudinal Green's function (see Appendix A) and $I(k_x)$ is spectral current that can be generalized as

$$I(k_x) = I_n e^{jk_x n d_x}$$

The distribution along $\hat{\mathbf{x}}$ of the potential is given by the direction of the current, indeed we know that

$$\mathbf{F} = \frac{\varepsilon}{4\pi}\iiint\limits_V \mathbf{M}\frac{e^{-jkR}}{R}dv'$$

where $\mathbf{M}$ is the magnetic current assumed to be perfectly distributed along the x-axis (considered true for w small in terms of the wavelength). The electric field can be obtained from the potential as in (3.19). It is known that

$$\begin{aligned}\frac{e^{-jk_2r}}{4\pi r} &= -j\frac{1}{8\pi^2}\int_{-\infty}^{\infty}\int_{-\infty}^{\infty}\frac{e^{-jk_xx}e^{-jk_yy}e^{-j\sqrt{k_2^2-k_x^2-k_y^2}z}}{\sqrt{k_2^2-k_x^2-k_y^2}}dk_xdk_y \\ &= -j\frac{1}{8\pi^2}\int_{-\infty}^{\infty}\int_{-\infty}^{\infty}\frac{e^{-jk_xx}e^{-jk_yy}e^{-jk_zz}}{k_z}dk_xdk_y\end{aligned} \tag{3.23}$$

And substituting (3.23) in (3.22), the electric field becomes

$$\mathbf{E}(\mathbf{r}) = \frac{2}{\varepsilon}\left[\frac{j}{8\pi^2}\int_{-\infty}^{\infty}\int_{-\infty}^{\infty}\frac{\text{sinc}\left(\frac{k_x\Delta}{2}\right)I(k_x)}{D_\infty(k_x)}\frac{e^{-jk_xx}e^{-jk_yy}e^{-jk_zz}}{\sqrt{k_2^2-k_x^2-k_y^2}}\left(k_y\hat{\mathbf{z}}-k_z\hat{\mathbf{y}}\right)dk_xdk_y\right] \tag{3.24}$$

Applying the stationary phase method, one obtains

$$\begin{aligned}\mathbf{E}(\mathbf{r}) &= \frac{2}{\varepsilon}\frac{\text{sinc}\left(\frac{k_{xs}\Delta}{2}\right)I(k_{xs})}{D_\infty(k_{xs})}\left[-jk_{ys}\frac{e^{-jk_2r}}{4\pi r}\hat{\mathbf{z}}+jk_{zs}\frac{e^{-jk_2r}}{4\pi r}\hat{\mathbf{y}}\right] \\ &= \frac{j}{\varepsilon}\frac{e^{-jk_2r}}{4\pi r}\frac{\text{sinc}\left(\frac{k_{xs}\Delta}{2}\right)I(k_{xs})}{D_\infty(k_{xs})}\left[-jk_{ys}\hat{\mathbf{z}}+jk_{zs}\hat{\mathbf{y}}\right]\end{aligned} \tag{3.25}$$

where

$$\begin{cases} k_{xs} = k_2 \sin\theta \cos\phi \\ k_{ys} = k_2 \sin\theta \sin\phi \\ k_{zs} = k_2 \cos\theta \end{cases}$$

Considering $\phi = 0°$, (3.25) becomes

$$\mathbf{E}(\mathbf{r}) \sim \frac{jk_2 \cos\theta}{\varepsilon} \frac{e^{-jk_2 r}}{2\pi r} \frac{\operatorname{sinc}\left(\frac{k_{xs}\Delta}{2}\right) I(k_{xs})}{D_\infty(k_{xs})} \hat{\mathbf{y}} \tag{3.26}$$

It is important to notice that this result derived from the electric vector potential in spatial domain form corresponds to the non-uniform asymptotic evaluation of the electric field in spectral domain.

3.2.3 Electric Field - Asymptotic Evaluation

The Steepest Descent Path (SDP) In subsection 3.2.1 the spectral integral of the electric field was found to be

$$\mathbf{E}(\mathbf{r}) = \frac{jI_0}{4\pi\varepsilon_0\varepsilon_r} \sum_{n_y=-N/2}^{N/2} \left[\int_{-\infty}^{\infty} \frac{H_0^{(2)}\left(\sqrt{k_2^2 - k_x^2}\rho_{n_y}\right)}{jD_\infty(k_x)} \operatorname{sinc}\left(\frac{k_x\Delta}{2}\right) \sqrt{k_2^2 - k_x^2} e^{-jk_x x} dk_x \right] \hat{\mathbf{y}} \tag{3.27}$$

The spectral k_x-plane (shown in Figure 3.11), in which (3.27) is defined, exhibits a saddle point at $k_x = k_2 \cos\gamma$ introduced by the Hankel function $e^{-j\sqrt{k_2^2 - k_x^2}\rho_t}$ since the asymptotic expansion for large argument (ρ_t) is

$$H_v^{(2)}(z) \sim \sqrt{\frac{2}{\pi z}} e^{-j\left(z - v\frac{\pi}{2} - \frac{\pi}{4}\right)} \sum_{n=0}^{\infty} \frac{(v, n)}{(-2jz)^n} \tag{3.28}$$

where $v = 0$. Two branch point are associated to the square roots of the integrand at $k_x = \pm k_1, \pm k_2$ with Sommerfeld type of branch cuts such as $\operatorname{Im}\sqrt{k_i^2 - k_x^2} < 0$ (i.e., $k_{zi} = -j|k_{zi}|$) on the entire top Riemann sheet. A leaky-wave pole $k_{x,\infty}^{LW}$ is located on the top Riemann sheet associated with $\sqrt{k_1^2 - k_x^2}$ (i.e., $\operatorname{Im}\sqrt{k_1^2 - k_x^2} < 0$) and on the bottom Riemann sheet associated with $\sqrt{k_2^2 - k_x^2}$ (i.e., $\operatorname{Im}\sqrt{k_2^2 - k_x^2} > 0$) [note that the propagation on the *improper* sheet (for a $e^{j\omega t}$ type of dependence the top sheet is *proper* and the bottom sheet is *improper*, since only the former verifies the radiation condition, i.e., the energy radiated by the source to distant observation points is bounded and out-going) is verified only for the fundamental Floquet mode $m_y = 0$].

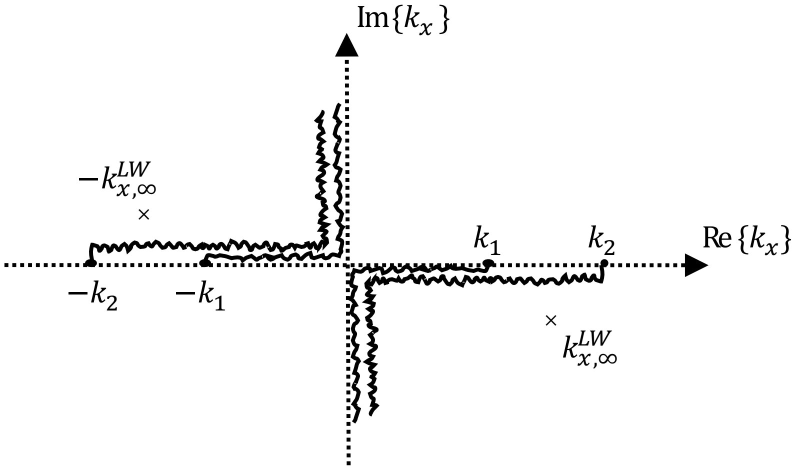

Figure 3.11: L-type branch cuts are associated to the square roots of the infinite longitudinal Green's function. The leaky-wave pole $k^{LW}_{x,\infty}$ is captured on the Bottom Riemann Sheet associated with Im $\sqrt{k_2^2 - k_x^2} > 0$.

In order to facilitate the manipulation of (3.27), it is convenient to introduce a new complex variable α via the transformation

$$k_x = k_2 \cos\alpha \tag{3.29}$$

which identifies α as a complex angle variable and makes $k_{zi} = \sqrt{k_i^2 - k_x^2} = 0$ a regular point in the α plane [the choice of the cosine in (3.29) instead of the sine as in [21] is related to the choice of the angle γ (as in Figure 3.10) which is complementary to the canonical θ]. The transcendental function $\cos\alpha$ is periodic [$\cos(\alpha + 2n\pi) = \cos\alpha \ \forall n$] and therefore a multiplicity of α values correspond to the same value of k_x. This means that the entire k_x plane can be mapped into various adjacent sections of *width* 2π in the α plane. Moreover, the inverse function $\cos^{-1}(k_x/k_2)$ in the k_x plane is multiple valued, implying the existence of branch points in that plane. The branch points occur at those points in the k_x plane for which the mapping derivative $dk_x/d\alpha$ vanishes in the α plane, since $dk_x/d\alpha = -k_2 \sin\alpha$, the branch points are situated at $k_x = \pm k_2$. One can notice that the repetitions with which the k_x-plane is mapped in the α-plane. For example, the Top Riemann sheet of the k_x-plane is mapped into the strip $0 < \operatorname{Re}\alpha < \pi$ and the Bottom Riemann is mapped into the strip $\pi < \operatorname{Re}\alpha < 2\pi$ (thus the Riemann sheets with *width* π appear as adjacent regions in the new mapping). By defining

$$k_{z2} = \sqrt{k_2^2 - k_x^2} = k_2 \sin\alpha \tag{3.30}$$

one is allowed to map $k_{z2}(\alpha = 0, \pi) = 0$ (solving the ambiguity in the k_x-plane) and $k_x(\alpha = 0, \pi) = k_2$. The integral of the electric field in (3.27) can now be mapped in the newly defined α-plane. By employing the asymptotic approximation for large arguments of the Hankel function as in (3.28), changing integration variable as

$$dk_x = -k_2 \sin\alpha d\alpha$$

and substituting (recalling the trigonometric identity $\cos(x - y) = \cos x \cos y + \sin x \sin y$)

$$\begin{cases} x = x_{new} \\ (y - y_{n_y}) = y_{new} \\ z = z_{new} \end{cases}$$

$$\begin{cases} x = r_{n_y} \cos \gamma_{n_y} \\ \rho_{n_y} = \sqrt{(y - y_{n_y})^2 + z^2} = \sqrt{y_{new}^2 + z^2} = r_{n_y} \sin \gamma_{n_y} \end{cases}$$

$$\begin{cases} \sqrt{k_2^2 - k_x^2} = k_2 \sin \alpha \\ k_x = k_2 \cos \alpha \end{cases}$$

The integral in (3.27) becomes

$$\mathbf{E}(\mathbf{r}) = \Omega \sum_{n_y=-N/2}^{N/2} \left[\sqrt{\frac{1}{r_{n_y} \sin \gamma_{n_y}}} \int_C e^{-jk_2 r_{n_y} \cos\left(\alpha - \gamma_{n_y}\right)} f(\alpha) d\alpha \right] \hat{\mathbf{y}} \tag{3.31}$$

where

$$f(\alpha) = \frac{\operatorname{sinc}\left(\frac{k_2 \cos \alpha \Delta}{2}\right) (\sin \alpha)^{3/2}}{D_\infty(k_2 \cos \alpha)}$$
$$\Omega = -\frac{I_0 e^{j\pi/4} (k_2)^{3/2} \sqrt{2}}{4\pi\varepsilon\sqrt{\pi}}$$

The newly defined path C in (3.31) indicates the path $(-j\infty, 0, \pi, \pi + j\infty)$ in the complex α-plane. Note that this is most certainly not the most convenient path of integration, although (3.31) is already in a form suitable to employ the steepest descent method since in far field the large parameter $k_2 r_{n_y}$ dominates over the others. This will be apparent later.

Let's now define the convergence zones. In order to investigate in details the properties of the α-plane, we can separate α in its real and imaginary part:

$$\alpha = \alpha_r + j\alpha_i \tag{3.32}$$

Using Euler's formula and (3.32), we may now write

$$\begin{aligned} \cos(\alpha - \gamma) &= \frac{e^{j(\alpha-\gamma)} + e^{-j(\alpha-\gamma)}}{2} = \frac{e^{j(\alpha_r + j\alpha_i - \gamma)} + e^{-j(\alpha_r + j\alpha_i - \gamma)}}{2} = \frac{e^{j(\alpha_r-\gamma)} e^{-\alpha_i} + e^{-j(\alpha_r-\gamma)} e^{\alpha_i}}{2} \\ &= \frac{\cos(\alpha_r - \gamma) e^{-\alpha_i} + j \sin(\alpha_r - \gamma) e^{-\alpha_i} + \cos(\alpha_r - \gamma) e^{\alpha_i} - j \sin(\alpha_r - \gamma) e^{\alpha_i}}{2} \\ &= \cos(\alpha_r - \gamma) \frac{e^{\alpha_i} + e^{-\alpha_i}}{2} - j \sin(\alpha_r - \gamma) \frac{e^{\alpha_i} - e^{-\alpha_i}}{2} \end{aligned}$$

Substituting in the exponential in (3.31) one obtains

$$e^{-jk_2 r \left[\cos(\alpha_r - \gamma) \frac{e^{\alpha_i} + e^{-\alpha_i}}{2} - j \sin(\alpha_r - \gamma) \frac{e^{\alpha_i} - e^{-\alpha_i}}{2}\right]} = e^{-jk_2 r \cos(\alpha_r - \gamma) \frac{e^{\alpha_i} + e^{-\alpha_i}}{2}} e^{-k_2 r \sin(\alpha_r - \gamma) \frac{e^{\alpha_i} - e^{-\alpha_i}}{2}} \tag{3.33}$$

In order to ensure the convergence of the integral in (3.31), we need to make sure that when α_i (see path C) tends to $\pm\infty$, $e^{-k_2 r \sin(\alpha_r - \gamma) \frac{e^{\alpha_i} - e^{-\alpha_i}}{2}}$ does not vanish, i.e., $\frac{e^{\alpha_i} - e^{-\alpha_i}}{2} > 0$. This defines the zones of convergence of (3.31):

1. $\alpha_i > 0$ implies $\frac{e^{\alpha_i} - e^{-\alpha_i}}{2} > 0$, implies $\sin(\alpha_r - \gamma) > 0 \Rightarrow 0 < \alpha_r - \gamma < \pi$
2. $\alpha_i < 0$ implies $\frac{e^{\alpha_i} - e^{-\alpha_i}}{2} < 0$, implies $\sin(\alpha_r - \gamma) < 0 \Rightarrow -\pi < \alpha_r - \gamma < 0$

Knowing the convergence requirements, we can now define the most convenient numerical path as the one along which the exponential is always decaying and non-oscillating, in particular expressing the exponential as in (3.33), the path that guarantees the upon mentioned properties is the one in which

$$\cos(\alpha_r - \gamma)\frac{e^{\alpha_i} + e^{-\alpha_i}}{2} = 1$$

verified for the saddle point, i.e., the point defined by the vanishing of the first derivative of the argument of the exponential:

$$\frac{d}{d\alpha}\left[-jk_2 r\cos(\alpha - \gamma)\right] = jk_2 r\sin(\alpha - \gamma) = 0 \Rightarrow \alpha = \gamma$$

This deformed path that passes through the saddle point is called Steepest Descent Path (SDP), therefore we can write

$$\mathbf{E}(\mathbf{r}) = \Omega \sum_{n_y=-N/2}^{N/2} \left[\sqrt{\frac{1}{r_{n_y}\sin\gamma_{n_y}}} \int_{\text{SDP}} e^{-jk_2 r_{n_y}\cos\left(\alpha-\gamma_{n_y}\right)} f(\alpha)d\alpha\right] \hat{\mathbf{y}} \tag{3.34}$$

Considering the system of equations valid for the SDP

$$\begin{cases} e^{-jk_2 r_{n_y}\cos\left(\alpha-\gamma_{n_y}\right)} = e^{-jk_2 r_{n_y}\cos\left(\alpha_r-\gamma_{n_y}\right)\frac{e^{\alpha_i}+e^{-\alpha_i}}{2}} e^{-k_2 r_{n_y}\sin\left(\alpha_r-\gamma_{n_y}\right)\frac{e^{\alpha_i}-e^{-\alpha_i}}{2}} \\ \cos\left(\alpha_r - \gamma_{n_y}\right)\frac{e^{\alpha_i}+e^{-\alpha_i}}{2} = 1 \end{cases}$$

We know that

$$e^{-jk_2 r\cos\left(\alpha-\gamma_{n_y}\right)} = e^{-jk_2 r} e^{-k_2 r\sin\left(\alpha_r-\gamma_{n_y}\right)\frac{e^{\alpha_i}-e^{-\alpha_i}}{2}}$$

and that the real part of the argument of the exponential is always decreasing. Let's now introduce an appropriate change of variables which simplifies the evaluation the saddle point in the α-plane (the choice for the transformations is treated in [21]):

$$\cos\left(\alpha - \gamma_{n_y}\right) = 1 - js^2$$

with s defined within the interval $(-\infty, \infty)$ on the real axis. The integral in (3.34) becomes

$$\begin{aligned} \mathbf{E}(\mathbf{r}) &\sim \Omega \sum_{n_y=-N/2}^{N/2} \left[\sqrt{\frac{1}{r_{n_y}\sin\gamma_{n_y}}} \int_{\text{SDP}} e^{-jk_2 r_{n_y}} e^{-k_2 r_{n_y} s^2} f(\alpha)d\alpha\right] \hat{\mathbf{y}} \\ &= \Omega \sum_{n_y=-N/2}^{N/2} \left[\sqrt{\frac{1}{r_{n_y}\sin\gamma_{n_y}}} e^{-jk_2 r_{n_y}} \int_{-\infty}^{\infty} e^{-k_2 r_{n_y} s^2} G(s)ds\right] \hat{\mathbf{y}} \qquad (3.35) \\ &= \Omega \sum_{n_y=-N/2}^{N/2} \left[\sqrt{\frac{1}{r_{n_y}\sin\gamma_{n_y}}} e^{-jk_2 r_{n_y}} \int_{-\infty}^{\infty} e^{\xi(s)\Psi} G(s)ds\right] \hat{\mathbf{y}} \end{aligned}$$

where $\Psi = -k_2 r_{n_y}$, $\xi(s) = s^2$ and $G(s) = f(\alpha)\frac{d\alpha}{ds}$. Note that the newly defined contour passing by $s = 0$ (the saddle point) is the one along which the magnitude of $e^{\xi(s)\Psi}$ decreases more rapidly with $\operatorname{Im}\xi(s)$ constant and $\operatorname{Re}\xi(0) > \operatorname{Re}\xi(s)$, meaning that the contribution to the integral away form the saddle point decreases exponentially and therefore can be neglected, thereby justifying the subsequent evaluation of the slowly varying function $G(s)$ in $s = 0$.

Let's now compute the derivative $d\alpha/ds$

$$-jk_2r\cos(\alpha-\gamma) = -jk_2r - k_2rs^2 \tag{3.36}$$

Recalling the trigonometric identity $\cos(x) = 1 - 2\sin^2(x/2)$, (3.36) becomes

$$\begin{aligned} -jk_2r\left[1-2\sin^2\left(\frac{\alpha-\gamma}{2}\right)\right] &= -jk_2r - k_2rs^2 \\ \rightarrow s^2 &= -j2\sin^2\left(\frac{\alpha-\gamma}{2}\right) \end{aligned}$$

Isolating s:

$$\begin{aligned} s &= \pm\sqrt{2}j\sqrt{j}\sin\left(\frac{\alpha-\gamma}{2}\right) \\ &= \pm\sqrt{2}e^{j3\pi/4}\sin\left(\frac{\alpha-\gamma}{2}\right) \end{aligned}$$

Therefore the derivative $d\alpha/ds$ can be computed as

$$\frac{d\alpha}{ds} = \pm\frac{e^{-j3\pi/4}\sqrt{2}}{\pm\sqrt{1-\sin^2\left(\frac{\alpha-\gamma}{2}\right)}} = \frac{e^{-j3\pi/4}\sqrt{2}}{\sqrt{1-j\frac{s^2}{2}}}$$

Thus, (3.35) becomes

$$\mathbf{E}(\mathbf{r}) \sim \Omega\sum_{n_y=-N/2}^{N/2}\left[\sqrt{\frac{1}{r_{n_y}\sin\gamma_{n_y}}}e^{-jk_2r_{n_y}}\int_{-\infty}^{\infty}e^{-k_2r_{n_y}s^2}G(s)ds\right]\hat{\mathbf{y}} \tag{3.37}$$

where

$$G(s) = f(\alpha)\frac{d\alpha}{ds} = f(\alpha)\left[\frac{e^{-j3\pi/4}\sqrt{2}}{\sqrt{1-j\frac{s^2}{2}}}\right]$$

The new integration interval (and the SDP) is on the real axis of the s-plane and the saddle point is mapped on $s = 0$.

Non-Uniform Asymptotic Evaluation Now we can proceed with the non-uniform asymptotic evaluation, meaning that we aim to expand the slowly varying portion of the integrand in a power series and then we integrate each term. The slowly varying function $f(\alpha)$ can be extracted from the integral and evaluated at the saddle point ($\alpha = \gamma$):

$$\mathbf{E}(\mathbf{r}) \sim \Omega\sum_{n_y=-N/2}^{N/2}\left[\sqrt{\frac{1}{r_{n_y}\sin\gamma_{n_y}}}e^{-jk_2r_{n_y}}f\left(\gamma_{n_y}\right)\int_{-\infty}^{\infty}\frac{e^{-k_2r_{n_y}s^2}}{\sqrt{1-j\frac{s^2}{2}}}ds\right]\hat{\mathbf{y}} \tag{3.38}$$

where

$$f\left(\gamma_{n_y}\right) = \frac{\operatorname{sinc}\left(\frac{k_2 \cos\gamma_{n_y}\Delta}{2}\right)\left(\sin\gamma_{n_y}\right)^{3/2}}{D_\infty(k_2\cos\gamma_{n_y})}$$
$$\Omega = -j\frac{I_0(k_2)^{3/2}}{2\pi\varepsilon\sqrt{\pi}}$$

The denominator of the integrand in (3.38) can be expanded using the Taylor expansion of the canonical form

$$\frac{1}{\sqrt{1+x}} = 1 - \frac{x}{2} + \frac{3x^2}{8} + \dots$$

Therefore one obtains that

$$\frac{1}{\sqrt{1-j\frac{s^2}{2}}} = 1 + \frac{j}{4}s^2 - \frac{3}{32}s^4 + \dots$$

Thus, (3.38) becomes

$$\mathbf{E}(\mathbf{r}) \sim \Omega \sum_{n_y=-N/2}^{N/2}\left[\sqrt{\frac{1}{r_{n_y}\sin\gamma_{n_y}}}e^{-jk_2 r_{ny}} f\left(\gamma_{n_y}\right)\int_{-\infty}^{\infty} e^{-k_2 r_{n_y}s^2}\left(1 + \frac{j}{4}s^2 - \frac{3}{32}s^4 + \dots\right)ds\right]\hat{\mathbf{y}} \tag{3.39}$$

Let's solve the integrals in (3.39) piece-by-piece. The first one is the well-known Gaussian integral (see Appendix B):

$$\int_{-\infty}^{\infty} e^{-k_2 r_{n_y}s^2}ds = \sqrt{\pi}\frac{1}{(k_2 r_{n_y})^{1/2}}$$

The second and the third integrals can be solved in a similar manner:

$$\frac{j}{4}\int_{-\infty}^{\infty} e^{-k_2 r_{n_y}s^2}s^2 ds = \frac{j}{4}\frac{d}{dx}\left[\int_{-\infty}^{\infty} e^{-k_2 r_{n_y}s^2}s^{2-2}ds\right] = \frac{j}{4}\frac{d}{dx}\left[\sqrt{\frac{\pi}{x}}\right] = -\frac{j\sqrt{\pi}}{8}\frac{1}{(k_2 r_{n_y})^{3/2}}$$
$$-\frac{3}{32}\int_{-\infty}^{\infty} e^{-k_2 r_{n_y}s^2}s^4 ds = -\frac{9\sqrt{\pi}}{128}\frac{1}{(k_2 r_{n_y})^{5/2}}$$

Considering only the first term of the Taylor expansion, we finally get:

$$\mathbf{E}(\mathbf{r}) \sim -j\frac{I_0 k_2}{2(\pi)^{3/2}\varepsilon_0\varepsilon_{r2}}\sum_{n_y=-N/2}^{N/2}\left[\sin\gamma_{n_y}\frac{\operatorname{sinc}\left(\frac{k_2\cos\gamma_{n_y}\Delta}{2}\right)}{D_\infty\left(k_2\cos\gamma_{n_y}\right)}\frac{e^{-jk_2 r_{n_y}}}{r_{n_y}}\right]\hat{\mathbf{y}} \tag{3.40}$$

Example In order to show the advantage of employing an infinite array of slots with leaky-wave pole $k_{x,\infty}^{LW}$ over the single slot pole k_x^{LW}, an example is shown.
Let us consider a single infinite slot and an infinite array of slots, both with silicon $\varepsilon_{r2} = 11.9$ and air $\varepsilon_{r1} = 1$ as dielectrics; a width $w = \lambda_d/10$ and delta gap $\lambda_d/10$; the array has a periodicity $d_y = 0.42\lambda_d$ where λ_d is the wavelength in the denser dielectric at the highest frequency. The bandwidth considered varies from 10 to 100 GHz. The leaky-wave poles are shown in Figure 3.12. For an infinite number of slot the leaky-wave poles from each slot coalesce into a single *infinite* pole which can be tracked by simply solving the dispersion

equation $D_\infty(k_x) = 0$ (note that a distinct leaky-wave pole would arise for each slot in a finite array configuration as shown in [15]). The advantage of having an infinite number of slots, as mentioned previously, is a higher angle of radiation. The difference of the resulting pole, $k_{x,\infty}^{LW}$, from the one considering only one slot, k_x^{LW}, is the higher imaginary part especially at low frequencies.

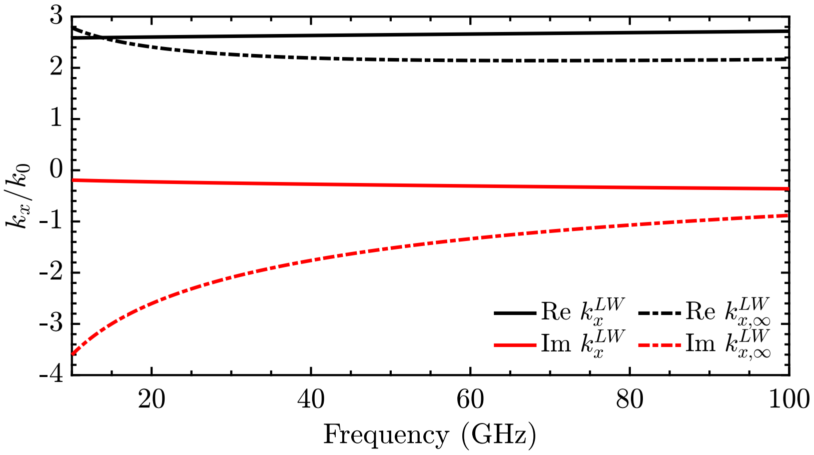

Figure 3.12: Normalized leaky-wave poles $k_{x,\infty}^{LW}$ and k_x^{LW} to the free space wavenumber k_0 related to the infinite array of slots and the single slot, respectively.

The resulting electric field is shown in Figure 3.13. The angle of maximum radiation γ in the example is 72.8°. The results have only a demonstrative purpose in terms of the angle of radiation, in the sense the latter could be increased by, for instance, including a denser dielectric and/or changing the geometric parameters of the slot.

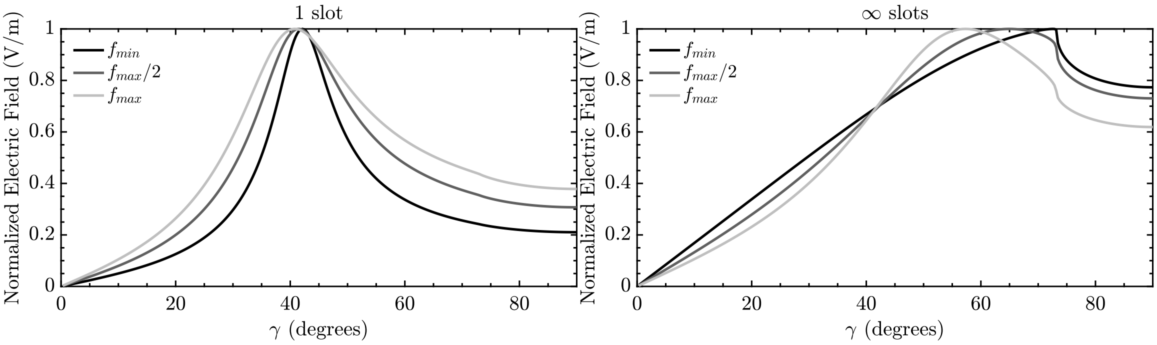

(a) **(b)**

Figure 3.13: Normalized electric field as function of the angle γ. The electric field for an infinite array of slots computed as in (3.40) is compared to the one obtained for a single slot. The former has a maximum of radiation at ≈ 72.5° whereas the latter at ≈ 42.1° at the lower frequency.

The electric field in TD is recovered via the anti Fourier-transform as explained in subsection 3.1.1:

$$e(t, \mathbf{r}) = \mathrm{Re}\left\{ \left[\frac{1}{\pi} \int_0^{+\infty} E(\omega, \mathbf{r}) e^{j\omega t} d\omega \right] \right\}$$

An example of the resulting electric field in TD is shown in Figure 3.14.

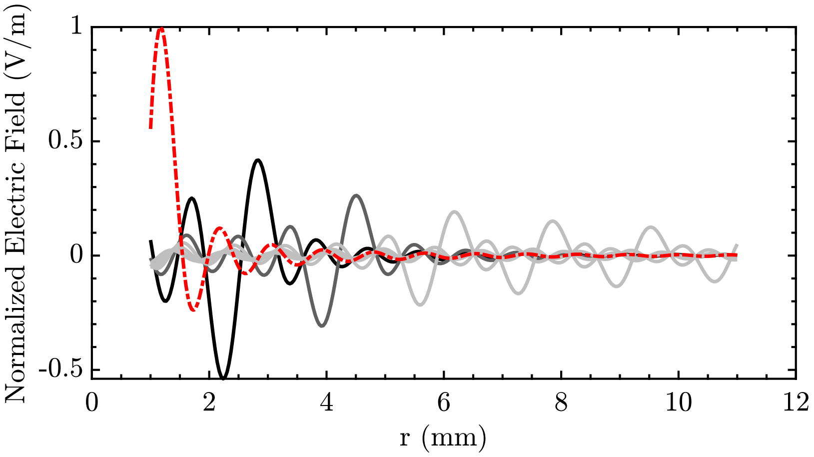

Figure 3.14: Radiation of the normalized electric field in TD at a fixed angle ≈ 72.5° away from the slot (r direction). The signal at the initial time considered (≈ 11.5 ps) is represented with a dashed line. The signal propagates with the speed of light in the denser dielectric (silicon), the various curves represent successive time steps.

3.3 Infinite Array of Slots Fed by N feeds

Let us consider an infinite array of slots fed by N feeds printed on an infinite ground plane between two homogeneous half-spaces with permittivity ε_{r2} and ε_{r1}, where $\varepsilon_{r2} > \varepsilon_{r1}$, with cross section w, delta gap Δ and periodicity $d_x = d_y$ as shown in Figure 3.15.

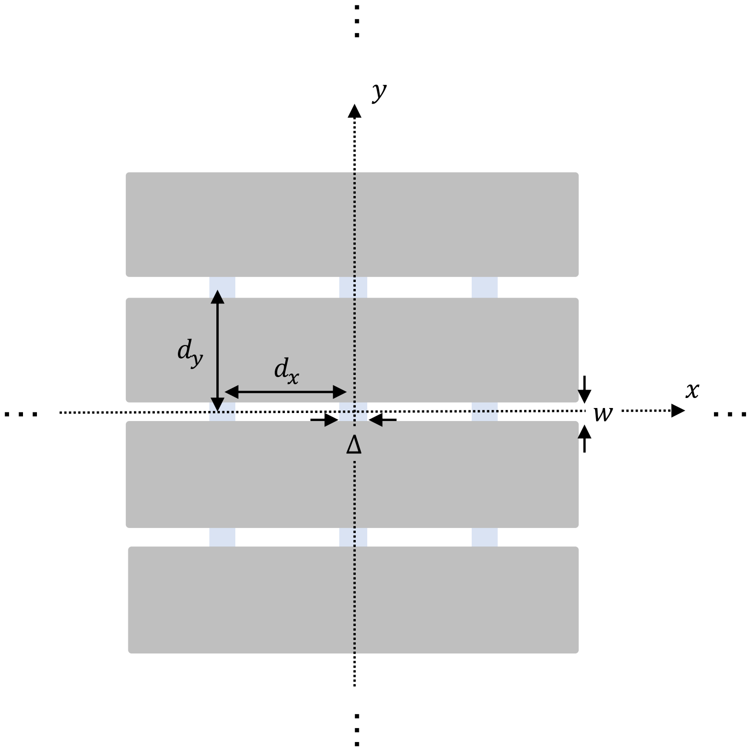

Figure 3.15: Infinite array of slots fed by N feeds printed on an infinite ground plane between two homogeneous half-spaces with permittivities ε_{r2} and ε_{r1}, where $\varepsilon_{r2} > \varepsilon_{r1}$, with cross section w and delta gap Δ.

The procedure employed for the derivation of the electric field of an infinite array of slots fed by N feeds is identical to the one described in section 3.2 and therefore only the result are shown.

The full integral of the electric field considering $\phi = 0°$ and $k_y = 0$ is

$$\mathbf{E}(\mathbf{r}) = \frac{j}{4\pi\varepsilon_0\varepsilon_r}\sum_{n=1}^{N}\left[\int_{-\infty}^{\infty}\frac{H_0^{(2)}\left(\sqrt{k_2^2-k_x^2}\rho_t\right)}{jD_\infty(k_x)}\operatorname{sinc}\left(\frac{k_x\Delta}{2}\right)I_n(k_x)\sqrt{k_2^2-k_x^2}e^{-jk_x x}dk_x\right]\hat{\mathbf{y}} \tag{3.41}$$

where $\rho_t = r\sin\gamma$, $x = r\cos\gamma$ and $I_n(k_x) = I_n e^{jk_x n d_x}$ is the current feeding the N ports. The non-uniform asymptotic evaluation of the integral in (3.41) yields

$$\mathbf{E}(\mathbf{r}) \sim \frac{e^{-jk_2 r}\sqrt{rk_2}k_2\sin\gamma}{2\pi r\varepsilon}\frac{\sum_{n=0}^{N-1}I_n(k_2\cos\gamma)\operatorname{sinc}\left(\frac{k_2\cos\gamma\Delta}{2}\right)}{D_\infty(k_2\cos\gamma)}\left[\frac{1}{(k_2 r)^{1/2}}-\frac{j}{8}\frac{1}{(k_2 r)^{3/2}}-\frac{9}{128}\frac{1}{(k_2 r)^{5/2}}\right]\hat{\mathbf{y}} \tag{3.42}$$

Chapter 4

PCAs Modeling in CST

In this chapter a novel procedure to analyze pulsed photoconductive antennas (PCAs) using an EM simulator [5] is described. In particular, we propose a new way to simulate the behavior of PCAs. The average power radiated of the new model is compared with the measurements obtained in [6]. Moreover, a revised version of the Norton equivalent circuit [4] is presented which improves on the accuracy of the CST model and reduces significantly the computational time.

4.1 Bow-tie Geometry and Measurements

In this thesis the reference antenna considered for the analysis is the bow-tie. Measurements of the average power radiated due to a pulsed PCA source for a bow-tie are available in [6]. Although in [6] the quasi-optical channel efficiency η_{qo} for the bow-tie was relatively low due to a non-directive radiated pattern from the former, the geometrical properties of the bow-tie allow for a low reactive part of the impedance which is shown in Figure 4.1. This is beneficial to the following analysis to avoid losses of efficiency due to mismatching.

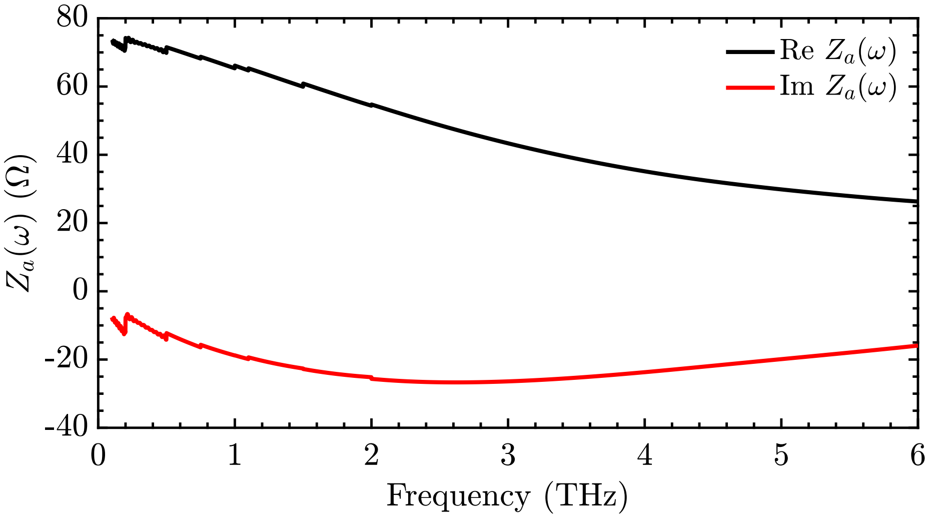

Figure 4.1: Simulated input impedance of the bow-tie antenna.

The dimensions and geometry of the simulated bow-tie refer to the one reported in [12] and are shown in Figure 4.2.

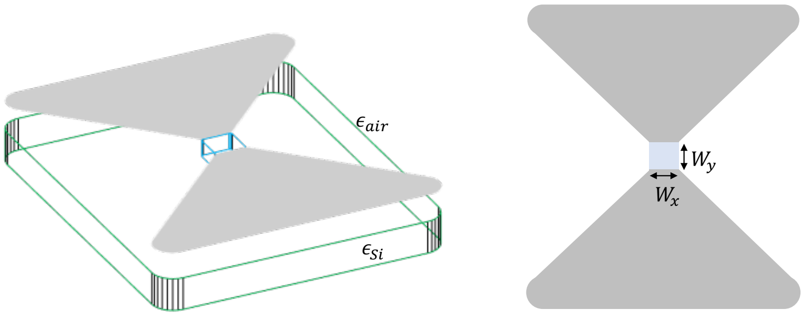

Figure 4.2: Bow-tie geometrical features. The antenna under investigation is printed on a ground plane between two homogeneous dielectric half-spaces of permittivity $\varepsilon_{r,air}$ (half-space above) and $\varepsilon_{r,silicon}$ (half-space below), which represents the silicon lens. The gap is modeled with a thin slab of photoconductive material made of low-temperature-grown gallium arsenide (LT-GaAs) with height $W_z = 2\ \mu$m and transversal dimensions $W_x = W_y = 10\ \mu$m. The length of the measured bow-tie is $L = 2$ mm and the tapering of 90°.

4.2 Norton Equivalent Circuit Model

This section introduces the model proposed in [4] and highlights its limits in order to delineate more clearly the improvements of the new CST model proposed in this thesis (section 4.3). Moreover, it serves as a comparison for the revised version of the Norton equivalent model in section 4.4.

The antenna is assumed to be biased by a DC voltage source, and the semiconductor gap is excited by a laser pulse whose properties are summarized in Table 4.1. The two sources, DC bias and laser pulse, are assumed to be represented by an equivalent circuit that provides an adequate linearized description for the time varying response of the circuit.

4.2.1 Norton - Model Description

The Norton Equivalent Circuit Model simplifies the analysis of the antenna coupling with the photoconductor gap by describing a complex circuit in which the former is decoupled from the latter. The circuit is shown in Figure 4.3.

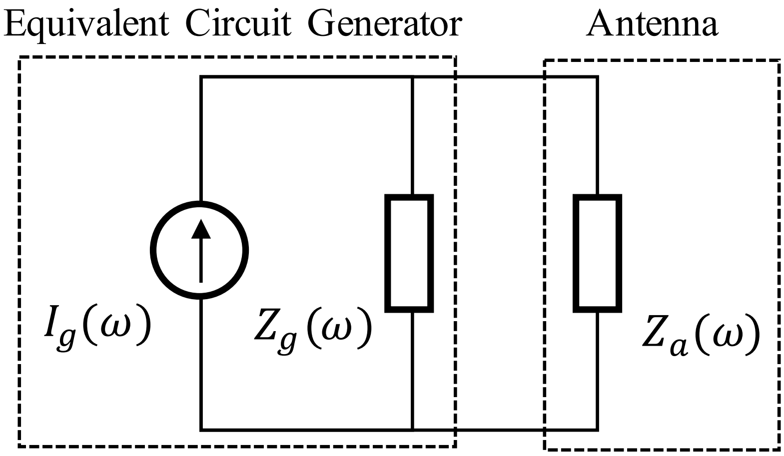

Figure 4.3: Norton equivalent circuit. The current generator $I_g(\omega)$ and the generator impedance $Z_g(\omega)$ are evaluated when the antenna impedance $Z_a(\omega)$ is short-circuited.

In order to compute the short-circuit current flowing across the gap it is assumed that the electric field is approximately constant with respect to time during the laser excitation, therefore

$$i_g(t) \approx g(t)V_{bias} \tag{4.1}$$

It must be noted that this approximation is very accurate if one considers the antenna being short-circuited, this will be apparent in section 4.4. In (4.1) V_{bias} is the bias level of the battery and $g(t)$ is the conductance, computed as:

$$g(t) = \eta\left(W_x, W_y, W_z, A_{laser}\right)\frac{A_{laser}}{W_y^2} e\,\mu\,h(t) * \widetilde{s}(t) \tag{4.2}$$

where η is the laser absorption efficiency computed as

$$\eta\left(W_x, W_y, W_z, A_{laser}\right) = \left(1-|\Gamma|^2\right)\frac{1-e^{-\alpha W_z}}{W_z}\frac{1}{A_{laser}}\int_{-W_y/2}^{W_y/2}\int_{-W_x/2}^{W_x/2}\int_{-W_z}^{0}\left|\widetilde{\mathbf{s}}_n\left(\boldsymbol{\rho}; z=0\right)\right| dz\,dx\,dy \tag{4.3}$$

where $\widetilde{\mathbf{s}}_n\left(\boldsymbol{\rho}; z=0\right)$ is the normalized spatial distribution of the Poynting vector, Γ is the optical Fresnel reflection coefficient at the air-semiconductor interface, α is the laser absorption coefficient at the semiconductor material, A_{laser} is the area of the laser beam on the semiconductor with unitary amplitude defined as

$$A_{laser}(z) = \int_{-\infty}^{\infty}\int_{-\infty}^{\infty}\widetilde{\mathbf{s}}_n\left(\boldsymbol{\rho}, z\right)\cdot\widehat{\mathbf{z}}\,dx\,dy \tag{4.4}$$

e is the elementary charge, μ is the free carriers' transient mobility, $h(t)$ is the impulsive response of the semiconductor expressed as

$$h(t) = \frac{1}{hf_g}e^{-\frac{t}{\tau_r}}u(t) \tag{4.5}$$

where $h = 6.626070040 \cdot 10^{-34}$ (Js) is the Planck's constant, f_g is the frequency associated to the energy band-gap $E_g = hf_g$ of the semiconductor material, τ_r is the charge carrier lifetime and $u(t)$ is the Heaviside step function defined as

$$u(t) = \begin{cases} 0, & t < 0 \\ 1, & t \geq 0 \end{cases}$$

$\widetilde{s}(t)$ is the laser power envelope which is assumed to have a Gaussian shape that can be written as

$$\widetilde{s}(t) = P_0 e^{-4\ln 2\frac{t^2}{\tau_p^2}} \tag{4.6}$$

where P_0 is the peak power of the pulse which is related to the area of the spatial distribution of the laser beam and the peak amplitude of the pulse envelope as $P_0 = A_{laser}(z)S_0(z)$ and τ_p is the half-power pulse-width. The spectrum of the current-generator $I_g(\omega)$ is obtained by Fourier-transforming (see Appendix B) the time-varying current $i_g(t)$ as

$$I_g(\omega) = \mathcal{F}\left[i_g(t)\right]$$

The generator impedance $Z_g(\omega)$ is the ratio of the voltage and current spectra. However, since the evaluation of these two quantities is not trivial, the generator impedance is computed with a zero*th* order approximation:

$$Z_g(\omega) \approx \frac{1}{g_0} = r_0 \tag{4.7}$$

where g_0 is the average of the conductance in an arbitrary time interval τ_σ, defined where $g(t)$ is above 1/100 of its peak:

$$g_0 = \eta\,(W_x, W_y, W_z, A_{laser})\,\frac{A_{laser}}{W_y^2} e\,\mu\,\frac{1}{\tau_\sigma} H(\omega = 0)\widetilde{S}(\omega = 0) \tag{4.8}$$

An example of the impedance of the generator is shown in Figure 4.4. The impedance of the antenna $Z_a(\omega)$ can be computed with an electromagnetic simulator or analytically, depending on the structure considered.

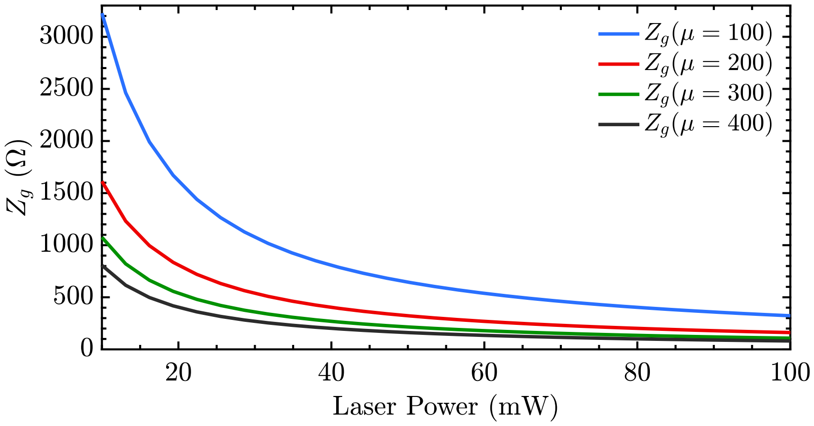

Figure 4.4: Norton Generator impedance in function of the laser power. The mobility is measured in $\mathrm{cm^2V^{-1}s^{-1}}$.

The generalized Parseval's theorem states that

$$E = \int_{-\infty}^{\infty} v_a(t)i_a(t)dt = \frac{1}{2\pi}\int_{-\infty}^{\infty} V_a(\omega)I_a^*(\omega)d\omega \tag{4.9}$$

where $V_a(\omega) = \mathcal{F}[v_a(t)]$ and $I_a(\omega) = \mathcal{F}[i_a(t)]$ are the spectra of the voltage and current; $v_a(t)$ and $i_a(t)$ are the time-varying voltage and current, respectively, observed on the photoconductor gap. The gap current $i_g(t)$ for a short-circuited antenna computed as in (4.1) is shown as an example in Figure 4.5 for different laser powers, a bias voltage $V_{bias} = 40$ V and a mobility $\mu = 100\ \mathrm{cm^2V^{-1}s^{-1}}$. Since the voltage is assumed to be always constant and the conductance varies linearly for different laser powers, according to (4.1) also the current presents the same behavior.

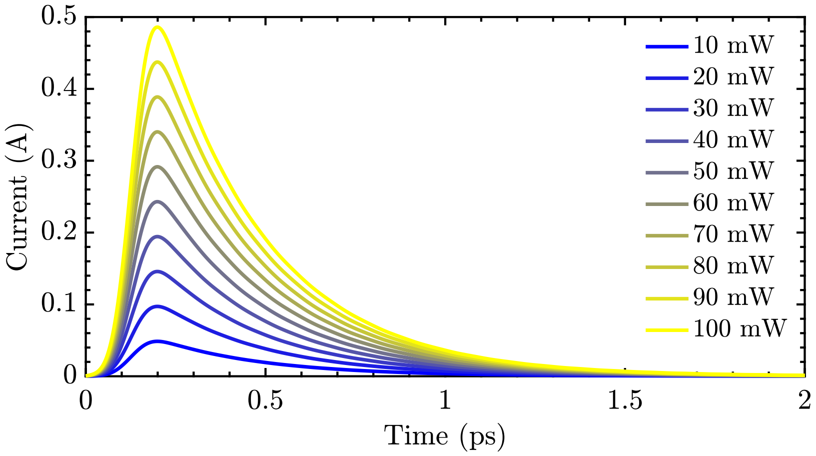

Figure 4.5: Current on the photoconductor gap as function of time for various laser powers. The antenna is biased at $V_{bias} = 40$ V and the semiconductor has a mobility $\mu = 100\ \mathrm{cm^2V^{-1}s^{-1}}$.

The current and voltage in frequency domain on the antenna are calculated as

$$I_a(\omega) = I_g(\omega)\frac{Z_g(\omega)}{Z_g(\omega) + Z_a(\omega)} \tag{4.10}$$

$$V_a(\omega) = I_a(\omega)Z_a(\omega) \tag{4.11}$$

The energy spectral density $E_s(\omega)$ associated with the antenna radiation is a real quantity for the Hermitian symmetry of the spectra and can be written as

$$E_s(\omega) = V_a(\omega)I_a^*(\omega) = Z_a(\omega)\left|\frac{Z_g}{Z_g + Z_a(\omega)}\right|^2 |I_g(\omega)|^2 \tag{4.12}$$

One can compute the average power radiated by the antenna as

$$\overline{P}_{rad} = \frac{1}{T_p}\frac{1}{2\pi}\int_{-\infty}^{\infty} E_s(\omega)\,\eta_{op}(\omega)\,d\omega \tag{4.13}$$

where η_{op} is the quasi-optical system efficiency that includes the radiation efficiency of the lens, the reflector system efficiency and the detector efficiency, and T_p is period of repetition of the laser excitation.

4.2.2 Norton - Model Results

The average power radiated estimated with the Norton Equivalent Circuit Model as function of the bias voltage with a free carriers' transient mobility of $\mu = 220\ \mathrm{cm^2V^{-1}s^{-1}}$ and for an average laser power of $\overline{P}_{laser} = 30$ mW is shown in Figure 4.7. Table 4.1 summarizes the parameters used in the model.

Table 4.1: Norton Equivalent circuit parameters of laser and semiconductor material. The parameters refer to the setup described in [6]. In particular, τ_p is the half-power pulsewidth, f_{laser} is the frequency associated with the energy band-gap, f_p is pulse repetition rate of the laser, D_{laser} is the focused laser beam diameter and η_{so} is the spillover efficiency (the laser beam profile is Gaussian); $W_{x,y}$ and W_z are the transversal and longitudinal dimensions of the photoconductor gap, respectively, α is the laser absorption coefficient at the semiconductor material, τ_r is the charge carrier lifetime, μ is the free carriers' transient mobility and Γ is the optical Fresnel reflection coefficient at the air-semiconductor interface.

Laser	**Semiconductor**
$\tau_p = 0.1$ ps	$W_x = W_y = 10\ \mu$m
$f_{laser} = 375$ THz	$W_z = 2\ \mu$m
$f_p = 80$ MHz	$\alpha = 10^6\ \mathrm{m}^{-1}$
$D_{laser} = 14.5\ \mu$m	$\tau_r = 0.3$ ps
$\eta_{so} = 0.34$	$\mu = 220\ \mathrm{cm^2V^{-1}s^{-1}}$
	$\Gamma = \sqrt{0.3}$

The model shows good agreements with the results, although, as depicted in Figure 4.8, for different laser power levels at a fixed voltage $V_{bias} = 40$ V it is not accurate. In particular, it is apparent that the choice of the generator impedance Z_g is such that it dominates over the antenna impedance $Z_a(\omega)$ and therefore the prediction of the model does not account for saturation at higher laser power levels. This behavior becomes apparent when analyzing the voltages and currents on the antenna load. In order to recover the time-varying current $i_a(t)$ and voltage $v_a(t)$ the inverse Fourier-transform (see Appendix B for the definition used) is applied on (4.10) and (4.11), respectively. It is possible to observe that the voltages and currents exhibit almost no saturation when the laser power level is increased.

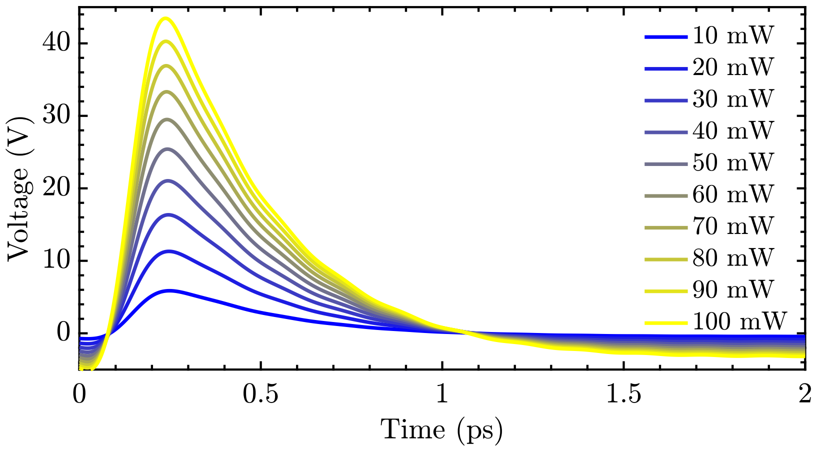

(a) Voltages on the gap

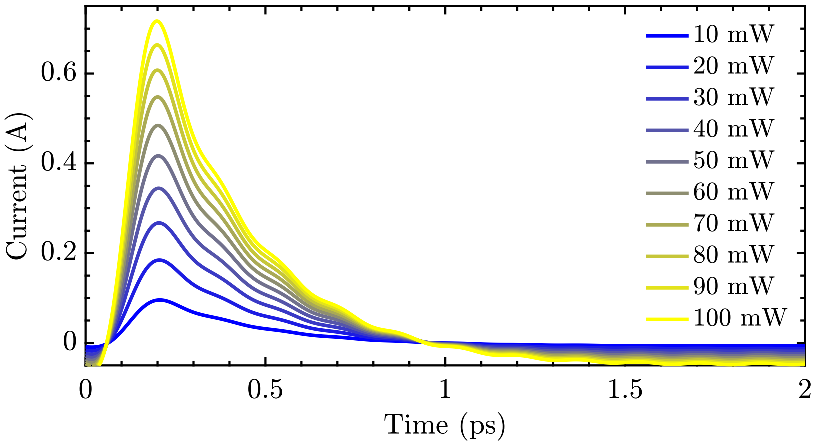

(b) Currents on the gap

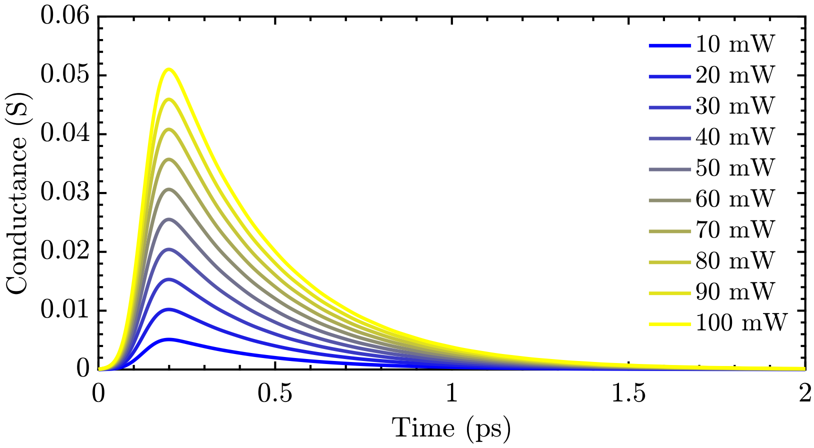

(c) Conductance of the gap

Figure 4.6: Voltages and currents with the relative conductances on the photoconductor gap as function of time for various laser power levels.

In order for the model to predict more accurately the power radiated, one could vary the mobility as function of the different laser power levels as shown in Figure 4.9, although this procedure results in an unrealistic characterization of the same.

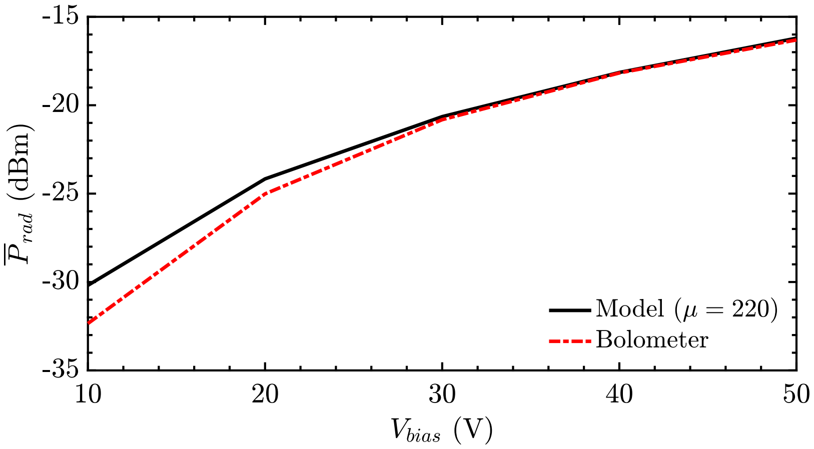

Figure 4.7: Average power radiated estimated by using the Norton equivalent circuit model and measurements as function of the bias voltage applied on the passive structure. The average laser power considered is $\overline{P}_{laser} = 30$ mW. The mobility is measured in cm^{2}V^{-1}s^{-1}.

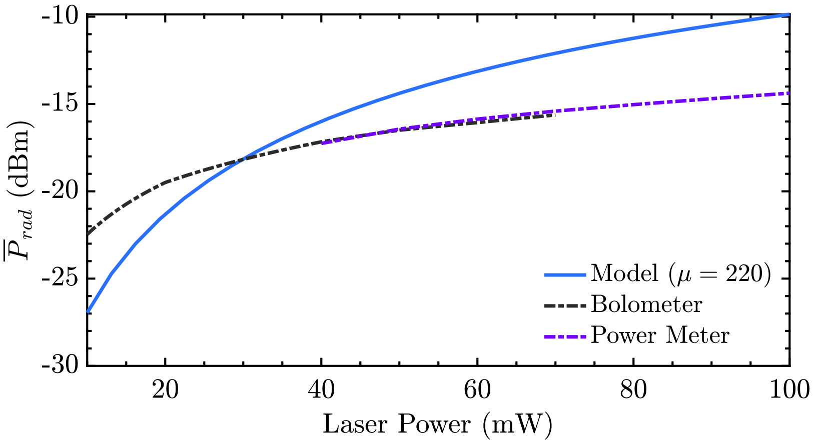

Figure 4.8: Average power radiated as a function of the laser power. The Norton model is compared with the measured power (dashed lines) for a bias voltage $V_{bias} = 40$ V. The mobility is measured in cm^{2}V^{-1}s^{-1}.

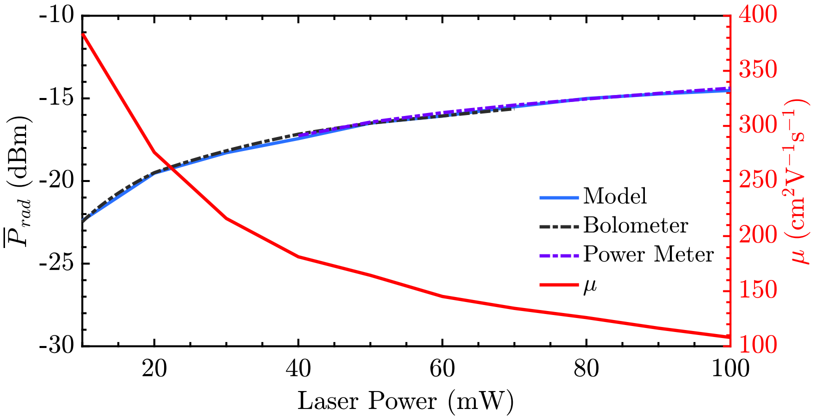

Figure 4.9: Average power radiated as a function of the laser power. The Norton model uses a fitted free carriers' transient mobility (μ line).

4.2.3 Norton - Limits of the Model

The fact that one would have to fine tune the value of the mobility to obtain a good match between the measured power and the model implicitly means that the model is of limited applicability. The other criticality, addressed in section 4.4, is the calculation of the generator impedance Z_g. Since there is no easy way to compute it, (4.7) was used to derived a zero*th* order approximation. As it will be apparent later in section 4.4, a proper choice of this impedance makes the model very accurate for various laser power levels.

4.3 Time Domain Model in CST

In this section a new and improved description of the radiation mechanisms of the PCA in transmission is proposed. It is based on the time domain solver of CST MWS [5]. Numerical simulations are performed to model the PCA as a passive component and introducing the semi-conducting gap conductivity temporal and spatial distribution as a separate material impulse response. As such, the model accounts for the interaction between the photoconductor gap and the hosting passive structures only via Maxwell's equations. The model's results are presented and analyzed, and compared to what was obtained in subsection 4.2.2 for the Norton Equivalent Circuit Model [4]. The time domain procedure allows for a better understanding of the phenomena that occur subsequently to a laser beam excitation on a semiconductor and can be particularly useful in view of a design in which the optimization and maximization of the power radiated is prioritized. To the author's knowledge, it has not been published a guide on how to simulate PCAs in CST, therefore subsection 4.3.1 is dedicated to this topic.

4.3.1 CST - Bias Sources

In the PCA problem at hand there are two electromagnetic sources to be considered. The bias at very low frequencies, in the order of the MHz, and the laser source. The latter is not viewed in our CST simulations as a source but can be more appropriately described as a variation of the properties of the gap medium, while the former is truly introduced in CST as an electromagnetic source. Since the time scales involved in the biasing and the pulsed variation of conductivity differ substantially, its purpose consists only in guaranteeing that a certain number of charges are available at the antenna terminals when the conductivity transient occurs. In a realistic model of the biasing, one would have to describe the complex circuitry used to isolate the high frequencies from the low frequencies (e.g. bulky inductors). Their simulations, together with the time scales required by the PCA transients, would render the geometry to be analyzed impossibly large to be solved numerically in reasonable times. Accordingly, rather than simulating the actual biasing of the circuit, we have decided to represent a simplified biasing phenomena that is analogous to the charging of a capacitor with which one can approximate the PCA before the optical excitation becomes active. Since CST does not allow to include charges as sources, we found that in order to induce a certain biasing in a passive structure one needs to slowly increase the impressed voltage. The time scales in which the charging needs to be performed require waiting until the current and the corresponding electric field associated to the moving charges in the conductors are stabilized. An example of the biasing signal is shown in Figure 4.10.

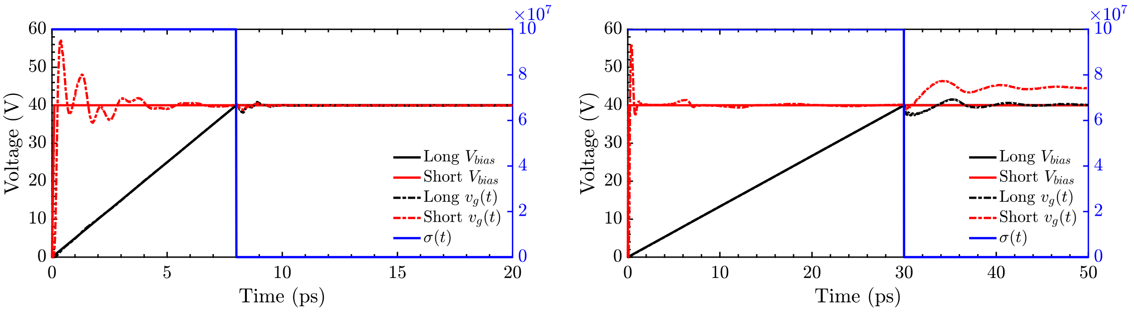

(a) Small structure **(b)** Bigger structure

Figure 4.10: Biasing signal for $V_{bias} = 40$ V. The biasing is shown for two structure, *Small structure* and *Bigger structure*, where the latter has the same geometry of the former except it is 6 times longer. In both cases the full black and red lines refer to a slow and a fast biasing signal, respectively, whereas the dashed lines refer to the voltage seen on the gap as a result of the biasing. The blue line, $\sigma(t)$, indicates the time-varying conductivity of the strip connecting the passive structure with the metallic zones where the impressed voltage is applied. It can be observed that for a longer biasing time the gap voltage presents less oscillations and, therefore, it allows for a better description of a stable bias signal once the open circuit is induced between the ports and the passive structure.

Once a stable electric field configuration is achieved, rather than removing the impressed voltage, we found it convenient to assume that the overall metallic passive structure is composed of three components. The metallic zones where the impressed voltage is applied (electrodes), the passive structure, and a strip connecting the two as shown in Figure 4.11.

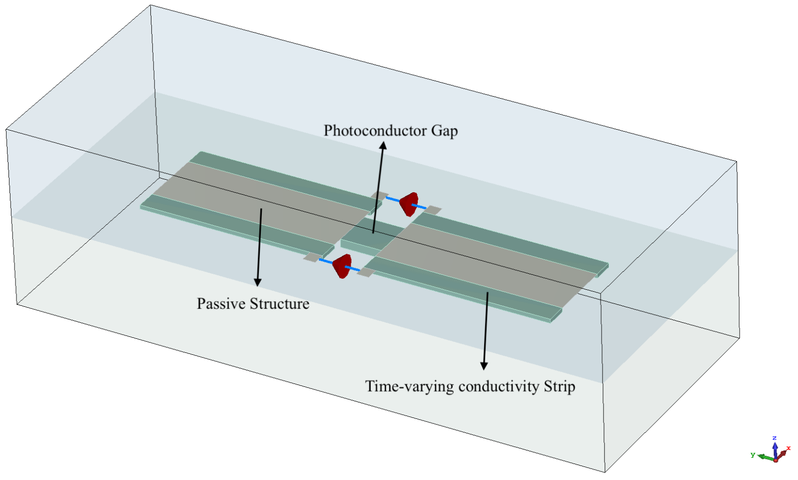

Figure 4.11: Overview of the PCA. The CST modeling comprises three main components needed for the simulation: the electrodes, the passive structure and a strip connecting the two.

The strip is assumed to be artificially characterized by a time-varying electrical conductivity (which varies from $\sigma_1 = 10^8$ (S/m) to $\sigma_2 = 0$), such that the impressed voltage is entirely disconnected from the charged antenna gaps at a defined time T_1. At a time $t = T_1$ the CST configuration is equivalent to the one of a charged capacitor with a predefined voltage at the PCA terminals. At a later time $T_2 > T_1$ the photoconductor gap becomes excited and thus a transient rearrangement of the charges, voltages and current occurs in the structure. An example of the electrical conductivity induced by the excitation on the gap is shown in Figure 4.12.

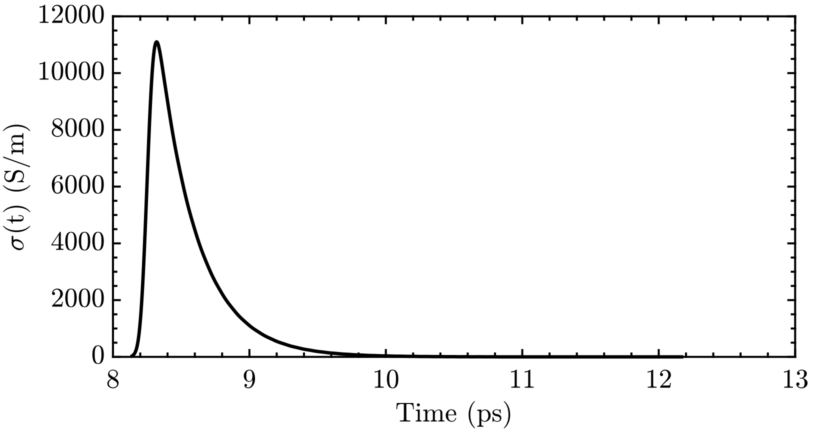

Figure 4.12: Time-varying electrical conductivity of the gap. The time scale refers to the structure biased as in Figure 4.10a.

The transient duration depends mainly from the assumed properties of the material and laser. Moreover, a non-negligible contribution is given by the impulse response of the antenna which modulates the signal by imposing its boundary conditions. The impulse response can be simply demonstrated, as discussed in Appendix C, to be the anti Fourier-transform of the input impedance of the antenna. CST takes into account all these information in providing the time evolution of the electromagnetic fields in the structure that are simulated.

4.3.2 CST - Simulation of the Power Radiated

The aim of these simulations is the quantification of the average power radiated which typically depends from various factors such as the geometry and dimension of the structure, the properties of the laser and photoconductive gap, and the overall efficiency of the quasi-optical system. Since it is known that these simulations can be quite cumbersome to perform, and the extraction of the power radiated by setting far-field monitors on the bandwidth considered can consistently degrade the speed and accuracy of the results, hereby it is reported an alternative procedure which improves greatly both the former and the latter. In particular, this procedure is intended to be used in a preliminary stage of the design where the evaluation of the directivity of the patters radiated by the structure is not prioritized, i.e., the problem of describing the power generated and radiated by the structure is decoupled in two sub-problems and only the former is effectively quantified. Furthermore, it is important to notice that these simulations describe accurately the power in proximity of the photoconductor gap, although fail to account for a full propagation and leakage (in the case of a leaky structure) of the pulse along the antenna.
The energy spectral density E_s associated with the antenna radiation is a real quantity for the Hermitian symmetry of the spectra and can be written as

$$E_s = \frac{1}{2\pi}\int_{-\infty}^{\infty} |I_a(\omega)|^2 Z_a(\omega) d\omega \tag{4.14}$$

Moreover, the laser feeds periodically the photoconductor gap with a period $T_p = 1/f_p$, thus the average power radiated can be computed with the available energy spectral density E_a which accounts for the efficiency of the quasi-optical system η_{op} as $E_a = E_s\eta_{op}$, therefore

$$\overline{P}_{rad} = \frac{E_a}{T_p} \tag{4.15}$$

The simulator yields the quantity integrated in (4.14), i.e., the power radiated in function of the frequency which can be obtained by setting the far-field monitors in the bandwidth of interest. Since the impedance of the structure can be evaluated separately, one could just extract the time-varying current on the gap from the simulator and perform the remaining computations on a separate programming tool. This solution is advantageous because it essentially eliminates the problem of simulating at lower frequencies, since the transient simulation works regardless of the bandwidth and frequency range considered. As a result, bigger structures that would be required in order for the current to leak in the propagation can be reduced in size by considering higher frequencies. In such a way the mesh cells count can be greatly reduced without impacting on the accuracy of the simulation. The procedure is exemplified for a dipole in Figure 4.13.

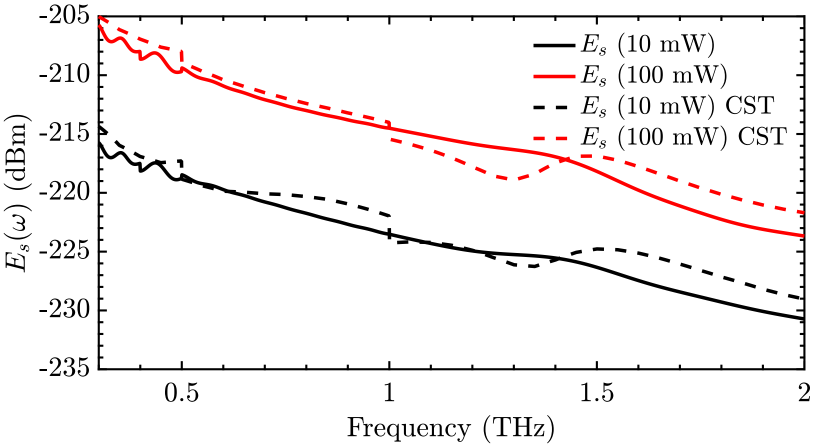

Figure 4.13: Energy spectral densities $E_s(\omega)$ as function of the frequency of a dipole with width $w = 10$ μm, gap dimensions $W_x = W_y = 10$ μm and length $L_d = 2$ mm. The quantities shown are equivalent to the integrand described in (4.14). The full lines depict the energy computed via the faster procedure, i.e., the frequency considered for the simulation is arbitrarily chosen to be $[1 - 1.5]$ THz and only the time-varying current is extracted from the simulator, whereas the impedance, $Z_a(\omega)$, is computed in a separate simulation. The dashed lines represent the radiated power computed via CST MWS by setting multiple far-field monitors in the bandwidth considered. In particular, three simulations have been performed, each for a different bandwidth: $[0.3 - 0.5]$ THz, $[0.5 - 1.0]$ THz and $[1.0 - 2.0]$ THz.

4.3.3 CST - Model Validation

Referring to the generalized Parseval's theorem in (4.9), $v_a(t)$ and $i_a(t)$ are the time-varying voltage and current, respectively, observed on the photoconductor gap. The voltage and the currents are assumed to be well described via CST simulations. In particular, the currents and voltages are recovered by defining, respectively, a current and voltage monitor on the gap as in Figure 4.14.

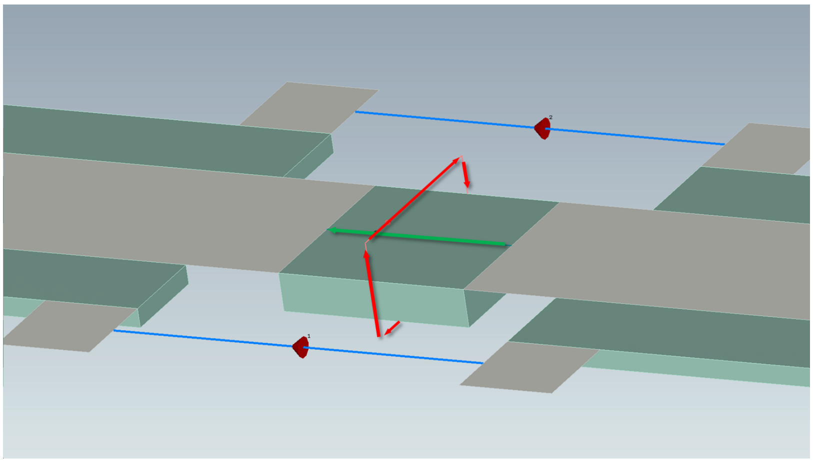

Figure 4.14: The voltages and currents are derived in CST by defining a voltage monitor on the gap in the direction of the ports (green arrow) and a current monitor around the gap (red arrow).

It must be noted that the quantity obtained via the voltage monitor corresponds to the voltage drop on the gap, which does not satisfy the Parseval's theorem in (4.9). Thus, the voltage on the gap is shown as in Figure 4.6 by considering $v_a(t) = V_{bias} - v_{cst}(t)$ where $v_{cst}(t)$ is the voltage obtained by defining the voltage monitor in CST (see Figure 4.15).

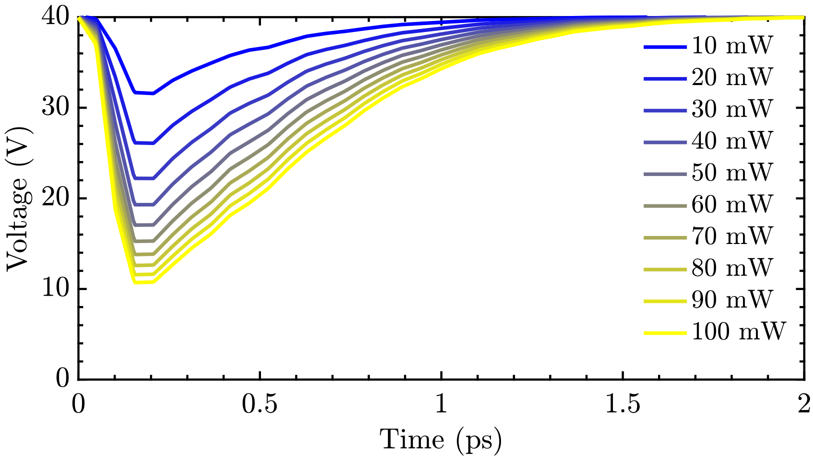

(a) $v_{cst}(t)$

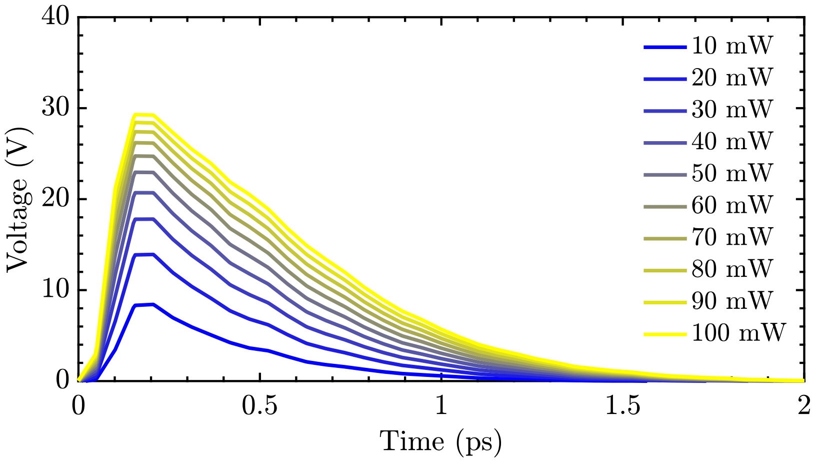

(b) $v_a(t)$

Figure 4.15: Time-varying voltage $v_{cst}(t)$ obtained from CST and gap voltage $v_a(t)$ computed as $V_{bias} - v_{cst}(t)$.

The results in Figure 4.17 are pertinent to the quantities reported in Table 4.2.

Table 4.2: CST model parameters of laser and semiconductor material. The parameters refer to the setup described in [6]. In particular, τ_p is the half-power pulsewidth, f_{laser} is the frequency associated with the energy band-gap, f_p is pulse repetition rate of the laser, D_{laser} is the focused laser beam diameter and η_{so} is the spillover efficiency (the laser beam profile is Gaussian); $W_{x,y}$ and W_z are the transversal and longitudinal dimensions of the photoconductor gap, respectively, α is the laser absorption coefficient at the semiconductor material, τ_r is the charge carrier lifetime, μ is the free carriers' transient mobility and Γ is the optical Fresnel reflection coefficient at the air-semiconductor interface.

Laser	**Semiconductor**
$\tau_p = 0.1$ ps	$W_x = W_y = 10\ \mu$m
$f_{laser} = 375$ THz	$W_z = 2\ \mu$m
$f_p = 80$ MHz	$\alpha = 10^6\ \text{m}^{-1}$
$D_{laser} = 14.5\ \mu$m	$\tau_r = 0.3$ ps
$\eta_{so} = 0.34$	$\mu = 420\ \text{cm}^2\text{V}^{-1}\text{s}^{-1}$
	$\Gamma = \sqrt{0.3}$

The geometry of the structure simulated refers to Figure 4.2. The biasing signal (as explained in subsection 4.3.1) is shown in Figure 4.16.

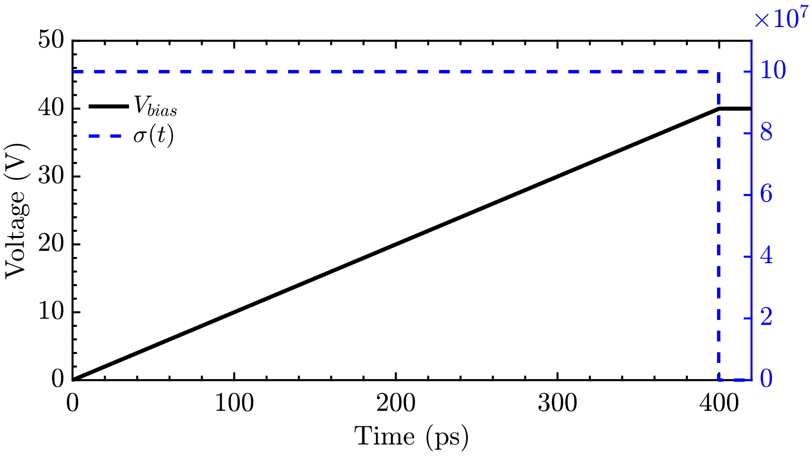

Figure 4.16: Biasing signal for $V_{bias} = 40$ V of the bow-tie.

In Figure 4.17 is possible to notice that for increasingly higher laser powers, an increment of the conductance, and therefore a decrease in resistivity, does not translate into a linear variation of the current and voltage. This behavior can be attributed to a phenomenon of saturation, i.e., one can consider the system semiconductor-antenna as a non-linear device which exhibits a compression point for high enough input power. Since the saturation is critical for a complete analysis and for an accurate radiated power estimation of these devices, it is discussed thoroughly and explained in section 4.5.

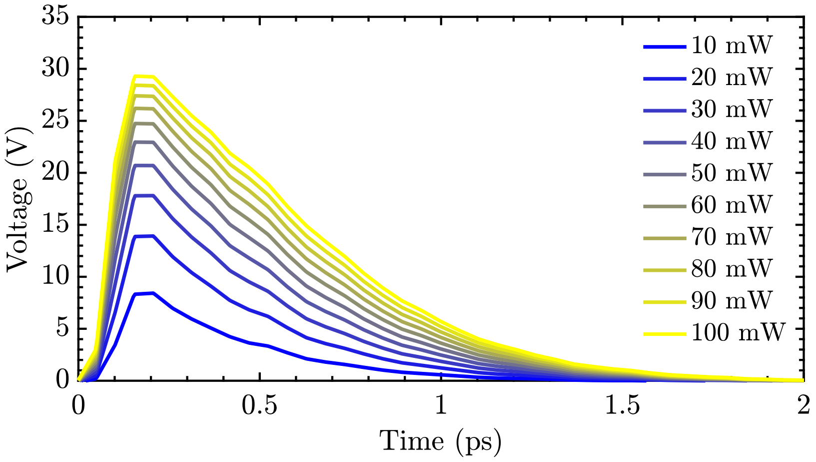

(a) Voltages on the gap

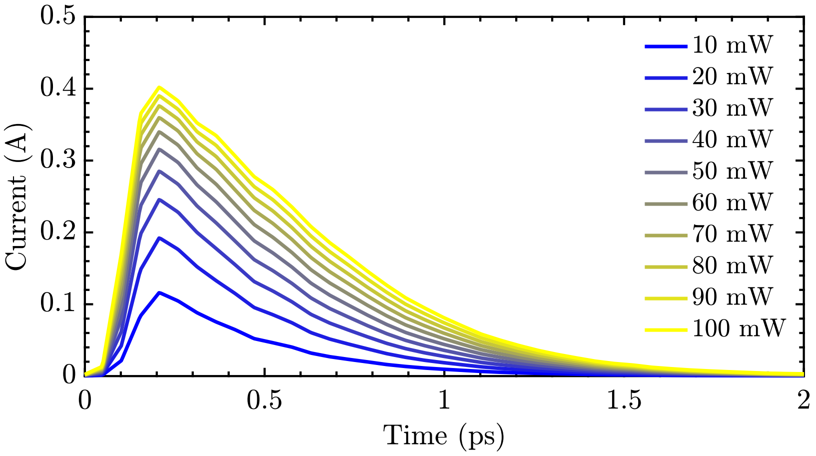

(b) Currents on the gap

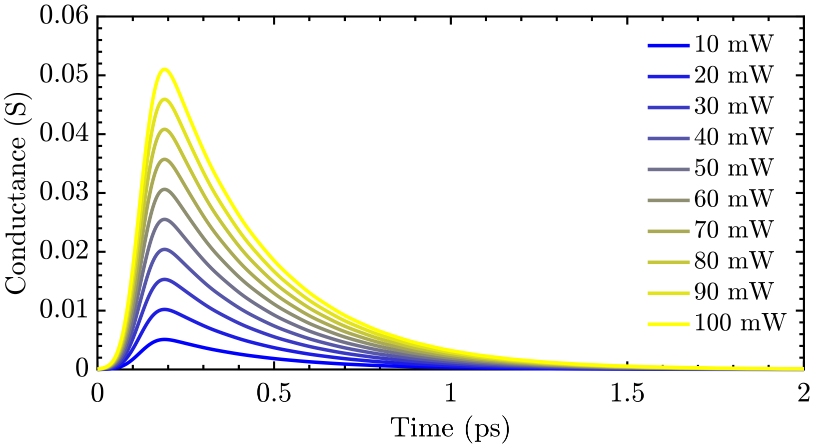

(c) Conductance of the gap

Figure 4.17: Voltages and currents with the relative conductances on the photoconductor gap as function of time for various laser power levels.

The energy spectrum densities predicted by the CST model for a mobility $\mu = 420\ \mathrm{cm^2V^{-1}s^{-1}}$ are shown in Figure 4.18.

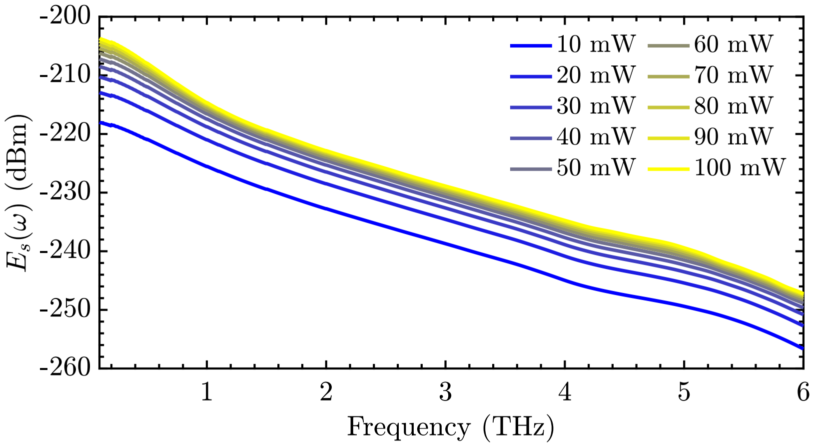

Figure 4.18: Energy spectrum densities as function of the frequency for various laser power levels.

The average power radiated estimated with the CST Model as function of the bias voltage for an average laser power of $\overline{P}_{laser} = 30$ mW is shown in Figure 4.19.

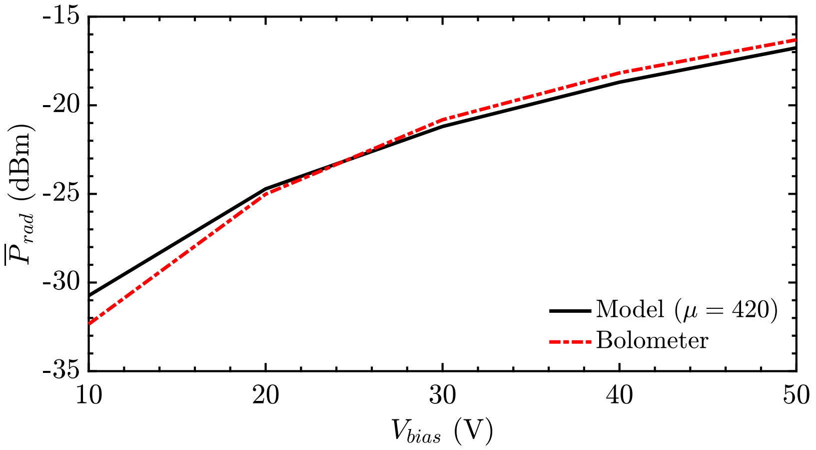

Figure 4.19: Average power radiated estimated by using the CST model and measurements as function of the bias voltage applied on the passive structure. The average laser power considered is $\overline{P}_{laser} = 30$ mW. The mobility is measured in cm^{2}V^{-1}s^{-1}.

The related average power is shown in Figure 4.20 and compared with the measurements. It is possible to see that the CST model, even by maintaining a constant mobility for different laser power levels, achieves a very high accuracy especially at laser power levels higher than 20 mW.

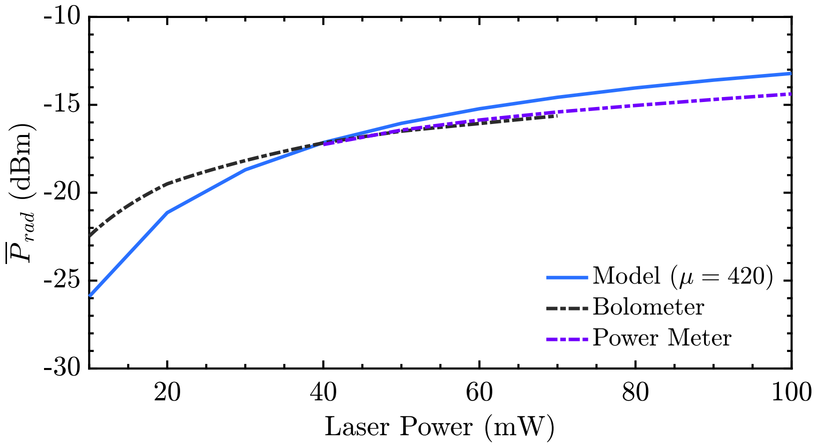

Figure 4.20: Average power radiated and measurements as a function of the average laser power. The bias voltage considered is $V_{bias} = 40$ V. The mobility is measured in $\mathrm{cm}^2\mathrm{V}^{-1}\mathrm{s}^{-1}$.

For completeness, Figure 4.21 shows the CST model results for different bias voltages.

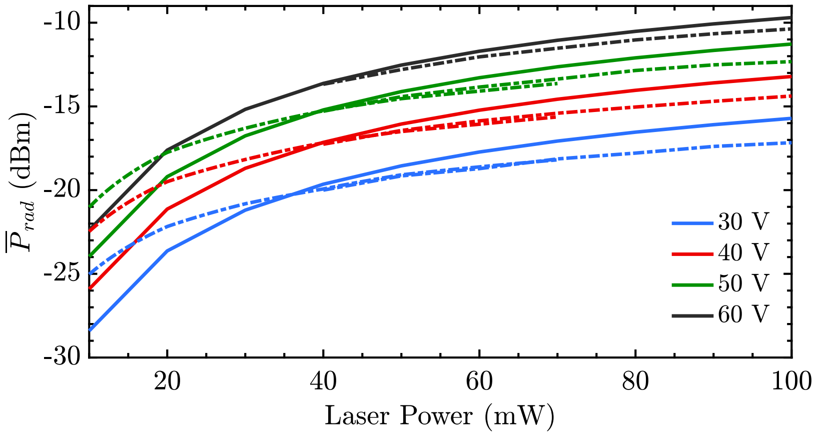

Figure 4.21: Average power radiated as a function of the laser power for different bias voltages. The full lines represent the CST model and the dashed lines represent the measurements of the bolometer and power meter.

4.4 Revised Norton Equivalent Circuit

It this section it is proposed a revised version of the Norton Equivalent Circuit. In (4.7) the generator impedance has been defined as $1/g_0$, with g_0 defined in (4.8) as the average of the conductance in an arbitrarily time interval τ_σ, taken where $g(t)$ is above 1/100 of its peak. A more appropriate choice of g_0 involves considering the time interval τ_σ comparable to the charge carrier lifetime τ_r, which approximately corresponds to average the $g(t)$ when it is above 1/3 of its peak (see Figure 4.22). The newly defined impedance generator Z_g is exemplified in Figure 4.23 for various mobilities. It is possible to observe that the impedance is much lower than the one shown in Figure 4.4 and therefore it becomes comparable and even lower than the antenna impedance (see Figure 4.1).

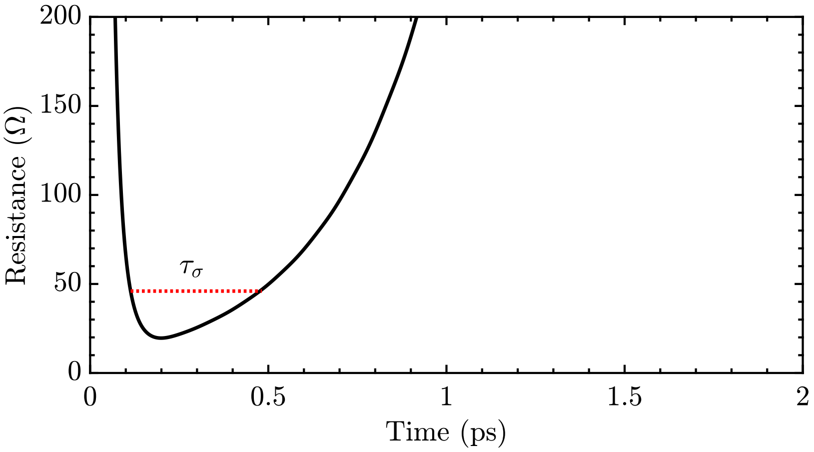

Figure 4.22: Resistance of the photoconductor material for an average laser power of $\overline{P}_{laser} = 100$ mW and a mobility of 420 cm^{2}V^{-1}s^{-1}. The straight line refers to the newly defined time interval τ_σ taken approximately where $g(t)$ is above 1/3 of its peak.

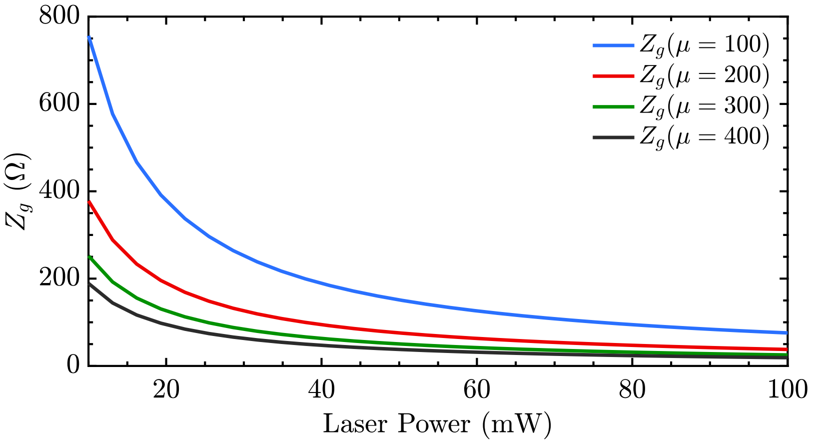

Figure 4.23: Revised Norton generator impedance in function of the laser power. The mobility is measured in cm^{2}V^{-1}s^{-1}.

The lower value of generator impedance compared to the antenna impedance is critical to observe the saturation behavior at higher laser power levels. The voltages and currents computed as in Figure 4.6 are shown in Figure 4.24. As expected, the voltages and currents exhibit saturation for an increase in the laser power level.

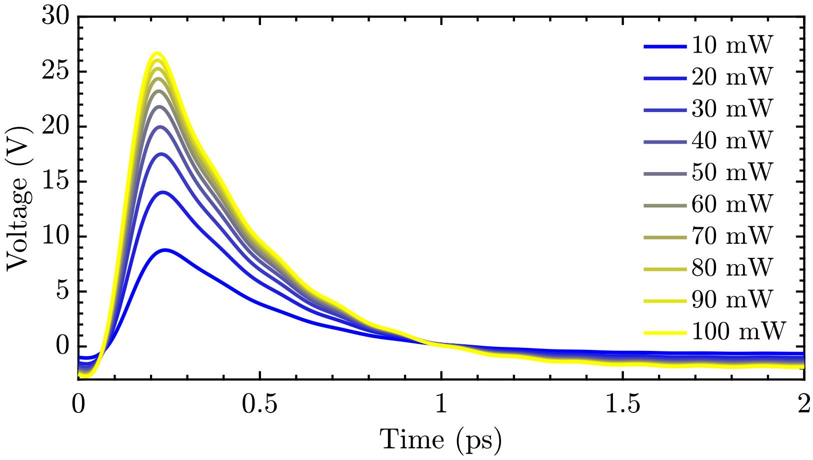

(a) Voltages on the gap

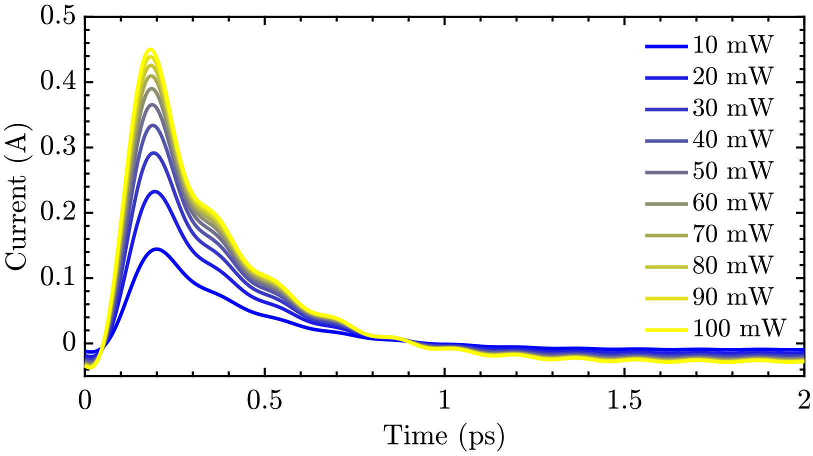

(b) Currents on the gap

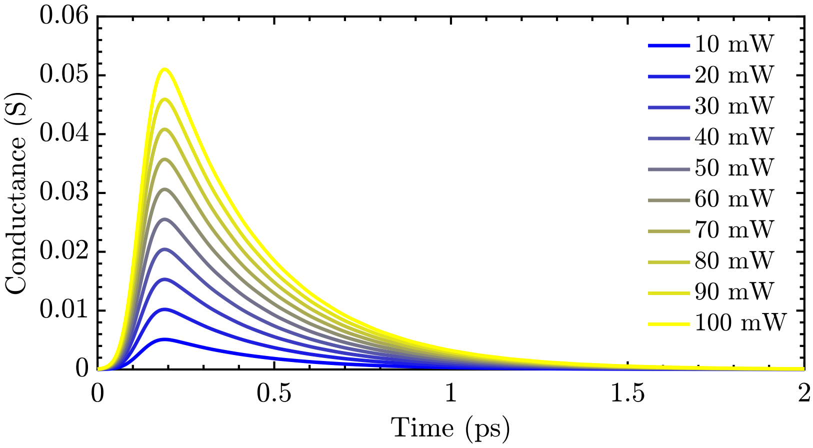

(c) Conductance of the gap

Figure 4.24: Voltages and currents with the relative conductances on the photoconductor gap as function of time for various laser power levels.

Figure 4.25 shows the available energy spectral density $E_a(\omega) = E_s(\omega)\eta_{qo}(\omega)$ of the revised Norton equivalent circuit model together with the original one, the CST model and the measurements (see [12, p.1656] for the measured spectrum).

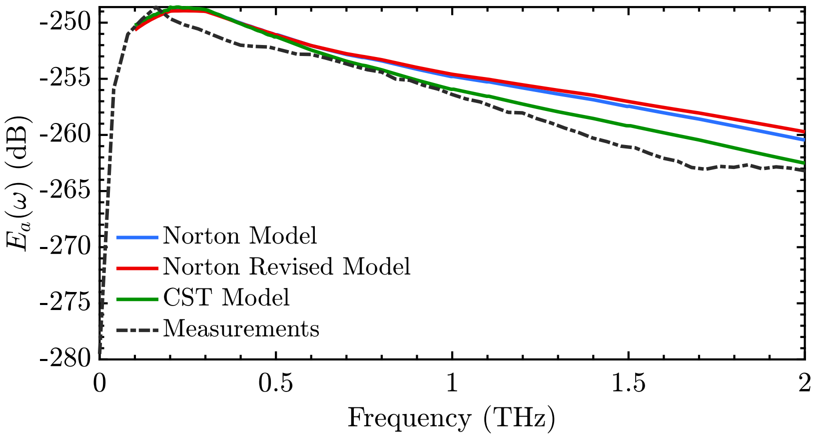

Figure 4.25: Energy spectral density $E_a(\omega)$ of the presented models and measurements as function of the frequency. The laser power considered is 30 mW and the bow-tie is biased at $V_{bias} = 40$ V.

Figure 4.26 shows the resulting average radiated power together with the result obtained for the CST model (using the same mobility) and the measurements. It is possible to observe that the Norton revised model is more accurate than the CST model at both lower and higher laser power levels.

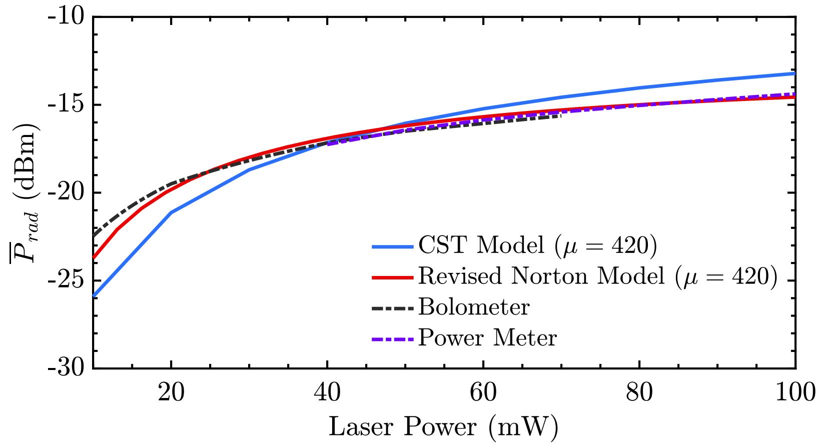

Figure 4.26: Average radiated power as function of the laser power level. The mobility is measured in cm^{2}V^{-1}s^{-1}.

The revised Norton equivalent circuit model constitutes an improvement on the state-of-the-art. In particular, the model predicts very accurately the average power radiated regardless of the laser power level considered and it offers a standardized way (frequency domain) to analyze any kind of antenna compared to other hybrid models ([1], [2]) which, although very precise, lose validity for dispersive and resonant antennas, i.e., being formulated in the time-domain, they only allow an average resistance of the antenna considered which works well for antennas such as the bow-tie, but fail to characterize other structures with a significant variation of the impedance in frequency. Furthermore, an accurate modeling of the generator impedance Z_g paves the way for better designs of complex structures such as connected arrays.

4.5 Parametric Analysis of the CST model

A thorough understanding of the spectral components of the signals propagating on the structure plays an important role in the maximization of the power radiated. Although the measurements are available only for limited sets parameters of laser and semiconductor, once the model is verified on one set, one can confidently vary these values for optimization purposes. As an example, one can refer to Figure 4.27 to visualize these spectral components. The figures show the gap currents in time domain with their relative Fourier-transform for different charge carrier lifetimes τ_r and half-power pulse-widths τ_p. In particular, α and β are multiplicative factors of τ_p and τ_r, respectively, with initial values which are referred to $\tau_r = 0.3$ ps and $\tau_p = 100$ fs, as done in the measurements. The spectral components of the current depend from the conductance (see Figure 4.17c for an example of the conductance) which is related to the envelope of the average laser power density $\widetilde{s}(t)$ and the impulsive response of the material $h(t)$ by a convolution, as shown in (4.2). It is possible to see that the low frequency components of the current are dominated by τ_r, i.e., a longer charge carrier lifetime corresponds to a higher magnitude at lower frequencies. The high frequency components are instead dominated by τ_p, i.e., a shorter half-power pulse-width corresponds to a higher magnitude at higher frequencies. It is therefore apparent that these two parameters play a central role in the maximization of the power radiated in certain bandwidths.

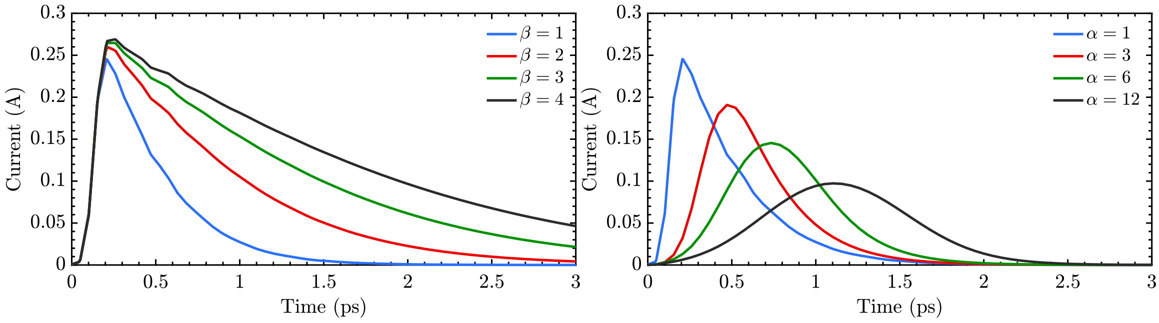

(a) Time domain ($\alpha = 1$) **(b)** Time domain ($\beta = 1$)

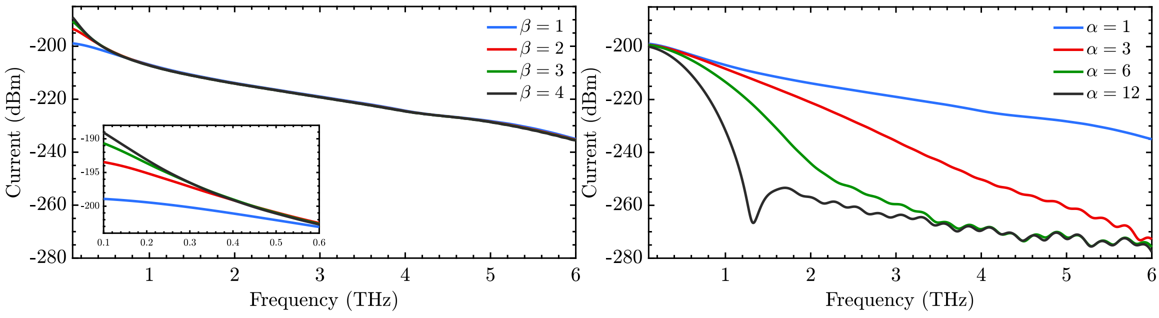

(c) Frequency domain ($\alpha = 1$) **(d)** Frequency domain ($\beta = 1$)

Figure 4.27: Current on the gap as function of time and frequency. The current is derived from CST, using a laser power $\overline{P}_{laser} = 30$ mW and the parameters in Table 4.2. The antenna is biased at $V_{bias} = 40$ V. The parametric curves are in function of α and β which are multiplicative factors of τ_p and τ_r, respectively, with initial values ($\alpha = 1$ and $\beta = 1$) referred to $\tau_p = 100$ fs and $\tau_r = 0.3$ ps which correspond to the measurements. As an example, $\alpha = 1$ and $\beta = 2$ indicate $\tau_p = 100$ fs and $\tau_r = 0.6$ ps. In Figures 4.27b and 4.27d it is assumed $\beta = 1$ and in Figures 4.27a and 4.27c it is assumed $\alpha = 1$.

Figure 4.28 shows the corresponding average power radiated as function of the laser power.

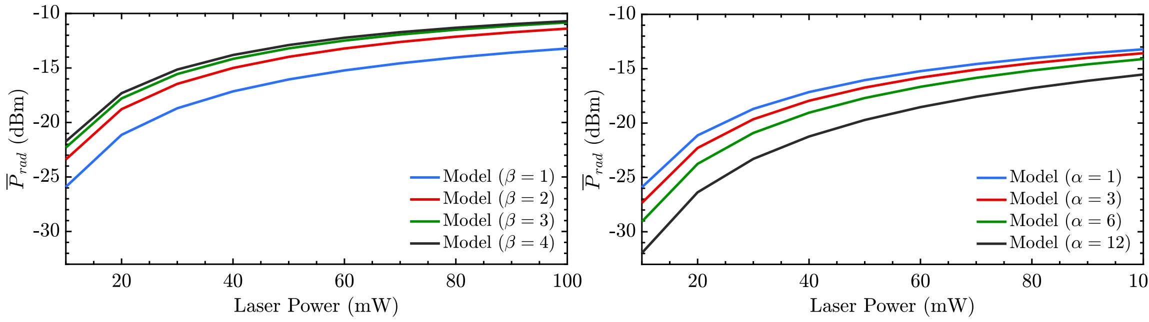

(a) $\alpha = 1$ **(b)** $\beta = 1$

Figure 4.28: Average power radiated as a function of the laser power. The current is derived from CST, using a laser power $\overline{P}_{laser} = 30$ mW and the parameters in Table 4.2. The antenna is biased at $V_{bias} = 40$ V. The parametric curves are in function of α and β which are multiplicative factors of τ_p and τ_r, respectively, with initial values referred to $\tau_p = 100$ fs and $\tau_r = 0.3$ ps, as done in the measurements. As an example, $\alpha = 1$ and $\beta = 2$ indicate $\tau_p = 100$ fs and $\tau_r = 0.6$ ps. In Figures 4.28a and 4.28b it is assumed $\alpha = 1$ and $\beta = 1$, respectively.

Having analyzed the signals involved in the laser excitation of the photoconductor gap, we can now focus on the saturation phenomena seen previously in Figure 4.17. Since CST is not able to model the properties of the semiconductor, we can confidently attribute the saturation as function of the laser power level seen by the simulator to the availability of charges on the metal of the antenna coupled to the photoconductor gap. When the laser impinges on the semiconductor gap, only the charges in proximity of the gap itself are able to react. Since the laser impulse lasts for 100 fs, the other charges deposited on the metal of the antenna propagate a signal limited by the velocity of light in a dielectric with an effective permittivity of approximately $\sqrt{(\varepsilon_r + 1)/2}$ where ε_r is the permittivity of the denser dielectric (silicon). The effect can be clearly seen in Figure 4.17a where, after the initial voltage drop due to the excitation of the laser, the voltage returns to (almost) the previous level of bias. This situation occurs when the antenna has dimensions that are big enough such that only a small percentage of the charges are interested by the discharge, and thus only a limited portion of the total current gets radiated.

We now we pose ourself in a situation where the dimensions of the antenna, and therefore the area of metal present, are so small that the current induced by the laser excitation depletes immediately almost all the charges deposited on the metal. The amount of metal is then parametrically increased, as shown in Figure 4.29, in order to be able to observe what was previously described.

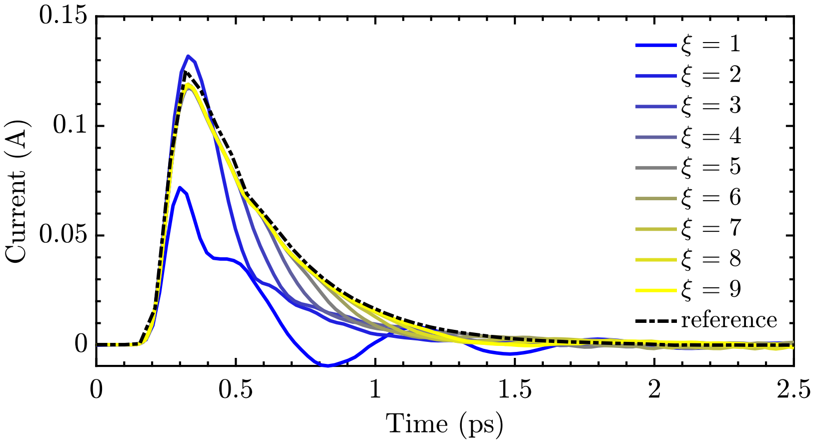

(a) Currents on the gap

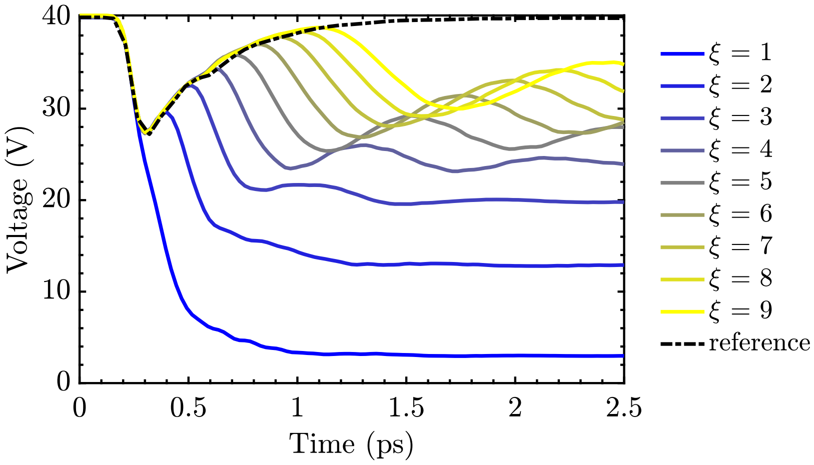

(b) Voltages on the gap

Figure 4.29: Voltage and current on the photoconductor gap as function of time. The parameter ξ indicates a small and linear increase in the longitudinal dimension of the antenna. In particular, $\xi = 1$ a situation where the antenna dimensions considered are such that the current induced by the laser excitation depletes almost all the charges deposited on the metal. The labels *reference* indicate the voltages and currents on the gap obtained with a much bigger structure.

It is possible to see that the currents converge to the reference value after a few iterations whereas it is not the case for the voltages. In the first iteration the antenna is completely depleted of the charges, and therefore this behavior can be seen in analogy with a capacitor which discharges itself with a certain time constant $\tau = RC$. In the following iterations the voltage tends to the reference line, but it is evident that the structure is not big enough to regain the same level of bias after the first discharge. It is therefore apparent that for higher laser powers more current is allowed to flow across the gap due to the lower resistivity, but the amount that can actually go through is limited by the velocity at which the charges on the metal of the antenna can react. This conclusion has great relevance for PCAs design since it implicates that the only significant part of the passive structure (the *active area*) is the one immediately in proximity of the photoconductor gap. This is exemplified in Figure 4.30 which shows the currents and voltages of the bow-tie as in Figure 4.17 compared with two dipoles with the same length of the latter and different widths (see Figure 4.32) computed with the CST model. Moreover, Figure 4.31 shows the voltages and currents derived from the Norton revised model by anti Fourier-transforming (4.10) and

(4.11), which essentially highlights the importance of employing the EM simulator for the analysis of the transients. The laser and semiconductor parameters of the dipoles are kept the same as in Figure 4.17 and are summarized in Table 4.2.

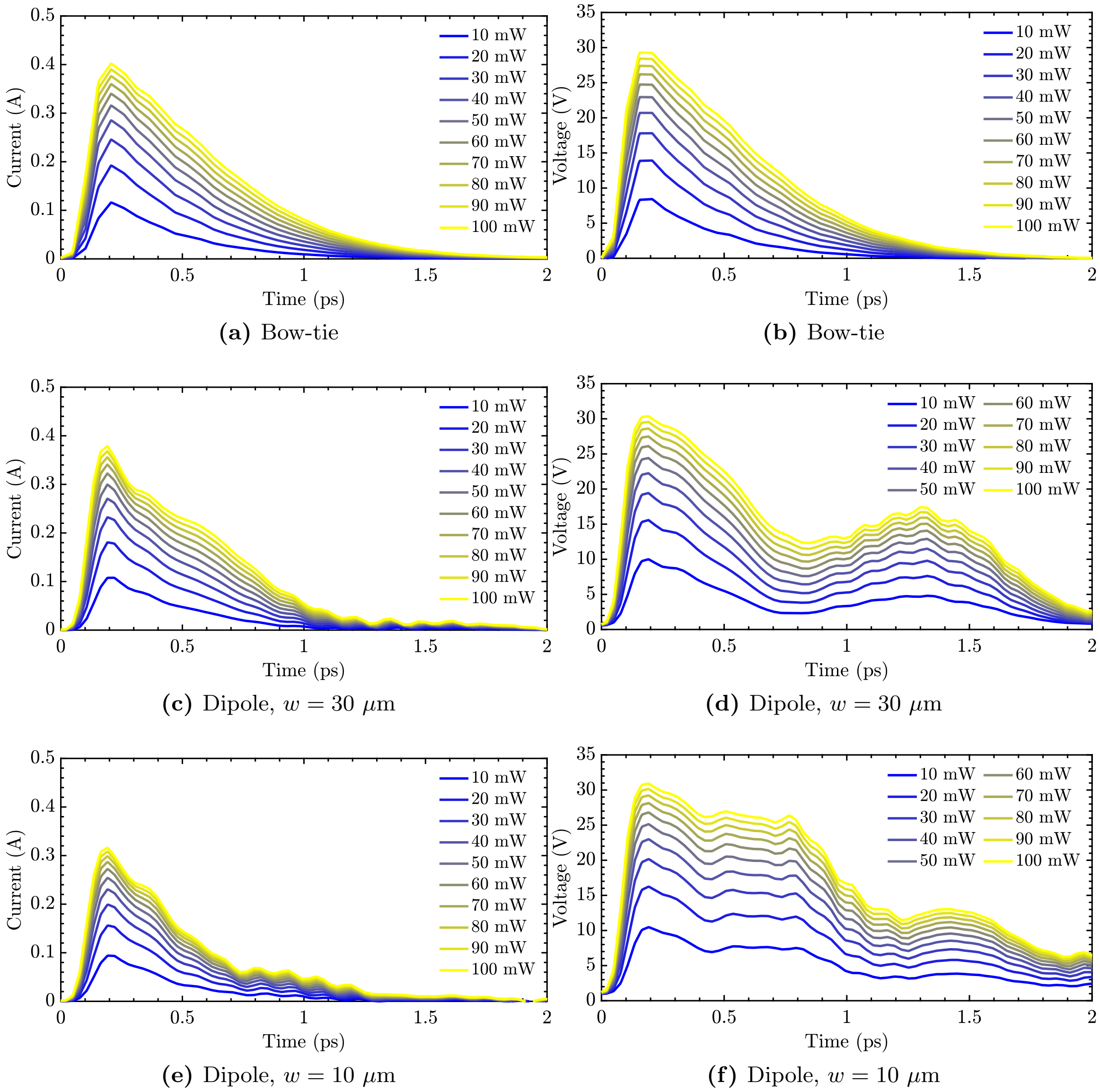

(a) Bow-tie **(b)** Bow-tie

(c) Dipole, $w = 30$ μm **(d)** Dipole, $w = 30$ μm

(e) Dipole, $w = 10$ μm **(f)** Dipole, $w = 10$ μm

Figure 4.30: Voltages and currents derived from the CST model as function of time for the reference structure (bow-tie) and two dipoles with the same length $L_d = 2$ mm which differ only in width w as shown in Figure 4.32.

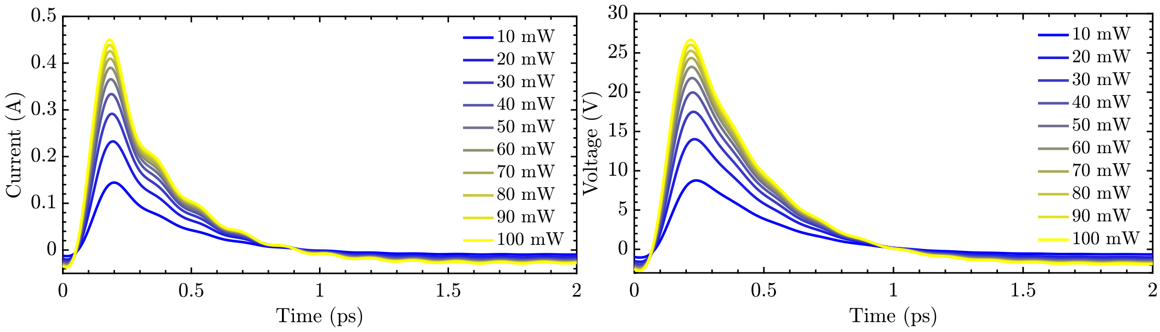

(a) Bow-tie **(b)** Bow-tie

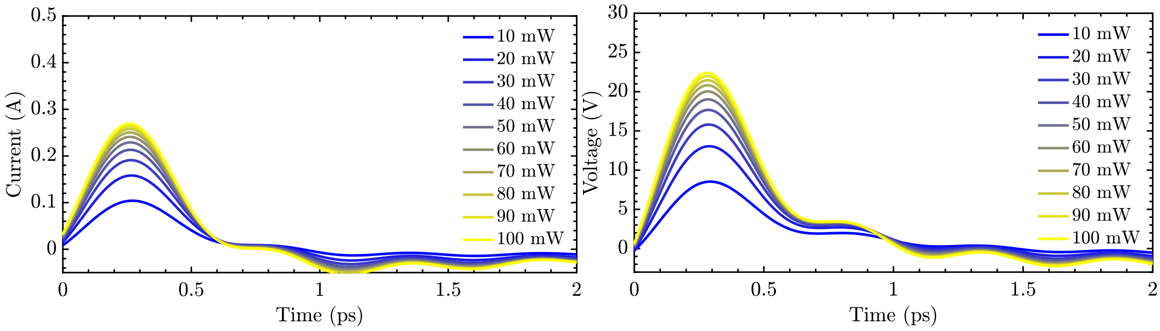

(c) Dipole, $w = 30\ \mu$m **(d)** Dipole, $w = 30\ \mu$m

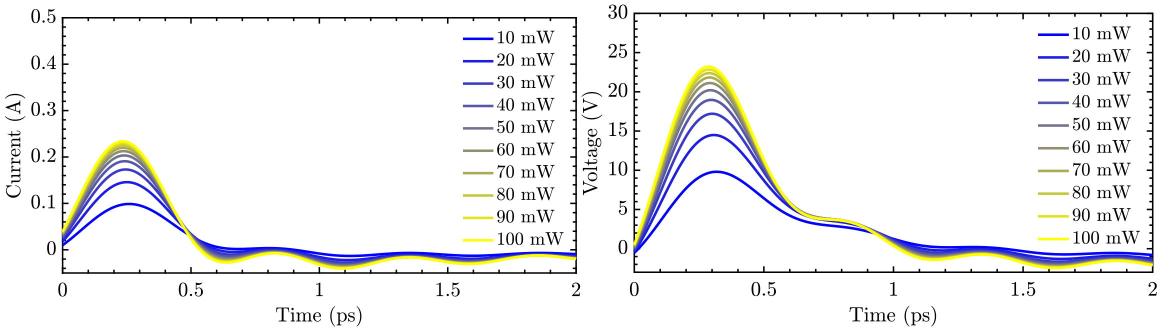

(e) Dipole, $w = 10\ \mu$m **(f)** Dipole, $w = 10\ \mu$m

Figure 4.31: Voltages and currents as function of time derived from the Norton revised model by anti Fourier-transforming (4.10) and (4.11) for the reference structure (bow-tie) and two dipoles with the same length $L_d = 2$ mm which differ only in width w as shown in Figure 4.32.

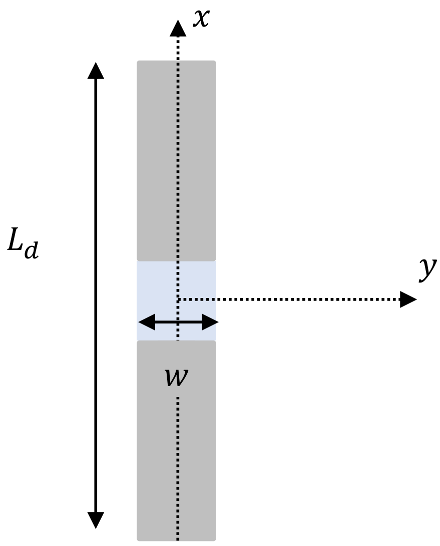

Figure 4.32: Dipole with cross section w, gap dimensions $W_x = W_y$ and length L_d. In Figure 4.30 the two dipoles have a width $w = 10$ μm and $w = 30$ μm, a gap dimension $W_x = W_y = 10$ μm and a length $L_d = 2$ mm.

The energy spectral densities $E_s(\omega)$ derived via the CST and Revised Norton equivalent circuit model for a laser power $\overline{P}_{laser} = 30$ mW and a bias voltage $V_{bias} = 40$ V are shown in Figure 4.33.

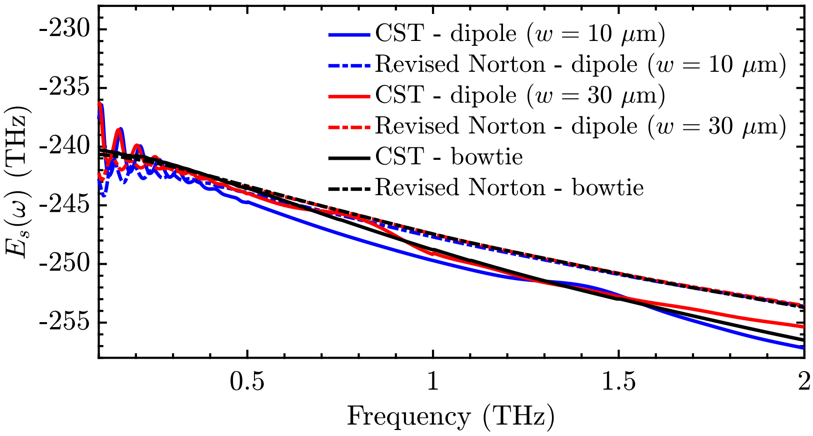

Figure 4.33: Energy spectral densities as a function of frequency computed via the CST method and the revised Norton equivalent circuit method. The laser power and bias voltage considered are $\overline{P}_{laser} = 30$ mW and $V_{bias} = 40$ V, respectively.

The average radiated powers computed with the revised Norton equivalent circuit and the CST model for the bow-tie and the two dipoles in Figure 4.32 are shown in Figure 4.35. The average radiated power by the bow-tie shown does not take into account the quasi-optical efficiency η_{qo} in order to be comparable to the ones of the dipoles. In particular, the power radiated is calculated by multiplying the energy spectral density E_s, computed as in (4.14), with the pulse repetition rate f_p. The simulated impedances of the two dipoles and bow-tie, together with the generator impedance for $\mu = 420$ cm^{2}V^{-1}s^{-1} are shown in Figure 4.34.

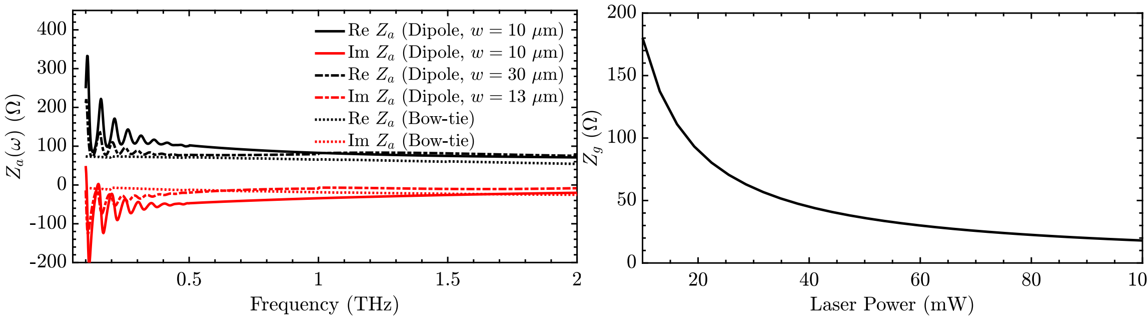

(a) Antennae Impedance **(b)** Generator Impedance

Figure 4.34: Simulated input impedance of the dipoles (shown in Figure 4.32) and bow-tie as function of the frequency, and generator impedance Z_g as function of the laser power level for a mobility $\mu = 420$ cm^{2}V^{-1}s^{-1}.

Although measurements for the dipoles are not available, Figure 4.35 serves as an example of the versatility of the tools presented in this thesis. In particular, it is possible to notice that at low laser power levels the geometry of the structure does not impact on the amount of radiated power since the impedance of the antennas is negligible compared to the one of the generator. By increasing the laser power level, the generator impedance decreases and thus the geometry of the structure becomes crucial to achieve good matching with

Z_g and therefore in the maximization of the power radiated. Since most of the energy is concentrated at low frequencies (see for instance Figure 4.18), it is important to notice that the matching of the antenna impedance with the one of the generator is particularly of interest in that bandwidth.

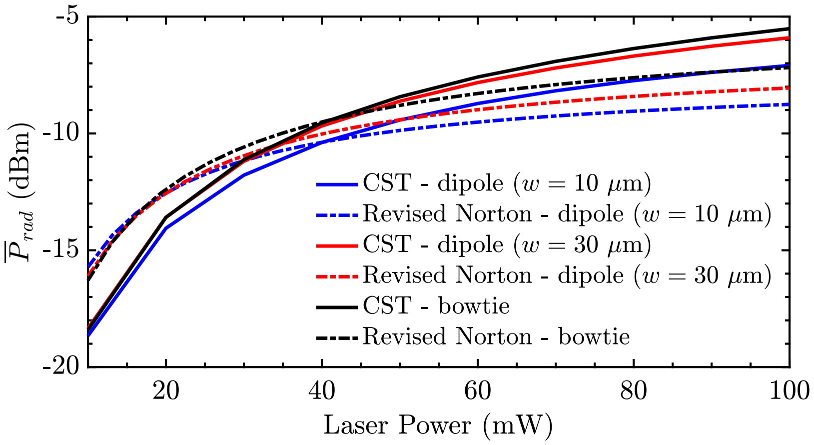

Figure 4.35: Average power radiated as a function of the laser power. The average radiated power computed with the CST method and the revised Norton equivalent circuit method are compared for various structures. Although no measurements are available for the dipoles considered, based on the results verified with the bow-tie (see Figure 4.26) we expect the Revised Norton line (dashed lines) to be slightly more accurate than the CST one (full lines).

Chapter 5

Conclusion

5.1 Summary and conclusions

In this thesis a preparatory work in view of an improved design of connected arrays of pulsed sources is presented.

In chapter 2 a transmission-line approach to approximate the voltage that propagates along an infinite slot printed on an infinite ground plane between two homogeneous dielectric is proposed. In particular, since this thesis has also the goal to serve as a starting ground for the optimization of the power radiated in Photoconductive Antennas (PCA) in a connected array configuration, the voltage is derived in the case where two feeds at an arbitrary small distance are present. Unfortunately, it is demonstrated that the final voltage derived with this approach differs slightly in amplitude and shape from the one recovered with the full spectral integral because of the choice of a leaky-wave structure.

In chapter 3, in order to visualize and characterize the signal generated by the PCA once excited, the time-varying electric field that propagates along an infinite slot and radiated by it is derived. The simplified current derived in [4] and described in section 4.2 is used. This derivation is intended especially for a better understanding of a connected array design in which one has to deal with multiple feeds excited in the same instant which after a brief interval return to the state of very high resistivity. Moreover, a novel way to improve the angle of radiation of leaky-wave antennas is proposed.

In chapter 4 a novel approach based on a commercially available electromagnetic simulator [5] to characterize the biasing of the passive structure, the optical laser excitation and the impulse response of the photoconductor is proposed. The accuracy of the model is verified by calculating the average power radiated by a bow-tie and the results are compared to the measurements in [6]. The model offers an accurate and generalized approach to model any kind of antenna by introducing a simple and effective way to optimize the geometry of an arbitrary passive structure and to maximize the power radiated by it. The characterization of the antenna in frequency domain essentially improves on previously proposed hybrid equivalent circuits [1, 2, 3] since it allows for a wide applicability of the model. Moreover, a revised version of the Norton equivalent circuit [4] is proposed which offers even more accuracy of the CST model and faster computational time. This revised version of the model will offer an invaluable tool to confidently characterize more complex structures such as connected arrays. Although the revised Norton model is very usable to compute the average radiated power being very accurate and computationally non-intensive, it lacks accuracy in describing the transient fields being formulated in frequency domain. This shortcoming can be compensated by using the CST model which, although computationally more intensive and less accurate in the description of the saturation phenomenon, is able to predict more realistically the transient fields. This combination of tools can be advantageous in the quantification of the power radiated and the description of the transient fields of more complex structures such as connected arrays in which the level of complexity is higher since these antennas are inherently characterized by a strong mutual coupling among the various elements.

5.2 Publications

1. *To be submitted*: A journal article will be submitted based on the results obtained in chapter 4 on the IEEE Transactions on Antennas and Propagation.

Appendix A

Impedance of various configurations of Slots and Dipoles

In this appendix the impedance of various configurations of Slots (section A.1) and Dipoles (section A.2) are presented.

A.1 Impedance of Various Configurations of Slots

In this section various configurations of slots are discussed. In particular, the voltage along the slot and the impedance are derived with the assumption of a width w small in terms of the wavelength. The current distribution is given by two magnetic current with equal amplitudes and opposite signs which are perfectly polarized along x. Unless otherwise stated, the reference structure is the one shown in Figure A.1.

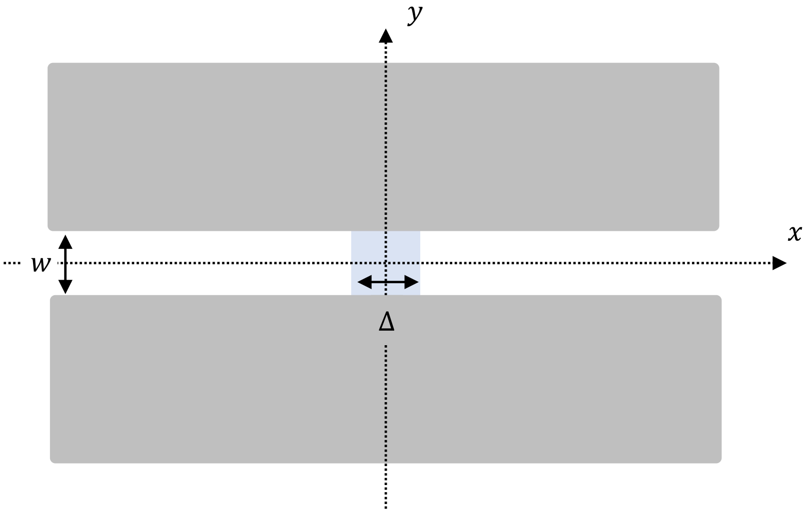

Figure A.1: Slot printed on an infinite ground plane with cross section w with dimensions small in terms of the wavelength and delta gap Δ.

A.1.1 Infinite Slot in Free Space - Singly Fed

Let us consider a slot printed on an infinite ground plane in free space with cross section w and delta gap Δ as shown in Figure A.1. The voltage can be computed as

$$v(x,\omega) = \frac{1}{2\pi}\int_{-\infty}^{\infty} \frac{\operatorname{sinc}\left(\frac{k_x\Delta}{2}\right) I(\omega)}{D(k_x)} e^{-jk_x x} dk_x$$

where $D(k_x)$ is the longitudinal Green's function in free space (for the derivation see [22], [18])

$$D(k_x) = \frac{(k_0^2 - k_x^2)}{k_0\zeta_0} J_0\left(\frac{w}{4}\sqrt{k_0^2 - k_x^2}\right) H_0^{(2)}\left(\frac{w}{4}\sqrt{k_0^2 - k_x^2}\right) \tag{A.1}$$

where J_0 is the zeroth order Bessel function, $H_0^{(2)}$ is the Hankel function of the second kind and zeroth order, k_0 is the free space wavenumber and ζ_0 is the free space characteristic impedance. The input impedance can be calculated as

$$Z_{in}(\omega) = \frac{1}{I(\omega)}\frac{1}{\Delta}\int_{-\Delta/2}^{\Delta/2} v(x,\omega)dx = \frac{1}{2\pi}\int_{-\infty}^{\infty} \frac{\operatorname{sinc}^2\left(\frac{k_x\Delta}{2}\right)}{D(k_x)} dk_x \tag{A.2}$$

The convergence of the integral in (A.2) constitutes a problem when considering $\Delta \ll \lambda$. Thus, one can write the impedance as [23]

$$Z_{in} = Z_{qs} + Z_{dyn} \tag{A.3}$$

where

$$Z_{qs} = \frac{1}{2\pi}\int_{-\infty}^{\infty} \frac{1}{D_1(k_x)} \operatorname{sinc}^2\left(\frac{k_x\Delta}{2}\right) dk_x \tag{A.4}$$

$$Z_{dyn} = \frac{1}{2\pi}\int_{-\infty}^{\infty} \left(\frac{1}{D(k_x)} - \frac{1}{D_1(k_x)}\right) \operatorname{sinc}^2\left(\frac{k_x\Delta}{2}\right) dk_x \tag{A.5}$$

where $D_1(k_x)$ is the longitudinal Green's function for large spectral components k_x

$$D_1(k_x) = \lim_{k_x\to\infty} D(k_x) = \frac{4}{k_0\zeta_0\pi w}\sqrt{k_0^2 - k_x^2}\left[1 + je^{-jw/2\sqrt{k_0^2 - k_x^2}}\right] \tag{A.6}$$

An example of the impedance is shown in Figure A.2.

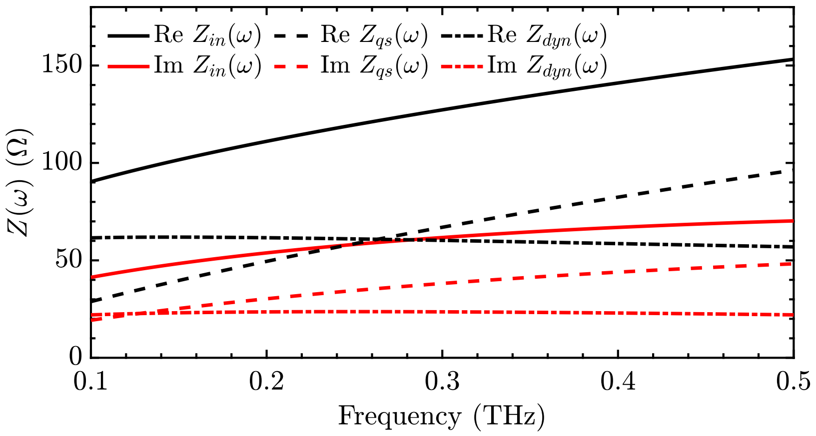

Figure A.2: Input impedance as function of the frequency of an infinite slot in free space. The parameters considered are a width $w = \lambda_0/10$ and a delta gap $\Delta = \lambda_0/10$ where λ_0 is the free space wavelength at the higher frequency.

A.1.2 Infinite Slot between two Infinite dielectrics - Singly Fed

Let us consider a slot printed on an infinite ground plane between two homogeneous half-spaces with permittivities ε_{r2} and ε_{r1}, where $\varepsilon_{r2} > \varepsilon_{r1}$, with cross section w and delta gap Δ as shown in Figure A.1. The slot is fed centrally by an electric dipole. The voltage can be computed as

$$v(x,\omega) = \frac{1}{2\pi}\int_{-\infty}^{\infty} \frac{\operatorname{sinc}\left(\frac{k_x\Delta}{2}\right) I(\omega)}{D(k_x)} e^{-jk_x x} dk_x$$

where $D(k_x)$ is the longitudinal Green's function between two infinite dielectrics (derivation in [22], [18])

$$D(k_x) = \frac{1}{2k_0\zeta_0}\sum_{i=1}^{2}(k_i^2 - k_x^2) J_0\left(\frac{w}{4}\sqrt{k_i^2 - k_x^2}\right) H_0^{(2)}\left(\frac{w}{4}\sqrt{k_i^2 - k_x^2}\right)$$

where J_0 is the zero*th* order Bessel function, $H_0^{(2)}$ is the Hankel function of the second kind and zero*th* order, k_0 is the free space wavenumber and ζ_0 is the free space characteristic impedance. The input impedance can be calculated as

$$Z_{in}(\omega) = \frac{1}{I(\omega)}\frac{1}{\Delta}\int_{-\Delta/2}^{\Delta/2} v(x,\omega)dx = \frac{1}{2\pi}\int_{-\infty}^{\infty} \frac{\operatorname{sinc}^2\left(\frac{k_x\Delta}{2}\right)}{D(k_x)} dk_x \qquad \text{(A.7)}$$

The convergence of (A.7) constitutes a problem when considering $\Delta \ll \lambda$. Thus, one can write the impedance as [23]

$$Z_{in} = Z_{qs} + Z_{dyn} \qquad \text{(A.8)}$$

where

$$Z_{qs} = \frac{1}{2\pi}\int_{-\infty}^{\infty} \frac{1}{D_1(k_x)} \operatorname{sinc}^2\left(\frac{k_x\Delta}{2}\right) dk_x \qquad \text{(A.9)}$$

$$Z_{dyn} = \frac{1}{2\pi}\int_{-\infty}^{\infty} \left(\frac{1}{D(k_x)} - \frac{1}{D_1(k_x)}\right) \operatorname{sinc}^2\left(\frac{k_x\Delta}{2}\right) dk_x \qquad \text{(A.10)}$$

where $D_1(k_x)$ is the longitudinal Green's function for large k_x

$$\frac{1}{D_1(k_x)} = \lim_{k_x\to\infty}\frac{1}{D(k_x)} = \frac{k_0\zeta_0\pi w}{2}\frac{1}{(k_1^2-k_2^2)}\left(\sqrt{k_1^2-k_x^2}-\sqrt{k_2^2-k_x^2}\right) \tag{A.11}$$

An example of the impedance is shown in Figure A.3.

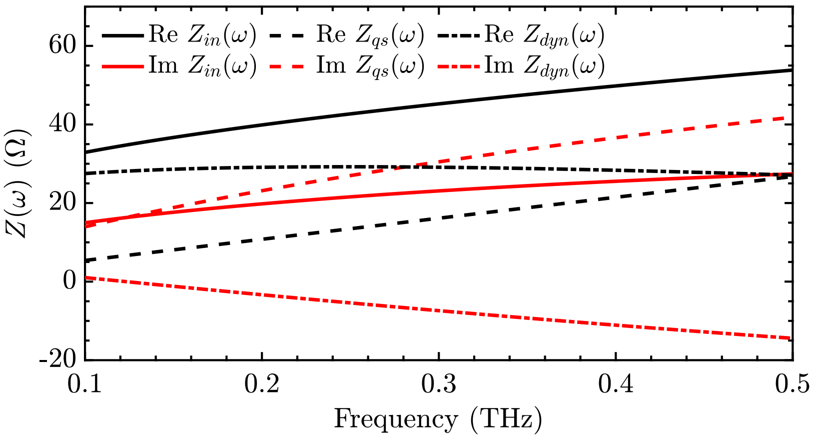

Figure A.3: Input impedance as function of the frequency of an infinite slot printed between air ($\varepsilon_r = 1$) and silicon ($\varepsilon_r = 11.9$). The parameters considered are a width $w = \lambda_d/10$ and a delta gap $\Delta = \lambda_d/10$ where λ_d is the wavelength in the denser medium at the higher frequency.

A.1.3 Infinite Slot between two Infinite dielectrics - Fed by a Dipole

Let us consider a slot printed on an infinite ground plane between two homogeneous half-spaces with permittivities ε_{r2} and ε_{r1}, where $\varepsilon_{r2} > \varepsilon_{r1}$, with cross section w and delta gap Δ as shown in Figure A.1. The slot is fed centrally by an electric dipole. The voltage can be computed as

$$v(x,\omega) = \frac{1}{2\pi}\int_{-\infty}^{\infty}\frac{\operatorname{sinc}\left(\frac{k_x\Delta}{2}\right)I(\omega)}{D(k_x)}e^{-jk_xx}dk_x$$

where $D(k_x)$ is the longitudinal Green's function between two infinite dielectrics (derivation in [22], [18])

$$D(k_x) = \frac{1}{2k_0\zeta_0}\sum_{i=1}^{2}(k_i^2-k_x^2)J_0\left(\frac{w}{4}\sqrt{k_i^2-k_x^2}\right)H_0^{(2)}\left(\frac{w}{4}\sqrt{k_i^2-k_x^2}\right) \tag{A.12}$$

where J_0 is the zero*th* order Bessel function, $H_0^{(2)}$ is the Hankel function of the second kind and zero*th* order, k_0 is the free space wavenumber and ζ_0 is the free space characteristic impedance. The input impedance can be calculated as

$$Z_{in}^{slot}(w,\Delta,w) = \frac{1}{I(\omega)}\frac{1}{\Delta}\int_{-\Delta/2}^{\Delta/2}v(x,\omega)dx = \frac{1}{2\pi}\int_{-\infty}^{\infty}\frac{\operatorname{sinc}^2\left(\frac{k_x\Delta}{2}\right)}{D(k_x,w)}dk_x \tag{A.13}$$

The convergence of (A.13) constitutes a problem when considering $\Delta \ll \lambda$. Thus, one can write the impedance as [23]

$$Z_{in}^{slot}(w,\Delta,w) = Z_{qs}^{slot}(w,\Delta,w) + Z_{dyn}^{slot}(w,\Delta,w) \tag{A.14}$$

The integral in (A.13) yields an impedance with a reactive part which is exclusively inductive. A more realistic modeling of a slot includes a capacitive contribution of the gap. Since this thesis is concerned with the modeling of PCAs, this analytical approach of describing the impedance of structures with known Green's functions such as dipoles and slots facilitates the understanding of the radiation mechanism. In order to introduce this capacitive contribution, one can essentially add the quasi-static admittance of a small dipole which acts as a connector between the slot and the feeding gap.
The following procedure describes more rigorously what stated above. The admittance of the slot can be computed as $Y_{in}^{slot}(w,\Delta,w) = Z_{in}^{slot}(w,\Delta,w)^{-1}$; separating the dynamic quasi-static contributions as in (A.14) ones gets

$$Y_{in}^{slot}(w,\Delta,w) = Y_{qs}^{slot}(w,\Delta,w) + Y_{dyn}^{slot}(w,\Delta,w) \tag{A.15}$$

The modeling of the structure is shown in Figure A.4. The two infinite dipoles have the same width Δ, but different gap dimensions (t and w). Accordingly, the admittances can be written as

$$Y_{in}^{dip}(\Delta,w) = Y_{qs}^{dip}(\Delta,w) + Y_{dyn}^{dip}(\Delta,w) \tag{A.16}$$

$$Y_{in}^{dip}(\Delta,t) = Y_{qs}^{dip}(\Delta,t) + Y_{dyn}^{dip}(\Delta,t) \tag{A.17}$$

The quasi-static admittances in (A.16) and (A.17) can be computed as in [24]

$$\begin{aligned} Y_{qs}^{dip}(\Delta,w) &= \sum_{n=1}^{2} Y_n(w) \\ Y_{qs}^{dip}(\Delta,t) &= \sum_{n=1}^{2} Y_n(t) \\ Y_n(\xi) &= -\frac{j\Delta k_0 \varepsilon_{r,n}}{\pi\zeta_0}\left[\ln\left(e^{\gamma}\frac{k_n}{2}\xi\right) - \frac{3}{2}\right] \end{aligned}$$

where $\gamma = 0.5772156649\ldots$ is the Euler constant.

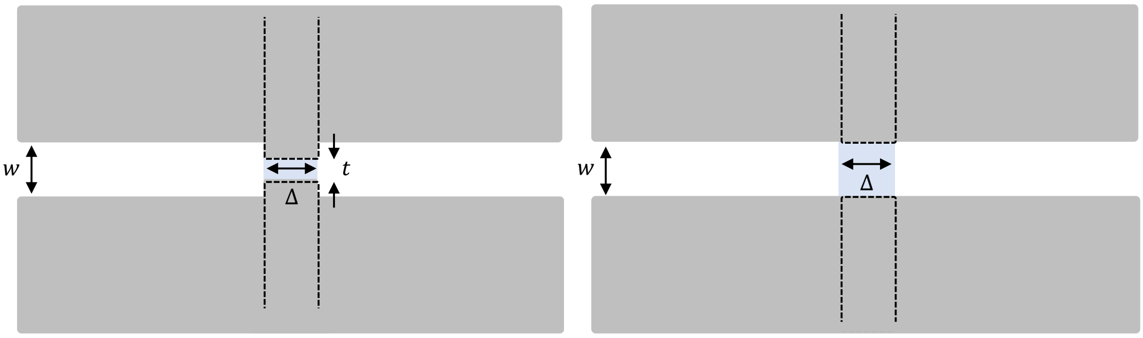

(a) (t,Δ) **(b)** (w,Δ)

Figure A.4: Infinite slot of width w, and gap dimensions (t,Δ) and (w,Δ) in Figure A.4a and in Figure A.4b, respectively.

Since the dynamic part of the admittance does not depend from the gap dimensions, one can safely assume that

$$Y_{dyn}^{dip}(\Delta,w) \approx Y_{dyn}^{dip}(\Delta,t) \tag{A.18}$$

And therefore substituting (A.18) in (A.17) one obtains that

$$Y_{in}^{dip}(\Delta, t) = Y_{qs}^{dip}(\Delta, t) + Y_{dyn}^{dip}(\Delta, w)$$

Since the quasi-static part of the admittance mostly depends on the geometry of the gap, one can notice that

$$Y_{qs}^{slot}(w, \Delta, w) \approx Y_{qs}^{dip}(\Delta, w) \tag{A.19}$$

And therefore substituting (A.19) in (A.15) one obtains that

$$Y_{in}^{slot}(w, \Delta, w) = Y_{qs}^{dip}(\Delta, w) + Y_{dyn}^{slot}(w, \Delta, w) \tag{A.20}$$

By extracting the dynamic part of the admittance from (A.20) and repeating the steps described above for $Y_{in}^{slot}(w, \Delta, t)$, one can find that

$$\begin{aligned} Y_{in}^{slot}(w, \Delta, t) &= Y_{qs}^{dip}(\Delta, t) + Y_{dyn}^{slot}(w, \Delta, t) \\ &= Y_{qs}^{dip}(\Delta, t) + \left[Y_{in}^{slot}(w, \Delta, w) - Y_{qs}^{dip}(\Delta, w) \right] \end{aligned}$$

More clearly:

$$Y_{in}^{slot}(w, \Delta, t) = Y_{in}^{slot}(w, \Delta, w) + \left[Y_{qs}^{dip}(\Delta, t) - Y_{qs}^{dip}(\Delta, w) \right] \tag{A.21}$$

The final slot impedance can be recovered simply as $Z_{in}^{slot}(w, \Delta, t) = Y_{in}^{slot}(w, \Delta, t)^{-1}$.

An example of the impedance is shown in Figure A.5.

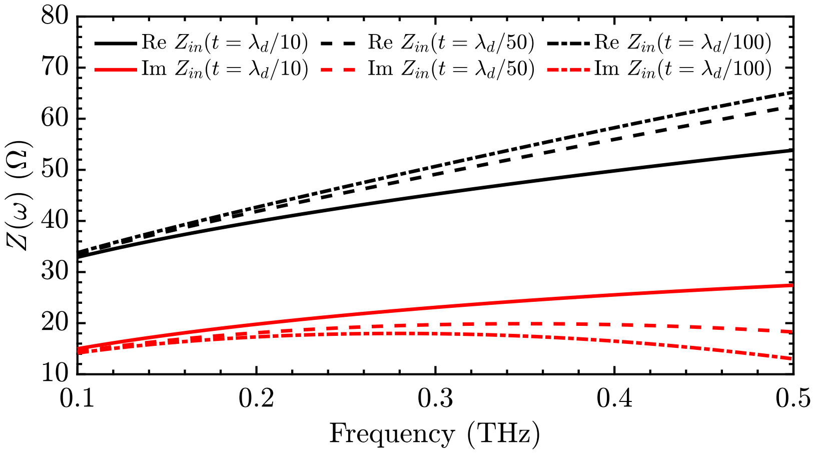

Figure A.5: Input impedance as function of the frequency of an infinite slot printed between air ($\varepsilon_r = 1$) and silicon ($\varepsilon_r = 11.9$) fed by a small dipole. The parameters considered are a width $w = \lambda_d/10$ and a delta gap $\Delta = \lambda_d/10$ where λ_d is the wavelength in the denser medium at the higher frequency.

A.1.4 Infinite Slot between two Infinite dielectrics - Infinitely Fed

Let us consider a slot printed on an infinite ground plane between two homogeneous half-spaces with permittivities ε_{r2} and ε_{r1}, where $\varepsilon_{r2} > \varepsilon_{r1}$, with cross section w and delta gap Δ as shown in Figure A.1. The slot is periodically fed at a distance d_x by an electric dipole.

The voltage can be computed as

$$v(x,\omega) = \frac{1}{2\pi}\int_{-\infty}^{\infty} \frac{I_e(k_x)}{D(k_x)} e^{-jk_x x} dk_x \tag{A.22}$$

where $D(k_x)$ is the longitudinal Green's function between two infinite dielectrics (derivation in [22], [18])

$$D(k_x) = \frac{1}{2k_0\zeta_0}\sum_{i=1}^{2}(k_i^2 - k_x^2) J_0\left(\frac{w}{4}\sqrt{k_i^2 - k_x^2}\right) H_0^{(2)}\left(\frac{w}{4}\sqrt{k_i^2 - k_x^2}\right) \tag{A.23}$$

where J_0 is the zero*th* order Bessel function, $H_0^{(2)}$ is the Hankel function of the second kind and zero*th* order, k_0 is the free space wavenumber and ζ_0 is the free space characteristic impedance. Assuming every source to be uniformly distributed along a gap of length Δ, constant in amplitude and linearly progressive in phase, the spectral transform of the excitation can be expressed as

$$\begin{aligned} I_e(k_x) &= I(\omega)\,\mathrm{sinc}\left(\frac{k_x\Delta}{2}\right) \sum_{n_x=-N/2}^{N/2} i(n_x) e^{jk_x n_x d_x} \\ &= I(\omega)\,\mathrm{sinc}\left(\frac{k_x\Delta}{2}\right) \sum_{n_x=-N/2}^{N/2} e^{j(k_x - k_{x0})n_x d_x} \end{aligned} \tag{A.24}$$

Applying the Poisson infinite formula, (A.24) becomes

$$I_e(k_x) = I(\omega)\frac{2\pi}{d_x}\sum_{m_x=-\infty}^{\infty} \delta(k_x - k_{xm})$$

where $k_{xm} = k_{x0} - 2\pi m_x/d_x$. The voltage in (A.22) can now be written as

$$v_0(x,\omega) = \frac{I(\omega)}{d_x}\sum_{m_x=-\infty}^{\infty} \frac{\mathrm{sinc}\left(\frac{k_{xm}\Delta}{2}\right)}{D(k_{xm})} e^{-jk_{xm}x}$$

The input impedance can be calculated as

$$Z_{in}(\omega) = \frac{1}{d_x}\sum_{m_x=-\infty}^{\infty} \frac{\mathrm{sinc}^2\left(\frac{k_{xm}\Delta}{2}\right)}{D(k_{xm})}$$

An example of the impedance is shown in Figure A.6.

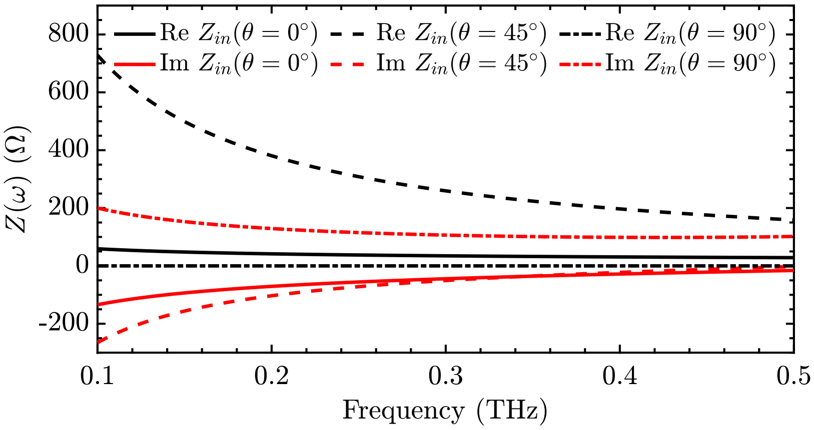

Figure A.6: Input impedance as function of the frequency of an infinite slot printed between air ($\varepsilon_r = 1$) and silicon ($\varepsilon_r = 11.9$) fed by an infinite number of feeds periodically positioned at a distance of $d_x = 0.42\lambda_d$. The parameters considered are a width $w = \lambda_d/10$ and a delta gap $\Delta = \lambda_d/10$ where λ_d is the wavelength in the denser medium at the higher frequency.

A.1.5 Infinite Array of Slots between two Infinite dielectrics - Singly Fed

Let us consider an array of slots printed on an infinite ground plane between two homogeneous half-spaces with permittivities ε_{r2} and ε_{r1}, where $\varepsilon_{r2} > \varepsilon_{r1}$, with cross section w and delta gap Δ as shown in Figure A.7. The slots are fed centrally by an electric dipole.

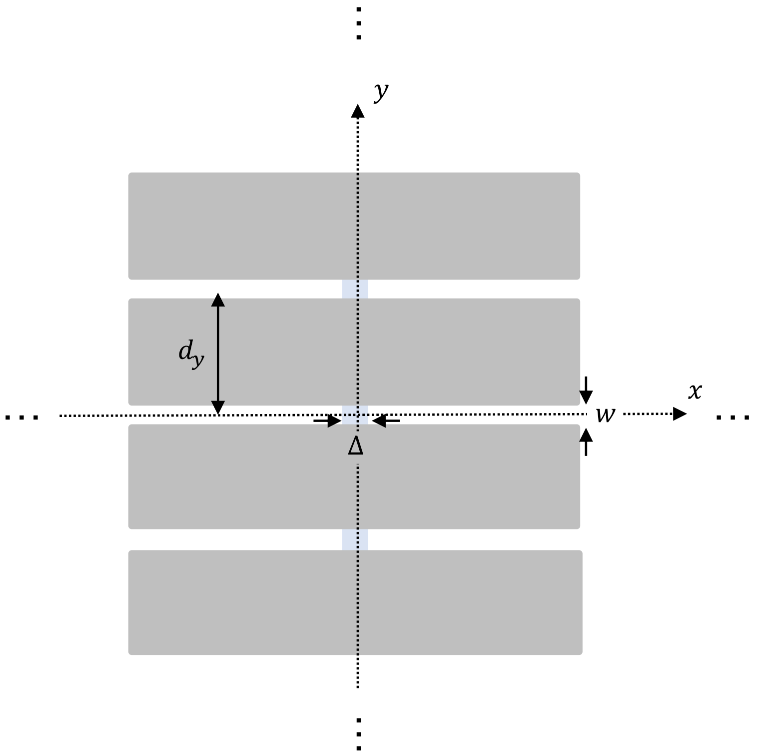

Figure A.7: Infinite array of slots printed on an infinite ground plane between two homogeneous half-spaces with permittivities ε_{r2} and ε_{r1}, where $\varepsilon_{r2} > \varepsilon_{r1}$, with cross section w and delta gap Δ.

The voltage can be computed as

$$v_\infty(x,\omega) = \frac{1}{2\pi}\int_{-\infty}^{\infty} \frac{\operatorname{sinc}\left(\frac{k_x\Delta}{2}\right) I(\omega)}{D_\infty(k_x)} e^{-jk_x x} dk_x$$

where $D_\infty(k_x)$ is the infinite longitudinal Green's function between two infinite dielectrics (derivation in [22])

$$D_\infty(k_x) = \frac{1}{d_y}\sum_{m_y=-\infty}^{\infty} \frac{J_0\left(\frac{wk_{ym}}{2}\right)}{k_0\zeta_0}\sum_{i=1}^{2}\frac{k_i^2-k_x^2}{\sqrt{k_i^2-k_x^2-k_{ym}^2}} \tag{A.25}$$

where J_0 is the zero*th* order Bessel function and ζ_0 is the free space characteristic impedance. The input impedance can be calculated as

$$Z_{in,\infty}(\omega) = \frac{1}{I(\omega)}\frac{1}{\Delta}\int_{-\Delta/2}^{\Delta/2} v_\infty(x,\omega)dx = \frac{1}{2\pi}\int_{-\infty}^{\infty}\frac{\operatorname{sinc}^2\left(\frac{k_x\Delta}{2}\right)}{D_\infty(k_x)}dk_x$$

An example of the impedance is shown in Figure A.8.

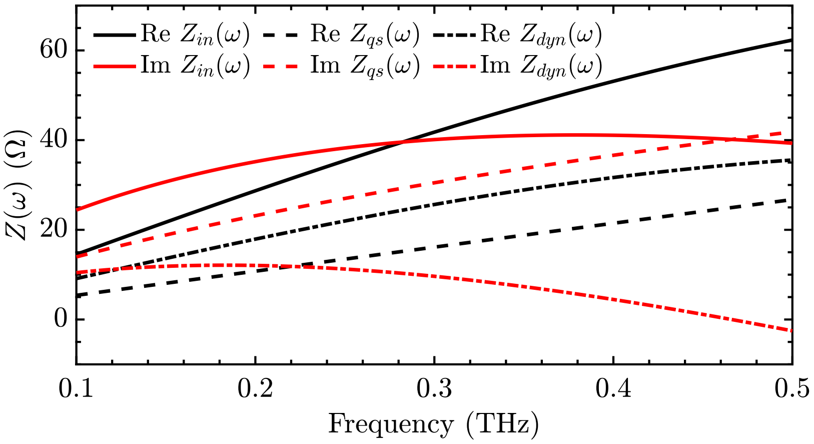

Figure A.8: Input impedance as function of the frequency of an infinite array of slots with periodicity $d_y = 0.42\lambda_d$, printed between air ($\varepsilon_r = 1$) and silicon ($\varepsilon_r = 11.9$) and fed singly in its origin. The parameters considered are a width $w = \lambda_d/10$ and a delta gap $\Delta = \lambda_d/10$ where λ_d is the wavelength in the denser medium at the higher frequency.

A.1.6 Infinite Array of Slots between two Infinite dielectrics - Infinitely Fed

Let us consider an array of slots printed on an infinite ground plane between two homogeneous half-spaces with permittivities ε_{r2} and ε_{r1}, where $\varepsilon_{r2} > \varepsilon_{r1}$, with cross section w and delta gap Δ as shown in Figure A.9. The slots are fed periodically at a distance d_x by an electric dipole.

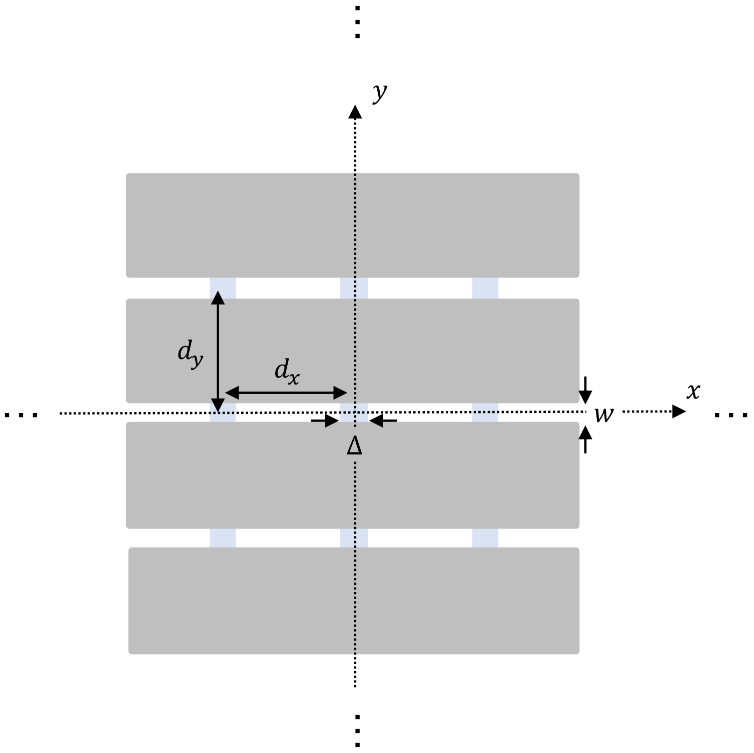

Figure A.9: Infinite array of slots fed by N feeds printed on an infinite ground plane between two homogeneous half-spaces with permittivities ε_{r2} and ε_{r1}, where $\varepsilon_{r2} > \varepsilon_{r1}$, with cross section w and delta gap Δ.

The voltage can be computed as

$$v_\infty(x,\omega) = \frac{1}{2\pi}\int_{-\infty}^{\infty} \frac{I_e(k_x)}{D_\infty(k_x)} e^{-jk_x x} dk_x \tag{A.26}$$

where $D_\infty(k_x)$ is the infinite longitudinal Green's function between two infinite dielectrics (derivation in [22])

$$D_\infty(k_x) = \frac{1}{d_y}\sum_{m_y=-\infty}^{\infty} \frac{J_0\left(\frac{wk_{ym}}{2}\right)}{k_0\zeta_0}\sum_{i=1}^{2}\frac{k_i^2 - k_x^2}{\sqrt{k_i^2 - k_x^2 - k_{ym}^2}} \tag{A.27}$$

where J_0 is the zeroth order Bessel function and ζ_0 is the free space characteristic impedance. Assuming every source to be uniformly distributed along a gap of length Δ, constant in amplitude and linearly progressive in phase, the spectral transform of the excitation can be expressed as

$$I_e(k_x) = I(\omega)\,\mathrm{sinc}\left(\frac{k_x\Delta}{2}\right)\sum_{n_x=-N/2}^{N/2} i(n_x)e^{jk_x n_x d_x} = I(\omega)\,\mathrm{sinc}\left(\frac{k_x\Delta}{2}\right)\sum_{n_x=-N/2}^{N/2} e^{j(k_x - k_{x0})n_x d_x} \tag{A.28}$$

Applying the Poisson infinite formula, (A.28) becomes

$$I_e(k_x) = I(\omega)\frac{2\pi}{d_x}\sum_{m_x=-\infty}^{\infty}\delta(k_x - k_{xm})$$

where $k_{xm} = k_{x0} - 2\pi m_x/d_x$. The voltage in (A.26) can now be written as

$$v_\infty(x,\omega) = \frac{I(\omega)}{d_x} \sum_{m_x=-\infty}^{\infty} \frac{\text{sinc}\left(\frac{k_{xm}\Delta}{2}\right)}{D_\infty(k_{xm})} e^{-jk_{xm}x}$$

The input impedance can be calculated as

$$Z_{in,\infty}(\omega) = \frac{1}{d_x} \sum_{m_x=-\infty}^{\infty} \frac{\text{sinc}^2\left(\frac{k_{xm}\Delta}{2}\right)}{D_\infty(k_{xm})}$$

An example of the impedance is shown in Figure A.10.

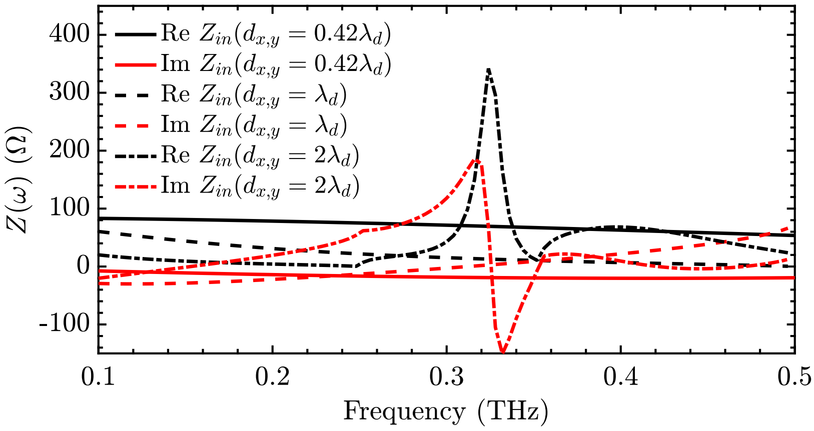

Figure A.10: Input impedance as function of the frequency of an infinite array of slots with periodicity d_y, printed between air ($\varepsilon_r = 1$) and silicon ($\varepsilon_r = 11.9$) and periodically fed with a distance d_x. The parameters considered are a width $w = \lambda_d/10$ and a delta gap $\Delta = \lambda_d/10$ where λ_d is the wavelength in the denser medium at the higher frequency.

A.2 Impedance of Various Configurations of Dipoles

In this section various configurations of dipoles are discussed. In particular, the current along the dipole and the admittance are derived with the assumption of a width w small in terms of the wavelength. The current distribution is given by two magnetic current with equal amplitudes and opposite signs which are perfectly polarized along x.

A.2.1 Infinite Dipole in Free Space - Singly fed

Let us consider a dipole in free space with cross section w and delta gap Δ as shown in Figure A.11.

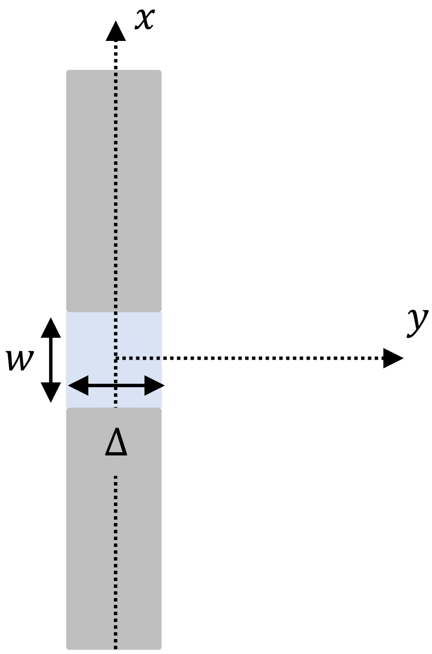

Figure A.11: Infinite dipole in free space with cross section w with dimensions small in terms of the wavelength and delta gap Δ.

The current can be computed as

$$i(x,\omega) = -\frac{1}{2\pi}\int_{-\infty}^{\infty} \frac{\operatorname{sinc}\left(\frac{k_x\Delta}{2}\right)V(\omega)}{D(k_x)} e^{-jk_x x} dk_x$$

where $D(k_x)$ is the longitudinal Green's function in free space (for the derivation see [22], [18])

$$D(k_x) = -\frac{\zeta_0}{4k_0}(k_0^2 - k_x^2) J_0\left(\frac{w}{4}\sqrt{k_0^2 - k_x^2}\right) H_0^{(2)}\left(\frac{w}{4}\sqrt{k_0^2 - k_x^2}\right) \tag{A.29}$$

where J_0 is the zero*th* order Bessel function, $H_0^{(2)}$ is the Hankel function of the second kind and zero*th* order, k_0 is the free space wavenumber and ζ_0 is the free space characteristic impedance. The input admittance can be calculated as

$$Y_{in}(\omega) = \frac{1}{V(\omega)}\frac{1}{\Delta}\int_{-\Delta/2}^{\Delta/2} i(x,\omega)dx = -\frac{1}{2\pi}\int_{-\infty}^{\infty} \frac{\operatorname{sinc}^2\left(\frac{k_x\Delta}{2}\right)}{D(k_x)} dk_x \tag{A.30}$$

The convergence of the integral in (A.30) constitutes a problem when considering $\Delta \ll \lambda$. Thus, one can write the admittance as [23]

$$Y_{in} = Y_{qs} + Y_{dyn} \tag{A.31}$$

where

$$Y_{qs} = -\frac{1}{2\pi}\int_{-\infty}^{\infty} \frac{1}{D_1(k_x)} \operatorname{sinc}^2\left(\frac{k_x\Delta}{2}\right) dk_x \tag{A.32}$$

$$Y_{dyn} = -\frac{1}{2\pi}\int_{-\infty}^{\infty} \left(\frac{1}{D(k_x)} - \frac{1}{D_1(k_x)}\right) \operatorname{sinc}^2\left(\frac{k_x\Delta}{2}\right) dk_x \tag{A.33}$$

where $D_1(k_x)$ is the longitudinal Green's function for large spectral components k_x

$$D_1(k_x) = \lim_{k_x \to \infty} D(k_x) = \frac{\zeta_0}{k_0 \pi w}\sqrt{k_0^2 - k_x^2}\left[1 + e^{-j/2\left(w\sqrt{k_0^2-k_x^2}-\pi\right)}\right] \tag{A.34}$$

An example of the impedance is shown in Figure A.12.

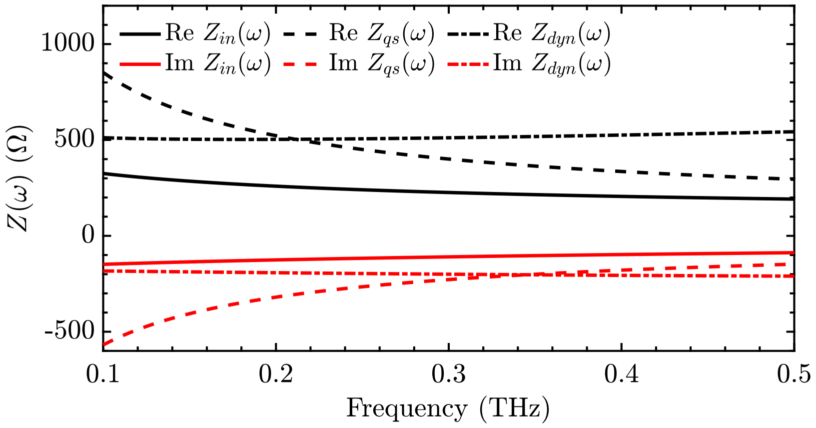

Figure A.12: Input impedance as function of the frequency of an infinite dipole in free space. The parameters considered are a cross section $w = \lambda_0/10$ and a delta gap $\Delta = \lambda_0/10$ where λ_0 is the free space wavelength at the higher frequency.

A.2.2 Infinite Dipole in Free Space with Surface Resistance - Singly fed

Let us consider a dipole in free space with cross section w and delta gap Δ as shown in Figure A.11. The current can be computed as in [13]

$$i(x,\omega) = -\frac{1}{2\pi}\int_{-\infty}^{\infty} \frac{\operatorname{sinc}\left(\frac{k_x \Delta}{2}\right) V(\omega)}{D(k_x) - \frac{R_d}{w}} e^{-jk_x x} dk_x$$

where R_d is the surface resistance associated with the ohmic losses of the metal. Note that for lossless dipoles (i.e., $R_d = 0$ Ω) the poles k_{xp} coincides with the branch points in $k_x = \pm k_0$, whereas with the assumption of a lossy metal the poles move away from the branch points and therefore it is possible to evaluate them separately. $D(k_x)$ is the longitudinal Green's function in free space (for the derivation see [22])

$$D(k_x) = -\frac{\zeta_0}{4k_0}(k_0^2 - k_x^2) J_0\left(\frac{w}{4}\sqrt{k_0^2 - k_x^2}\right) H_0^{(2)}\left(\frac{w}{4}\sqrt{k_0^2 - k_x^2}\right) \tag{A.35}$$

where J_0 is the zero*th* order Bessel function, $H_0^{(2)}$ is the Hankel function of the second kind and zero*th* order, k_0 is the free space wavenumber and ζ_0 is the free space characteristic impedance. The input admittance can be calculated as

$$Y_{in}(\omega) = \frac{1}{V(\omega)}\frac{1}{\Delta}\int_{-\Delta/2}^{\Delta/2} i(x,\omega)dx = -\frac{1}{2\pi}\int_{-\infty}^{\infty}\frac{\operatorname{sinc}^2\left(\frac{k_x\Delta}{2}\right)}{D(k_x) - \frac{R_d}{w}} dk_x$$

An example of the impedance is shown in Figure A.13.

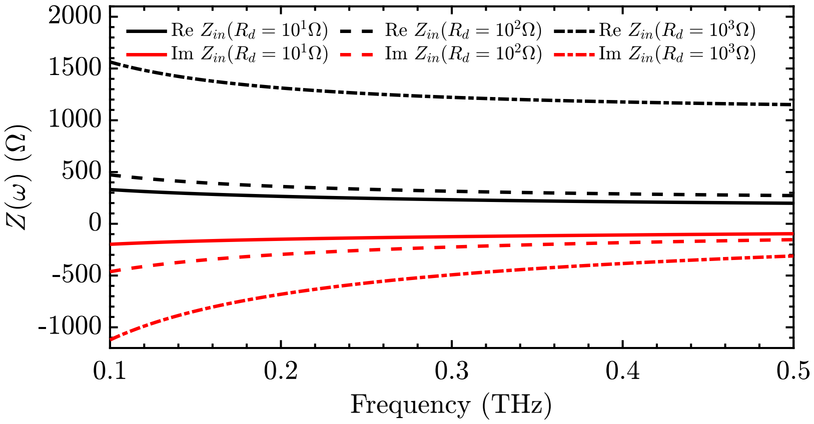

Figure A.13: Input impedance as function of the frequency of an infinite dipole in free space characterized by a metal with a finite resistance R_d. The parameters considered are a cross section $w = \lambda_0/10$ and a delta gap $\Delta = \lambda_0/10$ where λ_0 is the free space wavelength at the higher frequency.

A.2.3 Infinite Dipole between two Infinite Dielectrics - Singly fed

Let us consider an infinite dipole printed between two homogeneous half-spaces with permittivities ε_{r2} and ε_{r1}, where $\varepsilon_{r2} > \varepsilon_{r1}$, with cross section w and delta gap Δ as shown in Figure A.11. For the sake of simplicity, it is assumed that $\varepsilon_{r1} = 1$ and therefore the pedix for medium 1 is substituted always with 0, i.e., the canonical subscript for free-space.

Derivation of the longitudinal Green's function The canonical Green's function for an electric field and an electric current polarized along x can be expressed as

$$G_{xx}^{EJ}(k_x, k_y) = -\frac{v_{TM}(z=0)k_x^2 + v_{TE}(z=0)k_y^2}{k_\rho^2} \tag{A.36}$$

The voltage at $z = 0$ due to an electric source at $z' = 0$ can be expressed in terms of the input impedance and thus considering the TE and TM polarizations separately the voltages and currents become:

$$v_{TM}(z=0) = \frac{Z_0^{TM} Z_2^{TM}}{Z_0^{TM} + Z_2^{TM}} \tag{A.37}$$

$$i_{TM}(z=0) = 0 \tag{A.38}$$

$$v_{TE}(z=0) = \frac{Z_0^{TE} Z_2^{TE}}{Z_0^{TE} + Z_2^{TE}} \tag{A.39}$$

$$i_{TE}(z=0) = 0 \tag{A.40}$$

where

$$k_{zi} = \sqrt{k_i^2 - k_x^2 - k_y^2} \tag{A.41}$$

$$Z_i^{TM}(z=0) = \frac{\zeta_i k_{zi}}{k_i} \tag{A.42}$$

$$Z_i^{TE}(z=0) = \frac{\zeta_i k_i}{k_{zi}} \tag{A.43}$$

Substituting (A.41)-(A.43) in (A.37) and (A.39) one obtains

$$v_{TM}(z=0) = \frac{\frac{\zeta_0 k_{z0}}{k_0}\frac{\zeta_1 k_{z2}}{k_2}}{\frac{\zeta_0 k_{z0}}{k_0} + \frac{\zeta_1 k_{z2}}{k_2}} = \frac{\zeta_0}{k_0}\frac{k_{z0}k_{z2}}{\varepsilon k_{z0} + k_{z2}}$$

$$v_{TE}(z=0) = \frac{\frac{\zeta_0 k_0}{k_{z0}}\frac{\zeta_1 k_2}{k_{z2}}}{\frac{\zeta_0 k_0}{k_{z0}} + \frac{\zeta_1 k_2}{k_{z2}}} = \frac{\zeta_0 k_0}{k_{z2} + k_{z0}}$$

Therefore the Green's function in (A.36) becomes

$$\begin{aligned} G_{xx}^{EJ}(k_x, k_y) &= -\frac{\frac{\zeta_0}{k_0}\frac{k_{z0}k_{z2}}{\varepsilon k_{z0}+k_{z2}}k_x^2 + \frac{\zeta_0 k_0}{k_{z2}+k_{z0}}k_y^2}{k_x^2 + k_y^2} \\ &= -\zeta_0 k_0 \frac{1}{k_x^2 + k_y^2}\left[\frac{1}{k_0^2}\frac{k_{z0}k_{z2}}{\varepsilon_{r,2}k_{z0} + k_{z2}}k_x^2 + \frac{1}{k_{z2} + k_{z0}}k_y^2\right] \end{aligned}$$

The longitudinal Green's function $D(k_x)$ becomes (assuming a uniform distribution of the current instead of an edge singular behavior $J_0\left(k_y w/2\right)$ as in [25])

$$\begin{aligned} D(k_x, w) &= \frac{1}{2\pi}\int_{-\infty}^{\infty} G_{xx}(k_x, k_y)\,\mathrm{sinc}^2\left(\frac{k_y w}{2}\right) dk_y \\ &= -\frac{\zeta_0 k_0}{2\pi}\int_{-\infty}^{\infty} \frac{1}{k_x^2 + k_y^2}\left[\frac{1}{k_0^2}\frac{k_{z0}k_{z2}}{\varepsilon_{r,2}k_{z0} + k_{z2}}k_x^2 + \frac{1}{k_{z2} + k_{z0}}k_y^2\right]\mathrm{sinc}^2\left(\frac{k_y w}{2}\right) dk_y \end{aligned} \tag{A.44}$$

The integration path of (A.44) is given by

$$\int [\ldots]dk_y = \int_{-\infty,\text{ on TRS}}^{\infty,\text{ on TRS}} [\ldots]dk_y + \int_{-\infty, k_2 \text{ on TRS}}^{\infty,-k_2 \text{ on TRS}} [\ldots]dk_y + \int_{-\infty,-k_2 \text{ on BRS}}^{\infty, k_2 \text{ on BRS}} [\ldots]dk_y$$

where TRS and BRS are the Top Riemann sheet and the Bottom Riemann sheet, respectively. Since the integral cannot be solved analytically, we can help the convergence rate by extracting the high spectral components from $D(k_x)$ ([25]) as

$$\begin{aligned} D_\infty(k_x) = \lim_{k_x\to\infty} D(k_x) = \frac{1}{w}G_{xx}(k_x, k_y = 0) &= -\frac{\zeta_0 k_0}{w}\frac{1}{k_x^2}\left[\frac{1}{k_0^2}\frac{\sqrt{k_0^2 - k_x^2}\sqrt{k_2^2 - k_x^2}}{\varepsilon_{r,2}\sqrt{k_0^2 - k_x^2} + \sqrt{k_2^2 - k_x^2}}k_x^2\right] \\ &= -\frac{\zeta_0}{wk_0}\left[\frac{\sqrt{k_0^2 - k_x^2}\sqrt{k_2^2 - k_x^2}}{\varepsilon_{r,2}\sqrt{k_0^2 - k_x^2} + \sqrt{k_2^2 - k_x^2}}\right] \end{aligned}$$

Derivation of the Admittance The admittance can be therefore separated in two contributions, a dynamic one an an infinite one (with reference to the infinitely big spectral components), as

$$Y(\omega) = Y_{dyn}(\omega) + Y_\infty(\omega) \tag{A.45}$$

where

$$Y_{dyn}(\omega) = \frac{1}{2\pi}\int_{-\infty}^{\infty}\left(-\frac{1}{D(k_x)} + \frac{1}{D_\infty(k_x)}\right)\mathrm{sinc}^2\left(\frac{k_x\Delta}{2}\right) dk_x$$

$$Y_\infty(\omega) = -\frac{1}{2\pi}\int_{-\infty}^{\infty}\frac{1}{D_\infty(k_x)}\,\mathrm{sinc}^2\left(\frac{k_x\Delta}{2}\right) dk_x$$

One can decompose Y_∞ in two separate components $Y_\infty = Y_\infty^0 + Y_\infty^2$ where

$$\begin{aligned} Y_\infty^i(\omega) &= \frac{k_0 w}{\zeta_0}\frac{1}{2\pi}\int_{-\infty}^{\infty}\text{sinc}^2\left(\frac{k_x\Delta}{2}\right)\frac{\varepsilon_{r,i}\sqrt{k_i^2-k_x^2}}{\sqrt{k_0^2-k_x^2}\sqrt{k_2^2-k_x^2}}dk_x \\ &= \frac{k_0 w\varepsilon_{r,i}}{\zeta_0}\frac{1}{2\pi}\int_{-\infty}^{\infty}\text{sinc}^2\left(\frac{k_x\Delta}{2}\right)\frac{1}{\sqrt{k_i^2-k_x^2}}dk_x \end{aligned} \tag{A.46}$$

It is possible to solve (A.46) analytically when the argument of the sinc function is small compared to the wavelength, i.e., $\delta \ll \lambda_d \Rightarrow \text{sinc}^2(k_x\Delta/2) \approx 1$. By doing so and recalling the Fourier-transform of the Hankel function

$$H_0^{(2)}(k_i|x|) = \frac{1}{\pi}\int_{-\infty}^{\infty}\frac{1}{\sqrt{k_i^2-k_x^2}}e^{-jk_x x}dk_x \tag{A.47}$$

one can write (A.46) as

$$Y_\infty^i(\omega) = \frac{k_0 w\varepsilon_{r,i}}{\zeta_0}\frac{1}{2\pi}\int_{-\infty}^{\infty}\frac{1}{\sqrt{k_i^2-k_x^2}}dk_x = \frac{k_0 w\varepsilon_{r,i}}{2\zeta_0}H_0^{(2)}(0)$$

Invoking the small argument approximation of the Hankel function, one finally obtains that

$$Y_\infty^i(\omega) = \frac{k_0 w\varepsilon_{r,i}}{2\zeta_0}\left[\frac{1}{2} - \frac{j}{\pi}\ln\left(\frac{e^\gamma k_i}{2}\right) - \frac{j}{\pi}\left(\ln\delta - \frac{3}{2}\right)\right]$$

where $\gamma = 0.5772156649\ldots$ is the Euler constant. Note that this solution holds only for low frequencies, whereas for higher frequencies the numerical integration is required, although the convergence is much faster.

An example of the impedance is shown in Figure A.14.

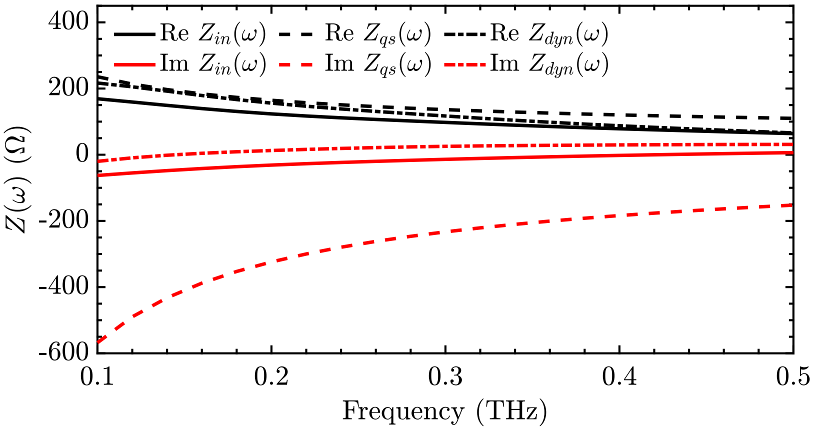

Figure A.14: Input impedance as function of the frequency of an infinite dipole printed between air ($\varepsilon_r = 1$) and silicon ($\varepsilon_r = 11.9$). The parameters considered are a cross section $w = \lambda_d/10$ and a delta gap $\Delta = \lambda_d/10$ where λ_d is the wavelength in the denser medium at the higher frequency.

A.2.4 Infinite Dipole between two Infinite Dielectrics - Fed by a small Gap

Let us consider an infinite dipole printed between two homogeneous half-spaces with permittivities ε_{r2} and ε_{r1}, where $\varepsilon_{r2} > \varepsilon_{r1}$, with cross section w and delta gap Δ as shown in Figure A.11.

The reciprocal of the sum of integrals in (A.45) yields an impedance with a reactive part which is exclusively capacitive. A more realistic modeling of a dipole includes an inductive contribution of the gap (due to the bending of the current which is forced to flow across the gap). Since this thesis is concerned with the modeling of PCAs, this analytical approach of describing the impedance of structures with known Green's functions such as dipoles and slots facilitates the understanding of the radiation mechanism. In order to introduce this inductive contribution, one can essentially add the quasi-static impedance of the difference of two infinite slots with different gap dimensions. The following procedure describes more rigorously what stated above. The modeling of the structure is shown in Figure A.15. The two infinite dipoles have the same width Δ, but different gap dimensions (t and w). Accordingly, the impedances of two infinite slots with similar gap dimensions can be written as

$$Z_{in}^{slot}(w,\Delta) = Z_{qs}^{slot}(w,\Delta) + Z_{dyn}^{slot}(w,\Delta) \tag{A.48}$$

$$Z_{in}^{slot}(w,t) = Z_{qs}^{slot}(w,t) + Z_{dyn}^{slot}(w,t) \tag{A.49}$$

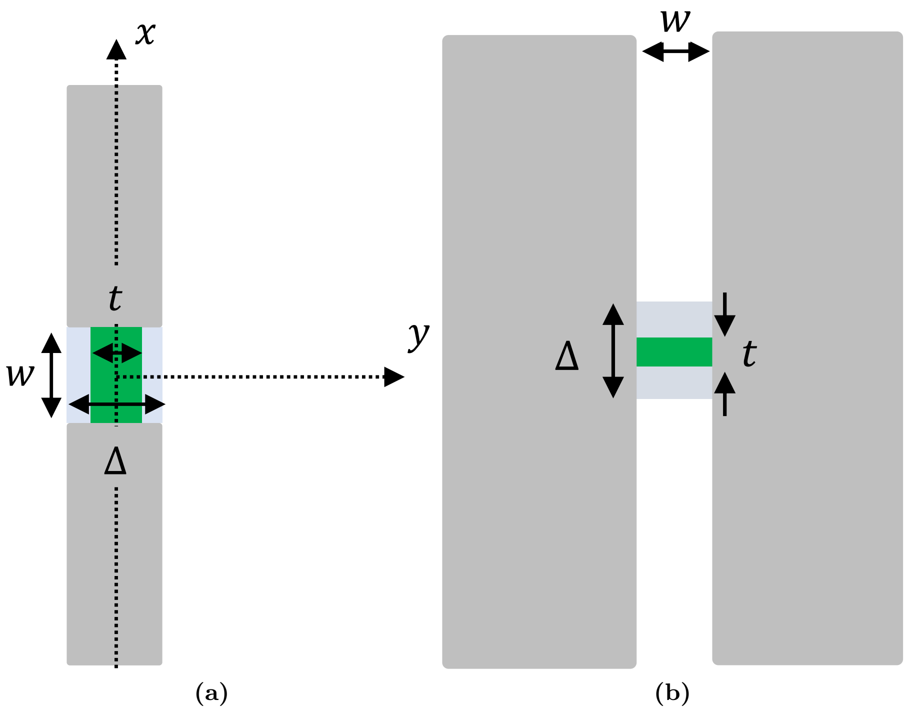

Figure A.15: Infinite dipole printed between two homogeneous half-spaces with permittivities ε_{r2} and ε_{r1}, where $\varepsilon_{r2} > \varepsilon_{r1}$, with cross section w and delta gap Δ. The inductance of the gap is introduced by decreasing the delta gap dimension Δ to a value t (Figure A.15a). The rigorous procedure involves considering two infinite slots with the same width w and different delta gap dimensions Δ and t (Figure A.15b).

Since the dynamic part of the impedance does not depend from the gap dimensions, one can safely assume that

$$Z_{dyn}^{slot}(w,t) \approx Z_{dyn}^{slot}(w,\Delta) \tag{A.50}$$

And therefore substituting (A.50) in (A.49) one obtains that

$$Z_{in}^{slot}(w,t) = Z_{qs}^{slot}(w,t) + Z_{dyn}^{slot}(w,\Delta)$$

The difference of the impedances of the two slots yields:

$$\begin{aligned} Z_{in}^{slot}(w,t) - Z_{in}^{slot}(w,\Delta) &= Z_{qs}^{slot}(w,t) + Z_{dyn}^{slot}(w,\Delta) - Z_{qs}^{slot}(w,\Delta) - Z_{dyn}^{slot}(w,\Delta) \\ &= Z_{qs}^{slot}(w,t) - Z_{qs}^{slot}(w,\Delta) \\ &= Z_{qs}^{slot} \end{aligned}$$

where Z_{qs}^{slot} represents the inductive part of the gap. Alternatively, one could approximate Z_{qs}^{slot} as in [24] where the quasi-static impedance associated with the reduction of the inner conductor is computed as

$$Z_{qs}^{slot} = Z(t) - Z(\delta)$$

where

$$\begin{aligned} Z(\xi) &= k_0 w \left[Z_a(\xi) + Z_b(\xi) \right] \\ Z_a(\xi) &= \frac{j\pi\zeta_0}{2\xi^2(k_1^2 - k_2^2)} \left[\frac{H_0^{(2)}(k_2\xi) - J_0(k_2\xi)}{-j} - \frac{H_0^{(2)}(k_1\xi) - J_0(k_1\xi)}{-j} + \frac{2}{\pi}\ln\left(\frac{k_1}{k_2}\right) \right] \\ Z_b(\xi) &= \frac{\pi\zeta_0}{2} \left\{ \frac{j}{2}\left[-\frac{2}{\pi}\ln(e^{\gamma}\xi) + \frac{3}{\pi} \right] - \frac{j\left[k_1^2 \ln\left(\frac{k_1}{2}\right) - k_2^2 \ln\left(\frac{k_2}{2}\right) \right]}{\pi(k_1^2 - k_2^2)} \right\} \end{aligned}$$

where $\gamma = 0.5772156649\ldots$ is the Euler constant. The dipole impedance with a smaller gap t can now be written as

$$Z_{in}^{dip}(w,\Delta,t) = Z_{qs}^{dip}(w,\Delta,t) + Z_{dyn}^{dip}(w,\Delta,t) + Z_{qs}^{slot}$$

The final dipole admittance can be recovered simply as $Y_{in}^{dip}(w,\Delta,t) = Z_{in}^{dip}(w,\Delta,t)^{-1}$.

An example of the impedance is shown in Figure A.16.

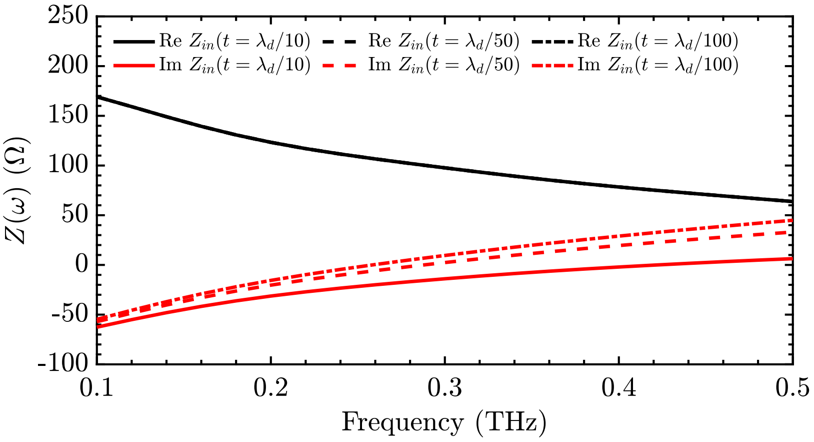

Figure A.16: Input impedance as function of the frequency of an infinite slot printed between air ($\varepsilon_r = 1$) and silicon ($\varepsilon_r = 11.9$) with cross section $w = \lambda_d/10$ and delta gap $\Delta = \lambda_d/10$ where λ_d is the wavelength in the denser medium at the higher frequency. The inductance of the gap is introduced by decreasing the delta gap dimension Δ to a value t.

Appendix B

Useful integrals

B.1 Convolution

The convolution integral in time domain is defined as

$$a(t) * b(t) = \int_{-\infty}^{\infty} a(t-\xi)b(\xi)d\xi$$

B.2 Fourier Transform

The definitions of Fourier-transform and anti Fourier-transform used in this thesis are, respectively:

$$\begin{aligned} A(\omega) = \mathcal{F}\left[a(t)\right] &= \int_{-\infty}^{\infty} a(t)e^{-j\omega t}dt \\ a(t) = \mathcal{F}^{-1}\left[A(\omega)\right] &= \frac{1}{2\pi}\int_{-\infty}^{\infty} A(\omega)e^{j\omega t}d\omega \end{aligned}$$

B.3 Gaussian Integral

The simplest Gaussian integral is

$$I = \int_{-\infty}^{\infty} e^{-x^2}dx$$

which can be solved quite easily. Squaring the quantity I, we get

$$I^2 = \int_{-\infty}^{\infty} e^{-x^2}dx \int_{-\infty}^{\infty} e^{-y^2}dy = \int_{-\infty}^{\infty}\int_{-\infty}^{\infty} e^{-(x^2+y^2)}dxdy$$

Going over to polar coordinates, we have $r^2 = x^2 + y^2$, $dxdy = rdrd\vartheta$, and

$$I^2 = \int_{0}^{\infty}\int_{0}^{2\pi} e^{-r^2}rdrd\vartheta$$

Integration of this double integral is now straightforward, and we have

$$I = \int_{-\infty}^{\infty} e^{-x^2}dx = \sqrt{\pi}$$

For example

$$I = \int_{-\infty}^{\infty} e^{-\frac{a}{n}x^2} dx = \sqrt{\frac{n}{a}}\sqrt{\pi}$$

Appendix C

Impulse Response of an Antenna

The voltage and current relation can be expressed via the product in frequency domain with the input impedance:

$$Z_{in}(\omega)I(\omega) = V(\omega) \tag{C.1}$$

In time domain the voltage $v(t)$ can be expressed as a convolution of a certain transfer function $h_{imp}(t)$ and the current $i(t)$ ($i(t) = 0$ for $t < 0$):

$$v(t) = h_{imp}(t) * i(t) = \int_{-\infty}^{\infty} h_{imp}(t-\xi)i(\xi)d\xi$$

which in frequency domain becomes

$$V(\omega) = \mathcal{F}\left[v(t)\right] = \int_{-\infty}^{\infty} \left[\int_{-\infty}^{\infty} h_{imp}(t-\xi)i(\xi)d\xi\right] e^{-j\omega t}dt \tag{C.2}$$

By rewriting the convolution integral in (C.2), one can notice that

$$\int_{-\infty}^{\infty} h_{imp}(t-\xi)e^{-j\omega t}dt = H_{imp}(\omega)e^{-j\omega\xi} \tag{C.3}$$

Substituting (C.2) in (C.1) one obtains

$$\begin{aligned} Z_{in}(\omega)I(\omega) &= \int_{-\infty}^{\infty} \left[\int_{-\infty}^{\infty} h_{imp}(t-\xi)i(\xi)d\xi\right] e^{-j\omega t}dt \\ &= \int_{-\infty}^{\infty} \left[\int_{-\infty}^{\infty} h_{imp}(t-\xi)e^{-j\omega t}dt\right] i(\xi)d\xi \\ &= \int_{-\infty}^{\infty} \left[H_{imp}(\omega)e^{-j\omega\xi}\right] i(\xi)d\xi \\ &= H_{imp}(\omega)I(\omega) \end{aligned} \tag{C.4}$$

Finally the impulse response is recovered as

$$h_{imp}(t) = \mathcal{F}^{-1}\left[Z_{in}(\omega)\right] \tag{C.5}$$

Bibliography

[1] N. Khiabani, Y. Huang, Y. Shen, and S. Boyes. Theoretical modeling of a photoconductive antenna in a terahertz pulsed system. *IEEE Transactions on Antennas and Propagation*, 61(4):1538–1546, April 2013.

[2] Gabriel C. Loata, Mark D. Thomson, Torsten Löffler, and Hartmut G. Roskos. Radiation field screening in photoconductive antennae studied via pulsed terahertz emission spectroscopy. *Applied Physics Letters*, 91(23):232506, 2007.

[3] J. Y. Suen, W. Li, Z. D. Taylor, and E. R. Brown. Characterization and modeling of a terahertz photoconductive switch. *Applied Physics Letters*, 96(14):141103, 2010.

[4] A. Garufo, G. Carluccio, N. Llombart, and A. Neto. Norton equivalent circuit for pulsed photoconductive antennas - part i: Theoretical model. *IEEE Transactions on Antennas and Propagation*, 66(4):1635–1645, April 2018.

[5] CST MWS 2018. Available: https://www.cst.com/.

[6] A. Garufo, P. M. Sberna, G. Carluccio, J. R. Freeman, D. R. Bacon, L. Li, J. Bueno, J. J. A. Baselmans, E. H. Linfield, A. G. Davies, N. Llombart, and A. Neto. A connected array of coherent photoconductive pulsed sources to generate mw average power in the submillimeter wavelength band. *IEEE Transactions on Terahertz Science and Technology*, 9(3):221–236, May 2019.

[7] D. H. Auston, K. P. Cheung, J. A. Valdmanis, and D. A. Kleinman. Cherenkov radiation from femtosecond optical pulses in electro-optic media. *Phys. Rev. Lett.*, 53:1555–1558, Oct 1984.

[8] D. H. Auston, K. P. Cheung, and P. R. Smith. Picosecond photoconducting hertzian dipoles. *Applied Physics Letters*, 45(3):284–286, 1984.

[9] Jérome Faist, Claire Gmachl, Federico Capasso, Carlo Sirtori, Deborah L. Sivco, James N. Baillargeon, and Alfred Y. Cho. Distributed feedback quantum cascade lasers. *Applied Physics Letters*, 70(20):2670–2672, 2019/07/16 1997.

[10] Rüdeger Köhler, Alessandro Tredicucci, Fabio Beltram, Harvey E. Beere, Edmund H. Linfield, A. Giles Davies, David A. Ritchie, Rita C. Iotti, and Fausto Rossi. Terahertz semiconductor-heterostructure laser. *Nature*, 417(6885):156–159, 2002.

[11] D. Cavallo. *Connected array antennas : analysis and design.* PhD thesis, Department of Electrical Engineering, 2011.

[12] A. Garufo, G. Carluccio, J. R. Freeman, D. R. Bacon, N. Llombart, E. H. Linfield, A. G. Davies, and A. Neto. Norton equivalent circuit for pulsed photoconductive antennas

- part ii: Experimental validation. *IEEE Transactions on Antennas and Propagation*, 66(4):1646–1659, April 2018.

[13] D. Cavallo, W. H. Syed, and A. Neto. Equivalent transmission line models for the analysis of edge effects in finite connected and tightly coupled arrays. *IEEE Transactions on Antennas and Propagation*, 65(4):1788–1796, April 2017.

[14] R. M. van Schelven, D. Cavallo, and A. Neto. Equivalent circuit models of finite slot antennas. *IEEE Transactions on Antennas and Propagation*, 67(7):4367–4376, July 2019.

[15] S. Bruni, A. Neto, S. Maci, and G. Gerini. Analysis of an array of long slots printed between two dielectric half-spaces. *not published*.

[16] S. Maci and A. Neto. Green's function of an infinite slot printed between two homogeneous dielectrics-part ii: uniform asymptotic solution. *IEEE Transactions on Antennas and Propagation*, 52(3):666–676, March 2004.

[17] A. Neto. Uwb, non dispersive radiation from the planarly fed leaky lens antenna. part 1: Theory and design. *IEEE Transactions on Antennas and Propagation*, 58(7):2238–2247, July 2010.

[18] A. Neto and S. Maci. Green's function for an infinite slot printed between two homogeneous dielectrics. i. magnetic currents. *IEEE Transactions on Antennas and Propagation*, 51(7):1572–1581, July 2003.

[19] L. B. Felsen and F. Capolino. Time-domain green's function for an infinite sequentially excited periodic line array of dipoles. *IEEE Transactions on Antennas and Propagation*, 48(6):921–931, June 2000.

[20] Andrea Neto. *Application of Method of Moments to the Analysis of Antenna Arrays for Satellite Communications*. PhD thesis, University of Siena, 1999.

[21] Leopold B. Felsen and Nathan Marcuvitz. *Radiation and Scattering of Waves*. IEEE, 1973.

[22] A. Neto and J. J. Lee. Ultrawide-band properties of long slot arrays. *IEEE Transactions on Antennas and Propagation*, 54(2):534–543, Feb 2006.

[23] Neto and Maci. Input impedance of slots printed between two dielectric media and fed by a small delta-gap. *IEEE Antennas and Wireless Propagation Letters*, 3:113–116, 2004.

[24] P. Focardi, A. Neto, and W. R. McGrath. Coplanar-waveguide-based terahertz hot-electron-bolometer mixers mproved embedding circuit description. *IEEE Transactions on Microwave Theory and Techniques*, 50(10):2374–2383, Oct 2002.

[25] A. Neto and P.H. Siegel. Equivalent network characterization for series fed microstrip lines on thin slabs. *not published*.